

THE AEROELASTIC CHARACTERISTICS
OF THE
SATURN IB SA-203
LAUNCH VEHICLE

April 1966

Prepared by: Lars E. Ericsson
Lars E. Ericsson
Flight Technology

Prepared by: Norman J. French
Norman J. French
Aero-Hydrodynamics

Approved by: M. Tucker
M. Tucker, Manager
Flight Technology

Prepared Under Contract NAS 8-11238
for
Aerodynamic Division
Aero-Astroynamics Laboratory
George C. Marshall Space Flight Center
Huntsville, Alabama

SUMMARY

Launch vehicles with slender cone-cylinder forebodies may experience aeroelastic instability under certain conditions. This flow phenomenon has been documented by wind-tunnel experiments. The flow expands to supersonic speeds when passing the cone-cylinder shoulder. The supersonic region is terminated by a normal shock that causes the boundary layer to separate. At increasing angle of attack the leeward boundary layer is thickened and more easily separated, resulting in a forward movement of the shock. On the windward side opposite effects occur, and a negative forebody load is generated that moderately affects the vehicle dynamics. When the angle of attack exceeds a critical value, the leeward boundary layer can not support the shock at any place; this results in complete leeward separation aft of the cone-cylinder shoulder. The associated jumpwise load change is shown to severely affect vehicle dynamics.

The Saturn IB SA-203 utilizes the generalized payload shroud, and at first glance it is geometrically similar enough to the above mentioned cone-cylinder to warrant concern that a similar problem may exist for the SA-203 vehicle.

However, the biconic shoulder of the generalized payload shroud "preseparates" the flow and the reattaching boundary layer on the conic-frustum is strong enough to negotiate the conic-frustum-cylinder shoulder without complete flow separation. The result is that the terminal shock moves smoothly along the cylinder with increasing angle of attack, and large changes in normal force and undamping effects are avoided. The forward movement of the leeward shock is still present because of a thickened boundary layer, and the aft movement of the windward shock results in a negative cylinder load and attendant moderate undamping effects.

The results of the static aerodynamic data analysis for the SA-203 were used in the quasi-steady computational method to predict the aerodynamic damping in the Mach number range of 0.7 to 2.0. The results of the computation show that the SA-203 vehicle is aeroelastically stable for the first three bending modes. It is therefore speculated that the SA-203 will be aerodynamically damped over the entire ascent trajectory.

CONTENTS

Section		Page
	SUMMARY	iii
	ILLUSTRATIONS	vi
1	INTRODUCTION	1-1
2	SATURN IB SA-203 ANALYSIS	2-1
	2.1 Static Aerodynamic Analysis	2-1
	2.2 Aerodynamic Damping Analysis	2-4
3	CONCLUSIONS	3-1
4	REFERENCES	4-1
Appendix		
A	NOMENCLATURE	A-1
B	DOCUMENTATION OF SA-203 LUMPED LOADS	B-1
C	AEROELASTIC EFFECTS OF BOUNDARY LAYER-TERMINAL SHOCK INTERACTION	C-1
	C.1 Introduction	C-1
	C.2 Statement of Problem	C-1
	C.3 Analytic Approach	C-5
	C.4 Terminal Shock Aerodynamics	C-7
	C.5 Vehicle Dynamics	C-12
	C.5.1 Aerodynamic Damping	C-15
	C.5.2 Nonlinear Damping	C-16
	C.6 Discussion	C-27
	C.7 Conclusions	C-30

ILLUSTRATIONS

Figure		Page
2-1	SA-203 Configuration	2-2
2-2	Comparison of SA-203 Integrated Lumped Loads With Force Data Results	2-5
2-3	SA-203 Aerodynamic Damping Characteristics	2-8
B-1	SA-203 Definition of Lumped Normal Force Vectors	B-2
B-2	SA-203 Local Normal Force Derivatives at $\alpha = 0$	B-3
B-3	SA-203 Induced Normal Force Derivatives at $\alpha = 0$	B-5
B-4	SA-203 Separated-Flow Velocity Ratio at $\alpha = 0, 4^\circ, \text{ and } 8^\circ$	B-6
B-5	SA-203 Local and Induced Nose-Shroud and Interstage-Flare Axial-Force Moment Derivatives at $\alpha = 0$	B-7
B-6	SA-203 Lumped-Load Centers of Pressure at $\alpha = 0$	B-9
B-7	SA-203 Local Normal Force Derivatives at $\alpha = 4^\circ$	B-11
B-8	SA-203 Induced Normal Force Derivatives at $\alpha = 4^\circ$	B-13
B-9	SA-203 Local and Induced Nose-Shroud and Interstage-Flare Axial-Force Moment Derivatives at $\alpha = 4^\circ$	B-14
B-10	SA-203 Lumped-Load Centers of Pressure at $\alpha = 4^\circ$	B-15
B-11	SA-203 Local Normal Force Derivatives at $\alpha = 8^\circ$	B-17
B-12	SA-203 Induced Normal Force Derivatives at $\alpha = 8^\circ$	B-21
B-13	SA-203 Local and Induced Nose-Shroud and Interstage-Flare Axial-Force Moment Derivatives at $\alpha = 8^\circ$	B-22
B-14	SA-203 Lumped-Load Centers of Pressure at $\alpha = 8^\circ$	B-23
B-15	SA-203 Normalized Free-Free Bending Mode Shapes	B-25
C-1	Aerodynamic Characteristics at $M_\infty = 0.89$ of a 20° Cone-Cylinder Body With Separated Flow	C-31
C-2	Effect of Cone Angle on Occurrence of Complete Flow Separation at $M_\infty = 0.89$	C-33

Figure		Page
C-3	Effect of Angle of Attack on Terminal-Shock Location on a 20° Cone-Cylinder Body at $M_\infty = 0.95$	C-34
C-4	Effect of Mach Number on Terminal-Shock Location on a 20° Cone-Cylinder Body at $\alpha = 0$	C-36
C-5	Combined Effect of Mach Number and Cone Angle on the Terminal-Shock Location on Cone-Cylinder Bodies at $\alpha = 0$	C-38
C-6	Combined Effect of Mach Number and Angle of Attack on the Terminal-Shock Location on a 20° Cone-Cylinder Body	C-39
C-7	Terminal Shock Location in Inviscid and Viscous Flow on Cone-Cylinder Bodies	C-40
C-8	Effect of Boundary Layer Thickness and Pressure Gradient on the Terminal-Shock Movement on a 20° Cone-Cylinder Body at $\alpha = 0$ and High Subsonic Mach Numbers	C-41
C-9	Normal Force Derivatives Induced by the Terminal-Shock Movement on a 20° Cone-Cylinder Body at $\alpha = 0$ and High Subsonic Mach Numbers	C-42
C-10	Effect of Cone Angle and Angle of Attack on the Terminal-Shock Movements at $M_\infty \approx 0.88$	C-43
C-11	Axial Variation of the Boundary Layer Auxiliary Shape Factor on a 30° Cone-Cylinder Body at $\alpha = 0$ and Various Mach Numbers	C-44
C-12	$\alpha - M_\infty$ - Regions for Fluctuating Flow on Cone-Cylinder Bodies With Various Cone Half-Angles	C-45
C-13	Coordinate Systems	C-46
C-14	Effect of Separation-Induced Terminal-Shock Movement on the Damping of an Elastic Vehicle Oscillating in its Second Bending Mode	C-47
C-15	Schematic Characteristics	C-48
C-16	Effect of Complete Windward-Side Flow Separation in the Damping of an Elastic Vehicle Oscillating in its Second Bending Mode at Various Nose Amplitudes	C-49
C-17	Comparison of Leeward- and Windward-Side Damping Combinations Induced by Complete Flow Separation on an Elastic Vehicle Oscillating in its Second Bending Mode at 0.25 Deg Nose Amplitude	C-50
C-18	Effect of Mode Shape on the Separation-Induced Elastic Vehicle Damping	C-51

Figure		Page
C-19	Aerodynamic Damping Measured on an 8-Percent Elastic Model of the Saturn I, Block II Vehicle With a Jupiter Nose	C-52
C-20	Dynamic Effects of Separation Induced Pitching-Movement Discontinuity on a Blunt-Nose, Cylinder-Flare Body at Transonic Speed	C-53
C-21	Effect of Complete Leeward-Side Separation on Pressure and Load Distribution Over a Hemispherical-Nose, Cylinder-Flare Body at $M_\infty = 0.95$	C-54
C-22	Dynamic Effects of Separation-Induced Pitching-Movement Discontinuity on a Hemispherical-Nose, Cylinder-Flare Body at $M_\infty = 0.95$	C-55
C-23	Shadowgraphs of the Flow Over the Saturn IB SA-203 Vehicle With a Generalized Payload at $M_\infty = 0.9$ and Various Angles of Attack	C-56
C-24	Shadowgraphs at $M_\infty = 0.65$ of the Flow Over Two Blunt-Nose, Cylinder-Flare Bodies With Identical Impact Nose Drag	C-57
C-25	Pressure Distribution Over the Forebody of the SA-203 Vehicle at $M_\infty = 0.9$ and Various Angles of Attack	C-58
C-26	Shadowgraphs of the Flow Over the SA-203 Vehicle at $\alpha = 0$	C-60
C-27	Pressure Distribution Over the Forebody of the SA-203 Vehicle at $\alpha = 0$ and Various Mach Numbers	C-61
C-28	Terminal-Shock Position on the SA-203 Vehicle as a Function of Mach Number and Angle of Attack	C-62

Section 1
INTRODUCTION

The present study has been conducted to provide the aerodynamic damping characteristics of the Saturn IB SA-203 vehicle and to document the flow field over the forward portion of the vehicle. The SA-203 vehicle is scheduled to launch a liquid hydrogen experiment and employs a generalized payload shroud in place of the Apollo command module, escape rocket and tower. The SA-203 is approximately 16 m shorter than the Apollo-Saturn IB configuration, and has a more nearly constant diameter. These geometric features produce an entirely new flow field for consideration. The extensive separated-flow field associated with the escape rocket and tower is gone, and a flow field controlled by the biconic configuration of the generalized payload shroud is found in its place.

The following sections describe the static load distributions used in the quasi-steady analysis and discuss the flow field and pressure distribution over the forward portion of the SA-203 vehicle and the resulting aerodynamic damping.

Section 2
SATURN IB SA-203 ANALYSIS

The aerodynamic damping for the Saturn IB SA-203 vehicle was computed for the high-dynamic pressure portion of the trajectory using the quasi-steady analytical method (Refs. 1 and 2). The static-load distributions over the SA-203 were obtained through analysis of all available data (Refs. 3 through 12). The distributions were reduced to lumped loads that were further split into local and induced derivatives. Appendix B documents the derivatives for 0-, 4-, and 8-deg angle of attack. Structural data for the first three bending modes and the vehicle trajectory were obtained from Refs. 13 and 14, respectively. Identification (Refs. 15 through 17) and understanding (Refs. 18 and 19) of a flow field suspected to exist on the forward portion of the Saturn SA-203 is documented in Appendix C.

2.1 STATIC AERODYNAMIC ANALYSIS

The Saturn IB SA-203 vehicle with the generalized payload shroud (Fig. 2-1) is unlike the Apollo-Saturn IB. The prominent separated-flow effects of the Apollo escape-rocket and tower are not present. There was evidence (Refs. 15 through 18) that the generalized payload shroud with its blunt biconic configuration could have considerable dynamic destabilizing effects. Chevalier and Robertson (Refs. 15 through 17) measured large changes in the loading on a cone-cylinder model caused by the sudden jump forward of the terminal shock to the cone-cylinder shoulder. Because of this information, there was concern that a similar interaction between the terminal shock and the separated boundary layer aft of the shoulder would cause drastic undamping effects to occur on the SA-203.

Static pressure coefficient data (Ref. 9) used in the analysis of the SA-203 were supplemented, at the request of LMSC, by additional pressure-distribution wind tunnel

tests (unpublished MSFC wind tunnel Test 2328). These additional tests were designed to document the sudden-jump phenomenon of the terminal shock. However, the tests documented the complete absence of the sudden separation phenomenon. Briefly, what happens is that the biconic shoulder of the generalized payload "preseparates" the flow and the reattaching boundary layer on the conical frustum is strong enough to negotiate the conic-frustum-cylinder shoulder without complete flow separation, even when the terminal shock is in close proximity to the shoulder. As a result the terminal shock moves smoothly along the cylindrical section with increasing angle of attack, and large changes in normal force are avoided as well as the feared undamping effects. Appendix C documents the complete analysis of the terminal shock-boundary layer interaction on the SA-203 vehicle.

Analysis of the data from Test 2328 involved an unexpected complication. For this test top centerline pressures were measured; both windward and leeward data were obtained by pitching the model through an angle range of ± 10 deg. Presumably the experimental setup was completely symmetrical in the wind-tunnel test section. However, the Mach number varied as much as 0.03 with negative angles of attack during a run. That is, when pitching the model through positive angles of attack, the Mach number held acceptably constant, but for negative angles of attack the Mach number was noted to fall off, e.g., Run 16 at $\alpha \approx 0^\circ$, $M = 0.948$ and at $\alpha \approx -10^\circ$, $M = 0.918$. Because the SA-203 configuration is extremely sensitive to Mach number in the range $0.80 \leq M \leq 0.95$, considerable data manipulation (extrapolating, cross plotting, and carpet plotting) was required before meaningful results were obtained.

The integrated pressure data (Ref. 9) were compared with total force data (Refs. 10 through 12) for the SA-203. Segmented-model force data were not available for the analysis; however, the pressure model had rather dense pressure orifice locations. The closely spaced orifices resulted in well-defined local normal force coefficient distributions, so that the negative load peak after the conic-frustum on the cylinder could be defined.

Integration of the load distributions defined the 16 lumped-load derivatives for 0-, 4-, and 8-deg angle of attack over the Mach number range of $0.7 \leq M \leq 2.0$. Agreement between the summed, lumped loads and the overall force data is shown in Fig. 2-2.

The force data from Ref. 10 and 12 do not agree at high angles of attack ($\alpha \geq 8^\circ$), the results of Ref. 10 being lower than those of Ref. 12. Because of this discrepancy, both results have been considered for $\alpha = 8^\circ$ and are shown in Fig. 2-2.

Also shown in Fig. 2-2 is the attached flow estimate at $M = 0.9$. The attached flow estimate was obtained by use of the transonic similarity parameter applied to the $M = 0.7$ static-load distributions of Ref. 9. The attached flow lumped-load derivatives were then perturbed to account for separated-flow effects.

2.2 AERODYNAMIC DAMPING ANALYSIS

The biconic shoulder caused the flow to expand to supersonic speed and shock out at $M \approx 1.4$ for $\alpha \geq 0^\circ$. (The shock causes the preseparation discussed earlier.) This shock effectively filtered out the accelerated-flow effects (described in Appendix C) as the flow conditions on the conical frustum become rather insensitive to angle of attack (and angular rates). Thus, boundary layer build-up was the dominant viscous effect, and the quasi-steady methods (Refs. 1 and 2) used on previous Saturn configurations (Refs. 1 and 20 through 23) were applicable in unmodified form.

The damping characteristics of SA-203 are presented in Fig. 2-3 in percent of critical for 0-, 4-, and 8-deg angle of attack over the high-dynamic pressure portion of the ascent trajectory ($0.7 \leq M \leq 2.0$). The bending-mode shapes were chosen from Ref. 13 at time 60 sec and are shown in Fig. B-15. The trajectory was taken from Ref. 14. The results of the quasi-steady computation show that the SA-203 vehicle has positive aerodynamic damping for the first three bending modes in the Mach number range of 0.7 to 2.0. Therefore, it is speculated that the vehicle will exhibit positive damping over the entire ascent trajectory.

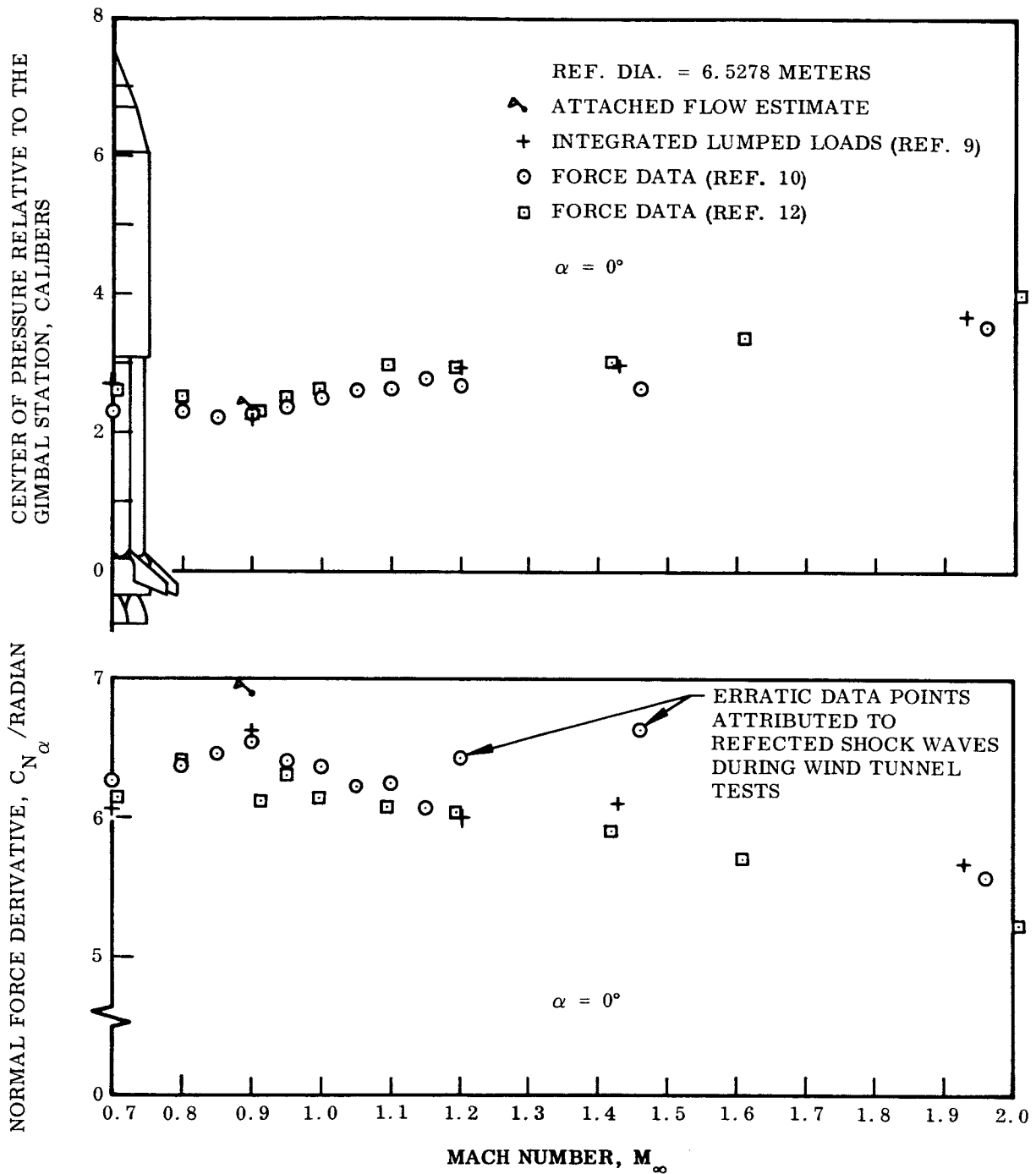


Fig. 2-2 Comparison of SA-203 Integrated Lumped Loads With Force Data Results

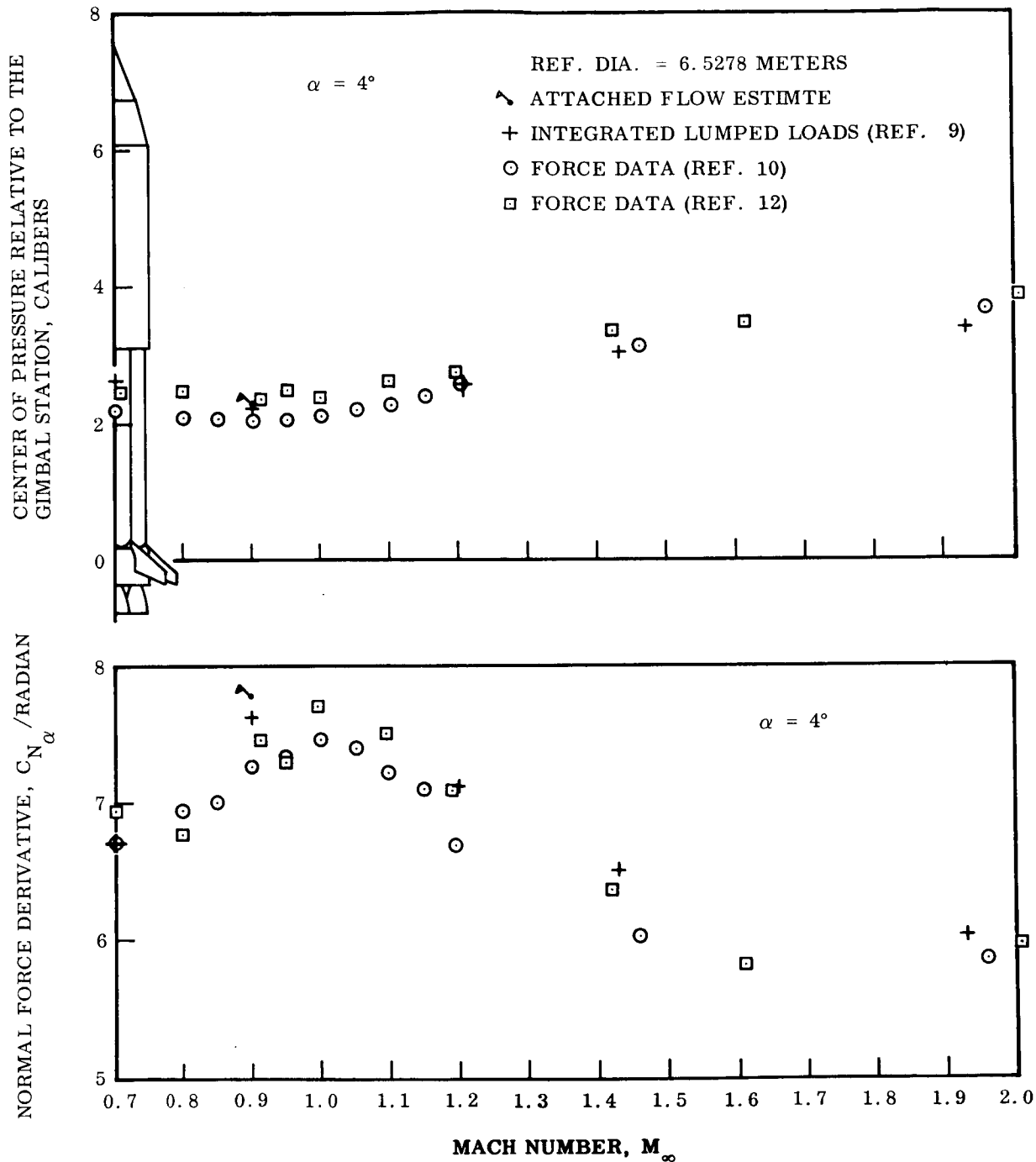


Fig. 2-2 Comparison of SA-203 Integrated Lumped Loads With Force Data Results (Cont.)

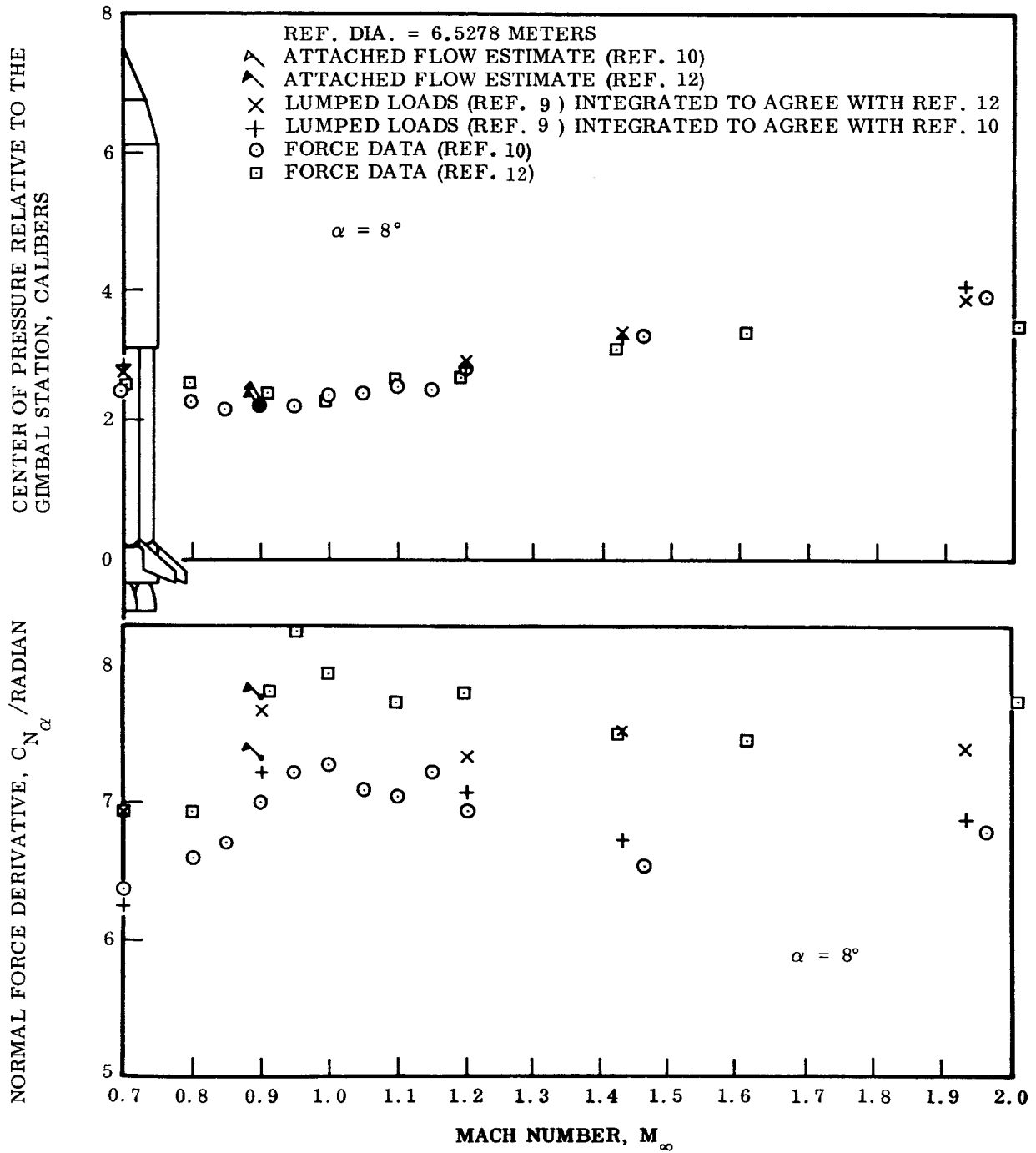


Fig. 2-2 Comparison of SA-203 Integrated Lumped Loads With Force Data Results (Cont.)

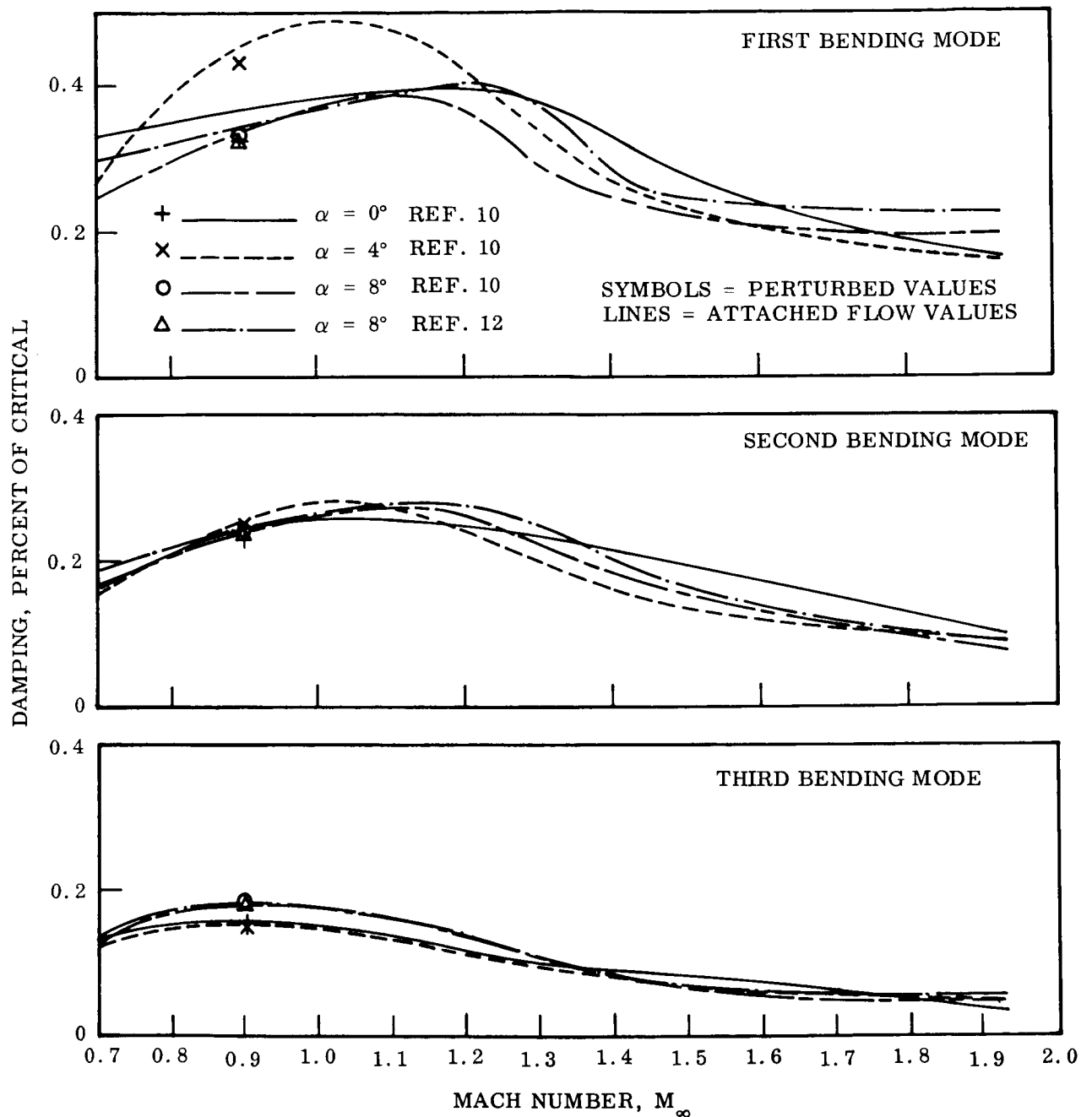


Fig. 2-3 SA-203 Aerodynamic Damping Characteristics

In Fig. 2-3 the attached-flow values are shown as well as the perturbed values at $M = 0.9$. Separated flow reduces the positive loading over the forward portion of the vehicle, and for the first three bending modes, the perturbed damping values are, therefore, lower than the attached-flow values. The first-mode damping curves are less positive in the transonic speed range for $\alpha = 0^\circ$ and 8° than for $\alpha = 4^\circ$. This is because the nonlinear induced loads become smaller with increasing angle of attack and the local loads peak near $\alpha = 4^\circ$ with the result that the total normal force derivative is greatest at $\alpha = 4^\circ$. The same trend is seen to a lesser extent in the second-mode damping curves. In the supersonic speed regime the damping curves are nearly independent of angle of attack for all three bending modes.

Section 3
CONCLUSIONS

The Saturn IB SA-203 vehicle is not affected by the dramatic dynamically destabilizing effects expected to be generated by the generalized payload shroud in the transonic speed regime. The design feature that saved the vehicle is the biconic shroud. This shroud configuration produces a strengthened boundary layer which can hold off flow separation sufficiently so that jumpwise terminal shock motions with attendant large undamping effects are avoided.

Careful study and analysis of the data for the SA-203 using quasi-steady analytical methods indicate that the first three bending modes of the vehicle are aerodynamically damped over the critical Mach number range from 0.7 to 2.0. Therefore, it may be speculated that the SA-203 will be aerodynamically damped over the entire ascent trajectory.

Section 4
REFERENCES

1. Lockheed Missiles & Space Company, Report on Saturn I - Apollo Unsteady Aerodynamics, by Lars-Eric Ericsson and J. Peter Reding, LMSC A650215, Sunnyvale, California, February 1964 (U)
2. Lars-Eric Ericsson and J. Peter Reding, "Analysis of Flow Separation Effects on the Dynamics of a Large Space Booster", AIAA 64-485, First AIAA Annual Meeting, Washington, D. C. , 29 June-2 July 1964. Also published in Journal of Spacecraft and Rockets, Vol. 2, July-August, 1965 pp. 481-490 (U)
3. National Aeronautics and Space Administration, Ames Research Center, Turbulent Boundary-Layer Separation Induced by Flares on Cylinders at Zero Angle of Attack, by Donald M. Keuhn, NASA TR R-117, Moffett Field, California, 1961 (U)
4. -----, Equations, Tables, and Charts for Compressible Flow, by A. R. Staff, NACA, Rpt 1135, Moffett Field, California, 1953 (U)
5. The Boeing Company, Saturn V Upper Stages Pressure Distribution W/APS Units Longitudinal Pressure Distribution and Local Normal Forces for Future Studies in S-II and S-IVB Region of Separation (0.505% Scale), by J. Wright, Project AD-5-63, 6 April 1964 (U)
6. Chrysler Corporation, Space Division, Static Pressure and Normal Force Coefficient Distributions on the Saturn IB Launch and Aborted Launch Configurations as Determined by Wind Tunnel Tests, by F. Chianese, Jr., TN-AE-63-12, New Orleans, La., 30 Dec 1963 (U)
7. -----, Results of a Wind Tunnel Investigation to Determine the Pressure and Local Normal Force Distribution Over the Saturn IB Vehicle, by H. B. Reese, TN-AE-63-3, New Orleans, Louisiana, 1 August 1963 (U)

8. Cornell Aeronautical Laboratory, Transonic Wind Tunnel Tests of a 0.0175 Scale Pressure Model of the Saturn C-1, Block II Launch Vehicle, by D. L. Millikan, Cornell Report No. HM-1510-Y-8, Buffalo, New York, 1 July 1963 (U)
9. Chrysler Corporation, Space Division, Results of An Experimental Investigation to Determine the Aerodynamic Loadings on Three Saturn Payload Shapes, by H. B. Reese, TN-AE-64-16, New Orleans, Louisiana, 1 March 1964 (U)
10. National Aeronautics and Space Administration, Marshall Space Flight Center, Experimental Static Longitudinal Stability and Axial Force Characteristics of a Saturn IB Liquid Hydrogen (LH₂) Experimental Vehicle Configuration, by R. E. Pitcock, Memo: R-AERO-AD-65-27, Huntsville, Alabama, 2 April 1965 (U)
11. Chrysler Corporation, Space Division, Static Stability and Axial Force Characteristics of a 1.32 Percent Scale Model of the Saturn IB/SA-203 Launch Vehicle, by F. Chianese, TN-AE-65-121, New Orleans, Louisiana, 27 October 1965 (U)
12. LTV Vought Aeronautics Division, Static Force Test in the LTV High Speed Wind Tunnel on a 1.32% Scale Saturn IB/SA-203 Launch Vehicle in the Mach Range 0.5 to 4.8 (U), by M. L. Felber, HSWT Test 196, Dallas, Texas, July 1965 (U)
13. National Aeronautics and Space Administration, Marshall Space Flight Center, Bending Vibration, First Stage Saturn IB, LH₂ Experiment Vehicle Configuration 2, by G. F. McDonough, R-AERO-DD-80, Huntsville, Alabama, 16 November 1964 (U)
14. Chrysler Corporation, Space Division, Preliminary Design Trajectories for the Saturn IB Vehicle SA-203, by C. J. Bertz and A. W. Luetje, TB-AE-65-234, New Orleans, Louisiana, 7 July 1965 (U)
15. Jack E. Robertson, "Unsteady Pressure Phenomena for Basic Missile Shapes at Transonic Speeds", AIAA Preprint No. 64-3, AIAA 1st Aerospace Sciences Meeting, New York, 20-22 January 1964 (U)
16. Arnold Engineering Development Center, Characteristics of Steady-State Pressures on the Cylindrical Portion of Cone-Cylinder Bodies at Transonic Speeds, by J. E. Robertson and H. L. Chevalier, AEDC TDR 63-104, August 1963 (U)

17. Arnold Engineering Development Center, Pressure Flunctuations Resulting from Alternating Flow Separation and Attachment at Transonic Speeds, by H. L. Chevalier and J. E. Robertson, AEDC TDR 63-204, November 1963 (U)
18. Lockheed Missiles & Space Company, Steady and Unsteady Terminal Shock Aerodynamics on Cone-Cylinder Bodies, by Lars Eric Ericsson (to be published).
19. Lars Eric Ericsson, "Aeroelastic Instability Caused by Slender Payloads," AIAA Preprint No. 66-471, AIAA 4th Aerospace Sciences Meeting, Los Angeles, California, 27-29 June 1966 (U)
20. Lockheed Missiles & Space Company, The Aeroelastic Characteristics of the Saturn IB and Saturn V Launch Vehicles, by J. Peter Reding, Dennis M. Jecmen, Norman J. French, and Lars-Eric Ericsson, M-37-65-1, Sunnyvale, California, March 1965 (U)
21. -----, The Aeroelastic Characteristics of the Saturn IB SA-201 Launch Vehicle, by Dennis M. Jecmen, M-37-65-2, Sunnyvale, California, August 1965 (U)
22. -----, The Aeroelastic Characteristics of the Saturn IB SA-202 Launch Vehicle, Addendum to M-37-65-2, Sunnyvale, California (U)
23. -----, The Aeroelastic Characteristics of the Saturn V SA-501 Launch Vehicle, by Dennis M. Jecmen, M-37-66-1, May 1966 (U)
24. J. Peter Reding, Dennis Jecmen, and Lars E. Ericsson, "An Application of Automatic Carpet Plotting to Wind Tunnel Data Reduction", submitted for presentation at the AIAA Aerodynamic Testing Conference, Los Angeles, California, 26-28 September 1966 (U)
25. California Institute of Technology, Jet Propulsion Laboratory, The Fluctuating Pressure Field in a Supersonic Turbulent Boundary Layer, by A. L. Kistler and W. S. Chen, JPL TR 32-277, August 1962 (U)
26. Lockheed Missiles & Space Company, Separated Flow Effects on the Dynamic Stability of Blunt-Nosed Cylinder-Flare Bodies, by Lars Eric Ericsson, LMSC-667991, December 1965 (C)

27. National Aeronautics and Space Administration, Aerodynamic Damping and Buffet Response of an Aeroelastic Model of the Saturn I Block II Launch Vehicle, by Perry W. Hanson and Robert V. Dogget, Jr., NASA TND-2713, March 1965 (U)

Appendix A
NOMENCLATURE

VARIABLES AND CONSTANTS

a	speed of sound, m/sec
a, b	parameter defined in Appendix C, Eqs. (C.51) and (C.52)
B	parameter defined in Appendix C, Eq. (C.36)
c	reference length or cylinder caliber (6.5278 for SA-203), m
D	aerodynamic damping derivative
\bar{D}	effective aerodynamic damping derivative [see Eqs. (C.41) and (C.43)]
E	dissipated energy per cycle of oscillation, kgm
F(t)	generalized force, kg
f(t)	driving function, m/sec ²
K	aerodynamic stiffness derivative
\bar{K}	effective aerodynamic stiffness derivative [see Eq. (C.44)]
L ₁	boundary layer shape factor
M	Mach number (U/a)
M	pitching moment, kgm [coefficient $C_m = M/(\rho U^2/2) S c$]
M _A	axial force moment, kgm [coefficient $C_{m_A} = M_A/(\rho U^2/2) S c$].
\tilde{m}	generalized mass, kg-sec ² /m
N	normal force, kg [coefficient $N/(\rho U^2/2) S$]
p	static pressure, kg/m ² [coefficient $C_p = (p - p_\infty)/(\rho U^2/2)$]

$q(t)$	normalized coordinate, m
S	reference area, m^2 ($\pi c^2/4$)
t	time, sec
T	period, sec
U	velocity, m/sec
\bar{U}	convection velocity, m/sec [see Eq. (C.17)]
w	crossflow, m/sec
x	horizontal coordinate, m
x_1	axial coordinate, m
z	vertical coordinate, m
α	angle of attack, radian or deg
α_0	trim angle of attack, radian or deg
$\tilde{\alpha}$	local crossflow angle, radian or deg
β	arc tan b (phase lag), radian
γ	specific heat ratio ($\gamma = 1.4$ for air)
δ	boundary layer thickness, m
Δ	incremental difference unit
ξ	structural damping, fraction of critical
ξ_s, ξ_a	aerodynamic damping, fraction of critical
θ	body attitude, radian or deg
θ_c	cone half-angle, radian or deg
ν	Prandtl-Meyer expansion angle, radian
ξ	dimensionless coordinate x_1/c
ρ	density of air, $kg \text{ sec}^2/m^4$

φ	normalized modal deflection
φ'	normal mode slope, 1/m ($\partial\varphi/\partial x$)
ψ	phase angle, radian (ωt)
ω	free-free bending frequency or rigid-body pitching frequency, radian/sec

SUBSCRIPTS

a	attached flow
A	due to axial forces
AC	aerodynamic center
b	buffeting
CG	center of gravity
d	discontinuity
e	local external flow
i	induced, e.g., $\tilde{\alpha}_i$ = induced angle of attack controlling the separation
L	at large α
N	nose
n	body force number
o	at $\xi = 0$
o	at α close to zero
p	p_ξ -effect
s	separated flow or shock wave
1,2	body force components (used in Appendix C)
∞	undisturbed flow

δ δ -effect

1,2,etc. number of lumped-load derivatives (see Fig. B-1)

SUPERSCRIPTS

i induced, e.g., $\Delta^i C_N$ = separation induced normal force coefficient

DIFFERENTIAL SYMBOLS

$$\varphi'(x) = \frac{\partial \varphi}{\partial x}$$

$$p_\xi = \frac{\partial p}{\partial \xi}$$

$$\dot{\theta}(t) = \frac{\partial \theta}{\partial t}$$

$$\ddot{q}(t) = \frac{\partial^2 q}{\partial t^2}$$

$$C_{N_\alpha} = \frac{dC_N}{d\alpha}$$

$$\left(\frac{\partial C_N}{\partial \alpha} \right)_\delta = \frac{\partial C_N}{\partial \alpha} \text{ at } \delta = \text{constant}$$

$$\left(\frac{\partial \Delta^i \xi_s}{\partial \alpha} \right)_{p_\xi} = \frac{\partial \Delta^i \xi_s}{\partial \alpha} \text{ at } p_\xi = \text{constant}$$

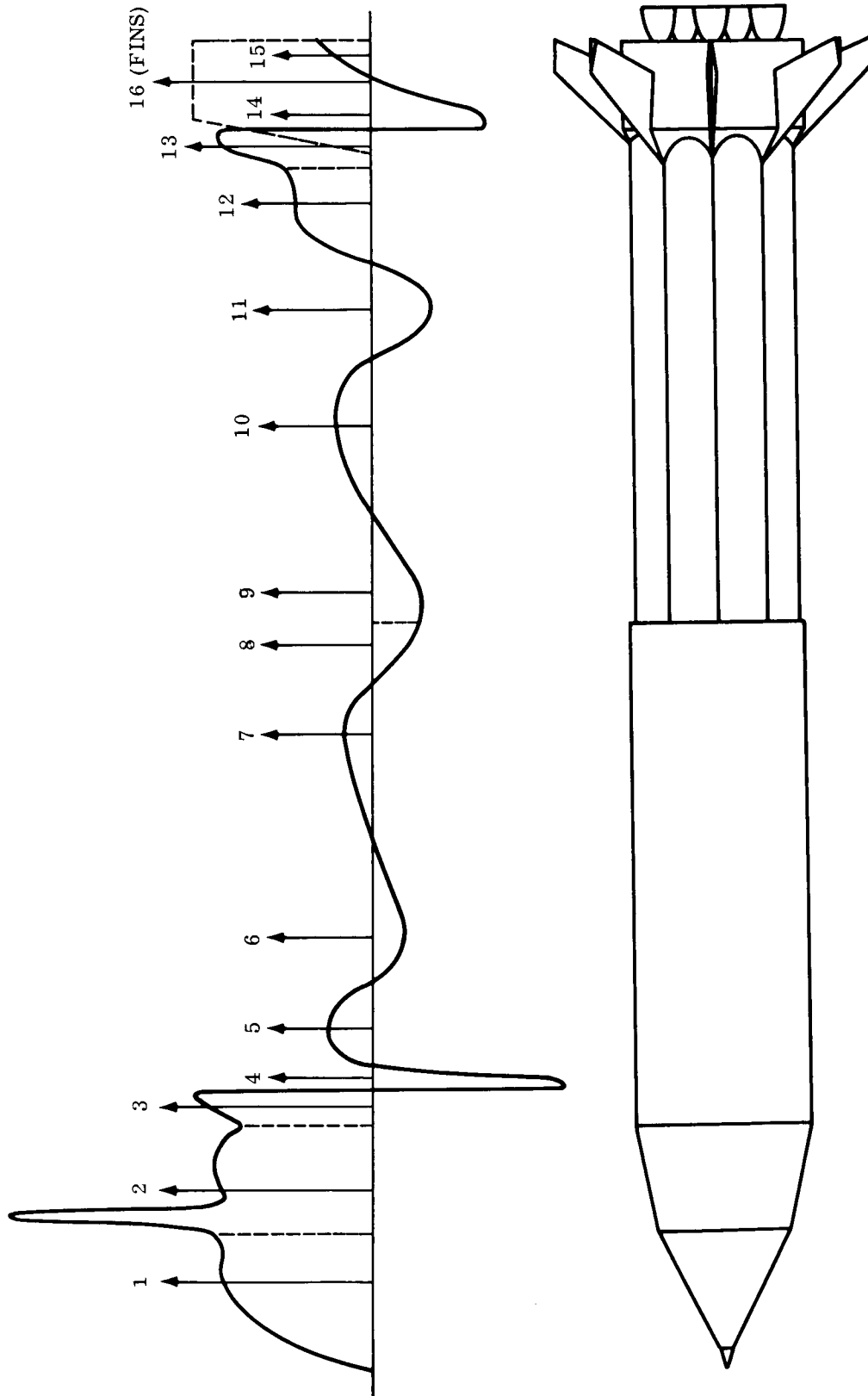
$$C_{N_q} = \frac{\partial C_N}{\partial \frac{q}{U}}$$

$$C_{m_{\dot{\theta}}} = \frac{\partial C_m}{\partial \left(\frac{c\dot{\theta}}{U} \right)}$$

Appendix B
DOCUMENTATION OF SA-203 LUMPED LOADS

The static-load distributions over the SA-203 vehicle have been defined for several Mach numbers and angles of attack. The loadings at nonzero angles of attack were examined closely because of the expected unsteady flow discussed previously and in Appendix C. The summation of these results is shown in Fig. 2-2. This appendix presents, as a function of Mach number, the individual lumped-load and axial-force-moment derivatives for 0-, 4-, and 8-deg angle of attack. Also included are the separated flow velocity ratios and the first three bending mode shapes used in the analysis.

Figure B-1 relates the lumped loads to the general SA-203 force distribution. The $\alpha = 0^\circ$ local and induced components of the lumped-load derivatives are plotted in Fig. B-2 and B-3. Figure B-4 presents the velocity ratio for each of the separated-flow regions, and Fig. B-5 shows the local and induced axial-force moment derivatives on the nose shroud and the interstage flare. The lumped-load centers of pressure are given in Fig. B-6. Both the attached flow and induced-load centers of pressure are shown near Mach = 0.9. The various parameters discussed above are presented in Fig. B-7 through B-10 for $\alpha = 4^\circ$ and in Fig. B-11 through B-14 for $\alpha = 8^\circ$. Figure B-15 shows the first three bending mode shapes of the SA-203 vehicle.



B-2

Fig. B-1 SA-203 Definition of Lumped Normal Force Vectors

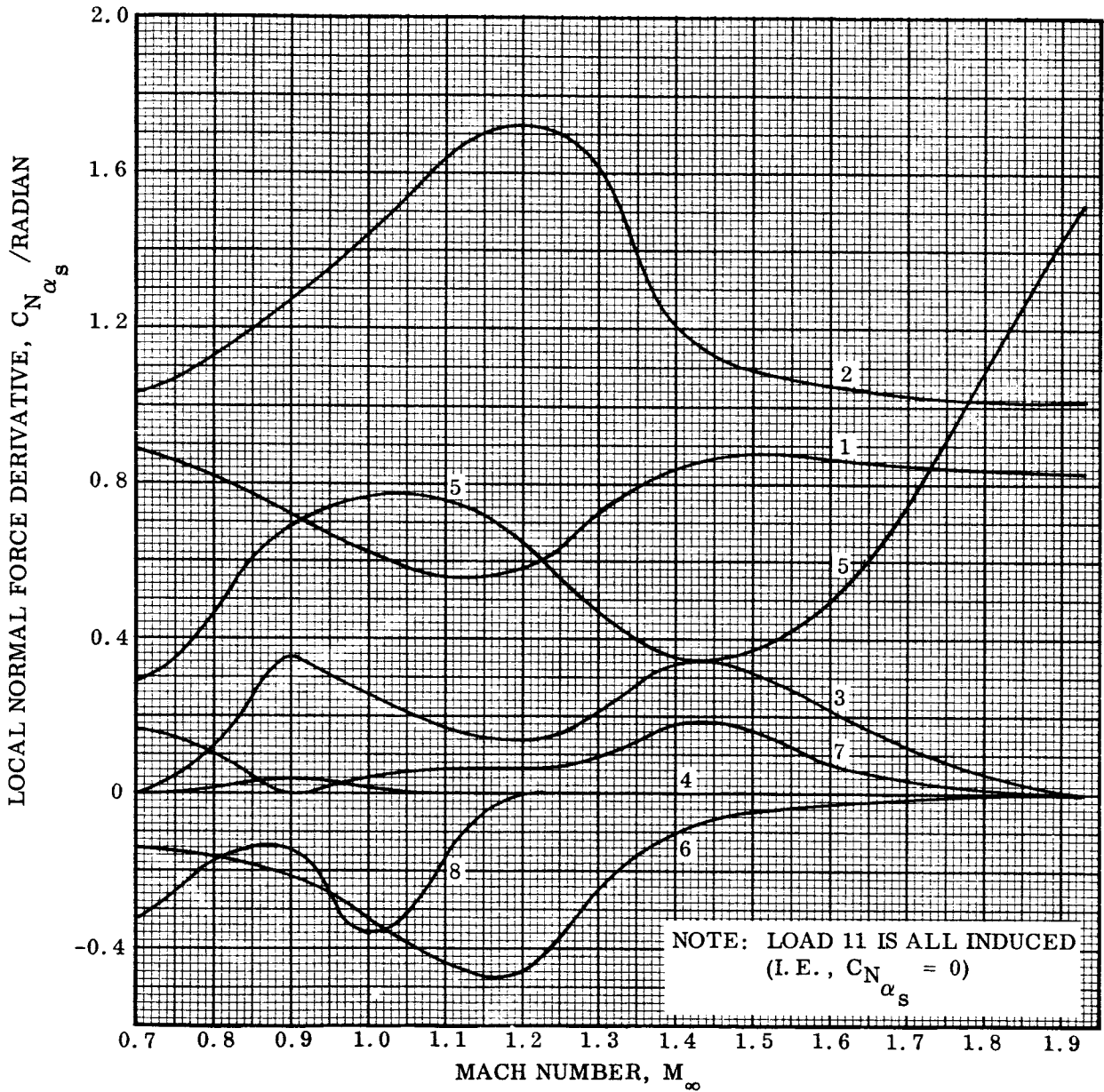
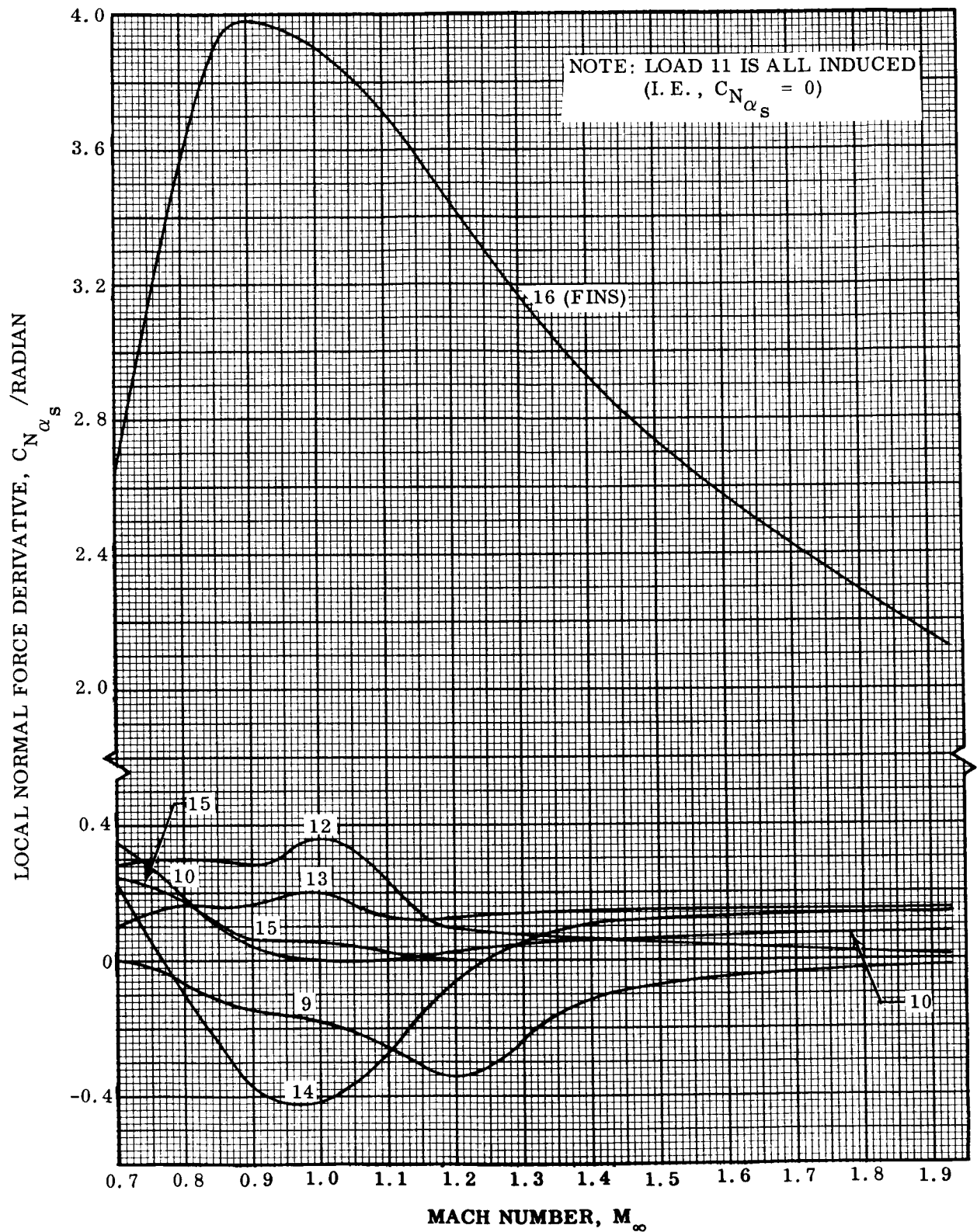


Fig. B-2 SA-203 Local Normal Force Derivatives at $\alpha = 0$

Fig. B-2 SA-203 Local Normal Force Derivatives at $\alpha = 0$ (Cont.)

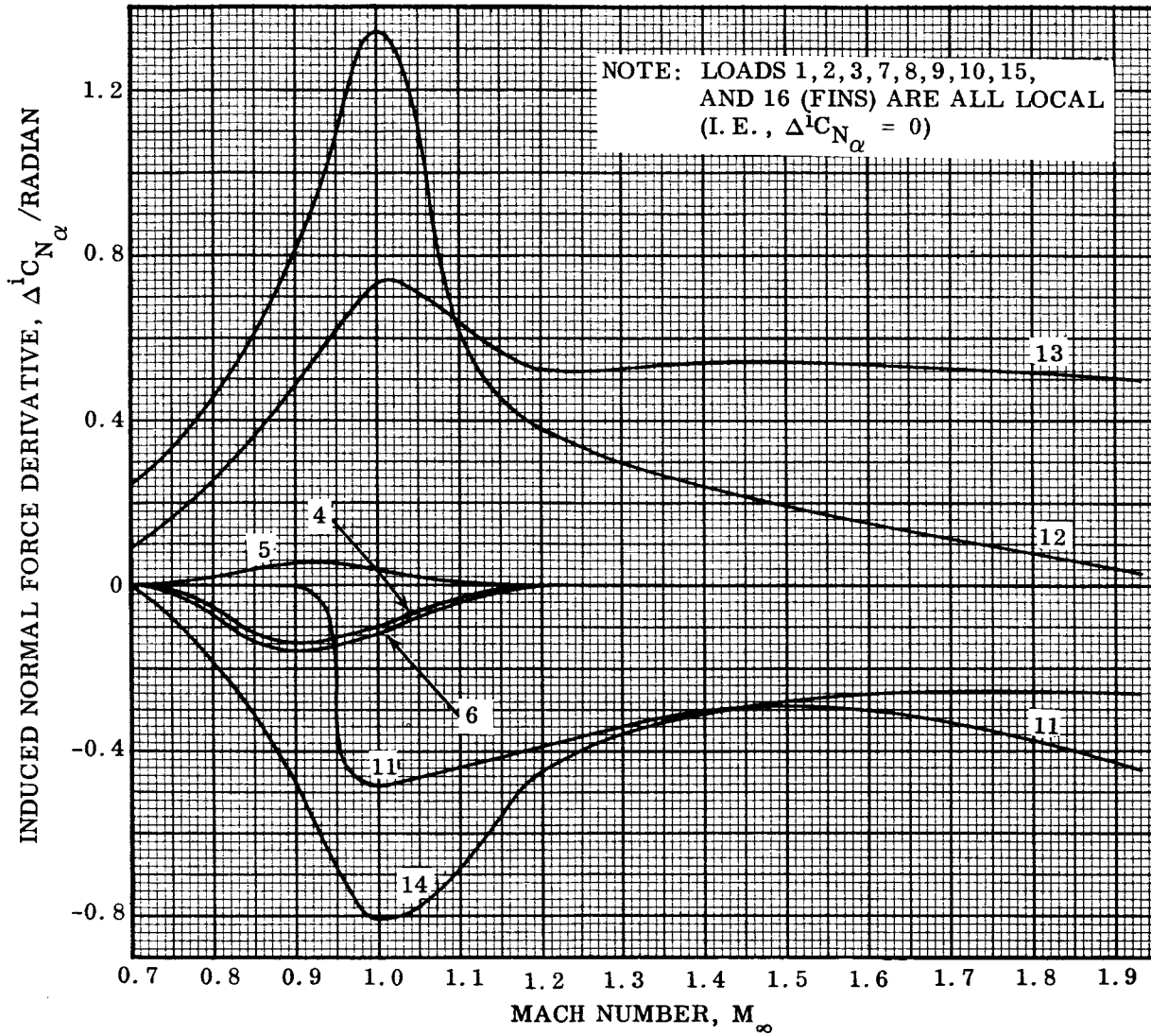


Fig. B-3 SA-203 Induced Normal Force Derivatives at $\alpha = 0$

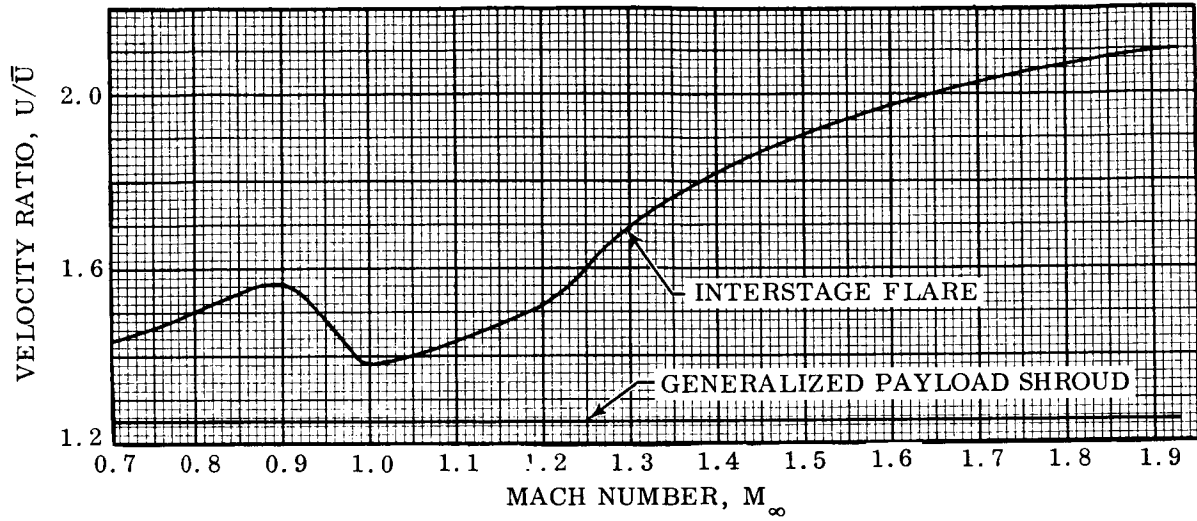


Fig. B-4 SA-203 Separated-Flow Velocity Ratio at $\alpha = 0, 4^\circ$, and 8°

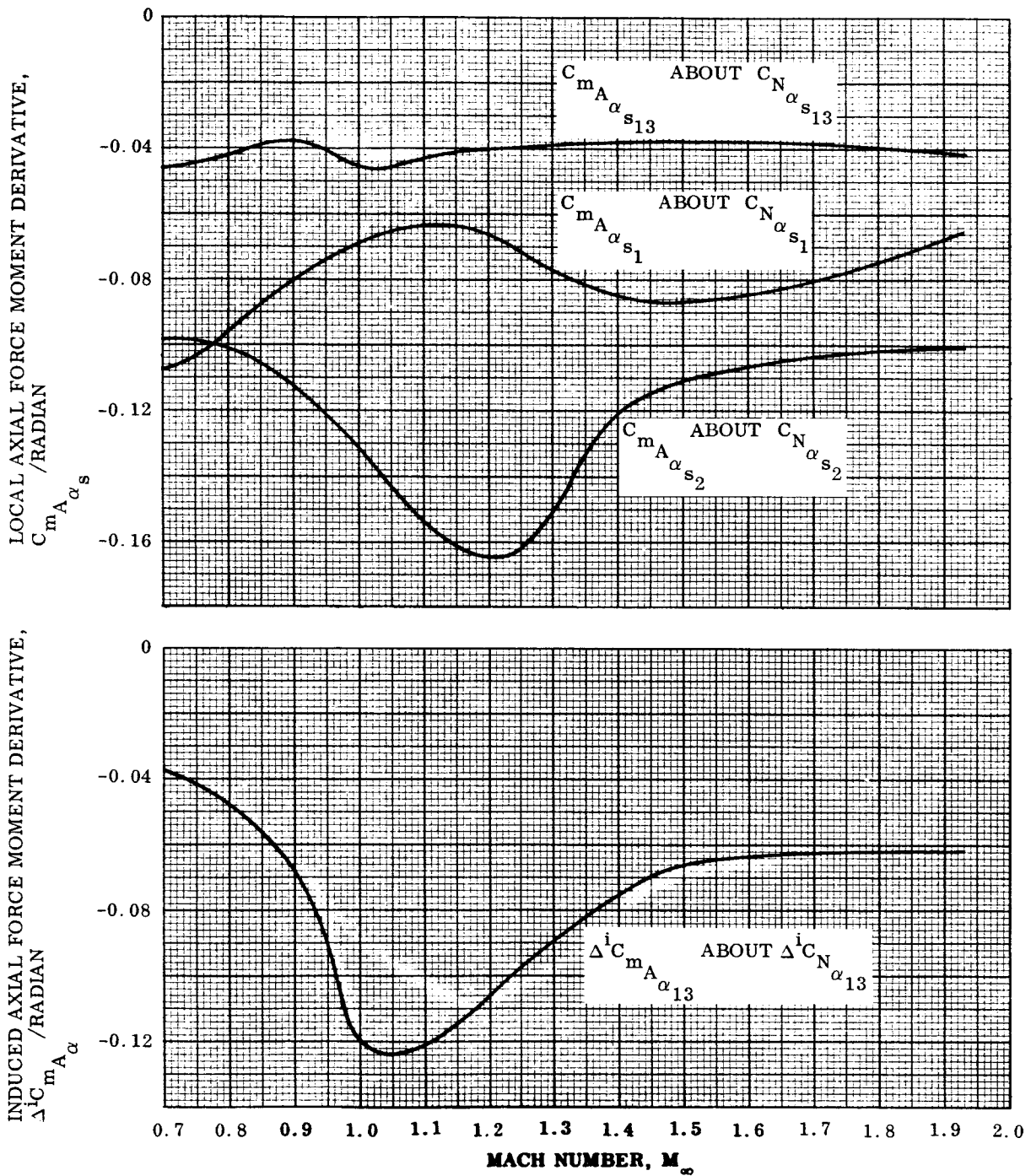
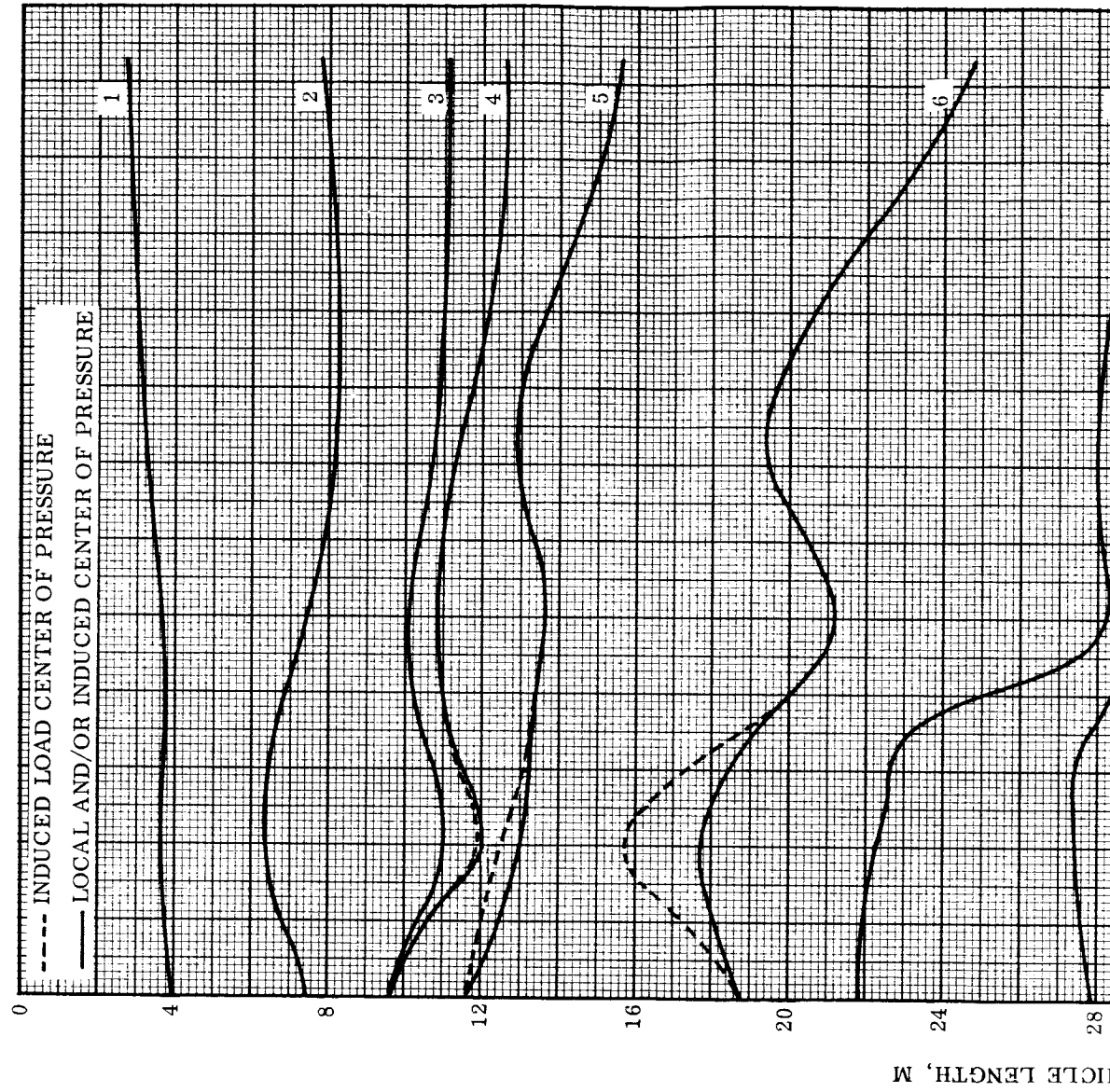
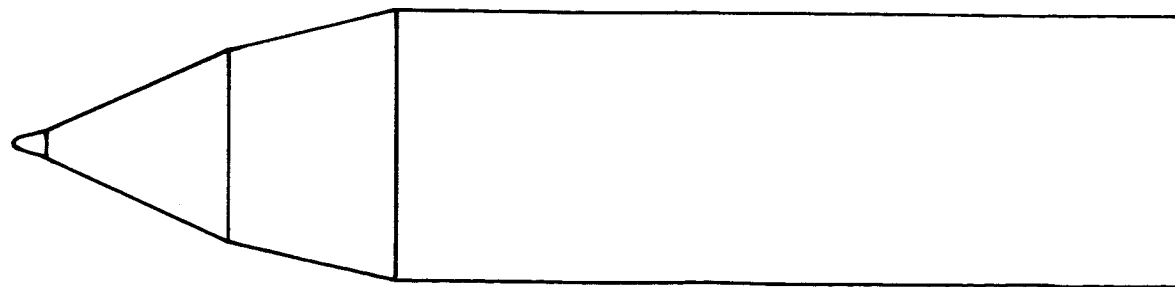
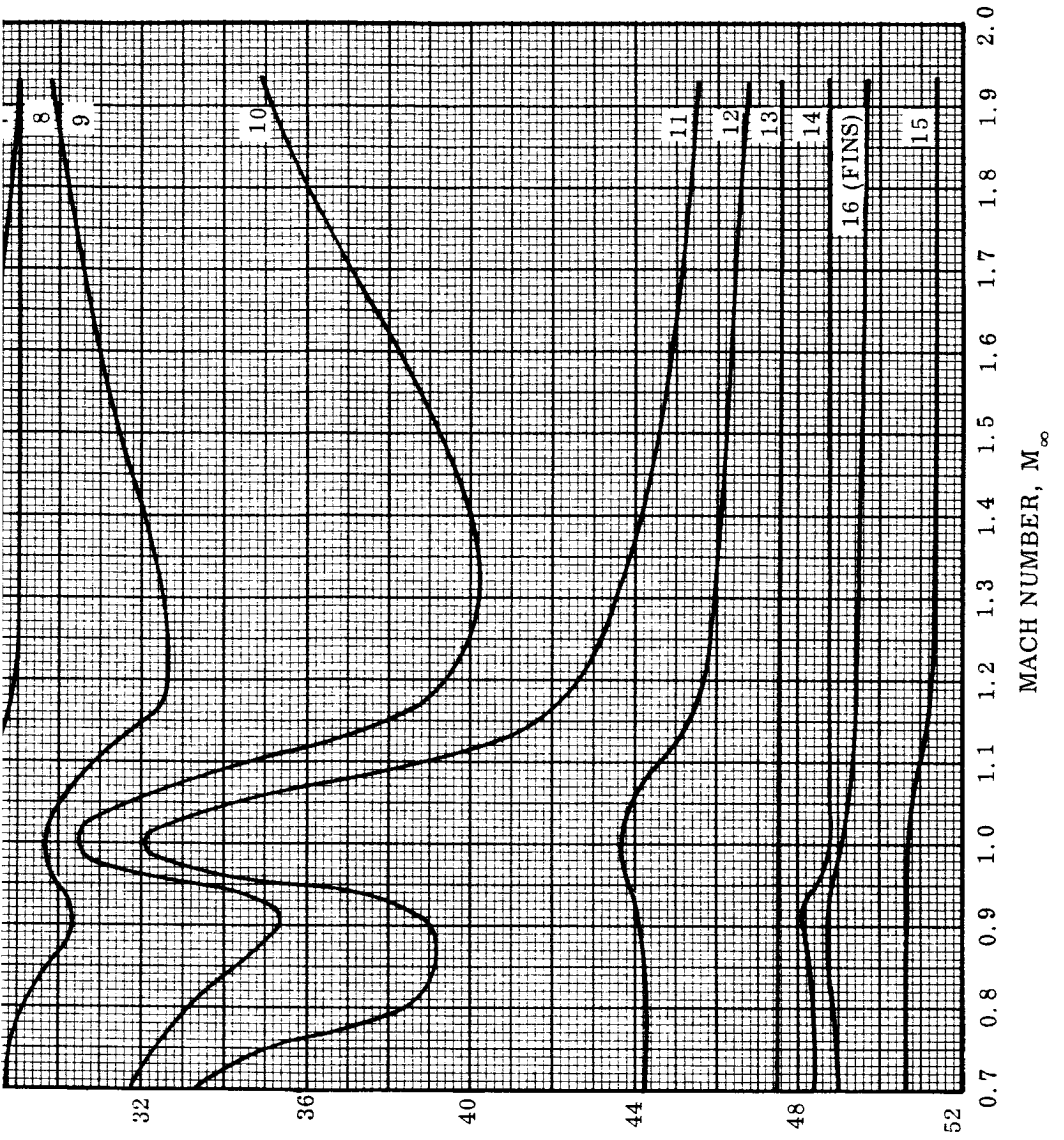


Fig. B-5 SA-203 Local and Induced Nose-Shroud and Interstage-Flare Axial-Force Moment Derivatives at $\alpha = 0$



B-9



EA

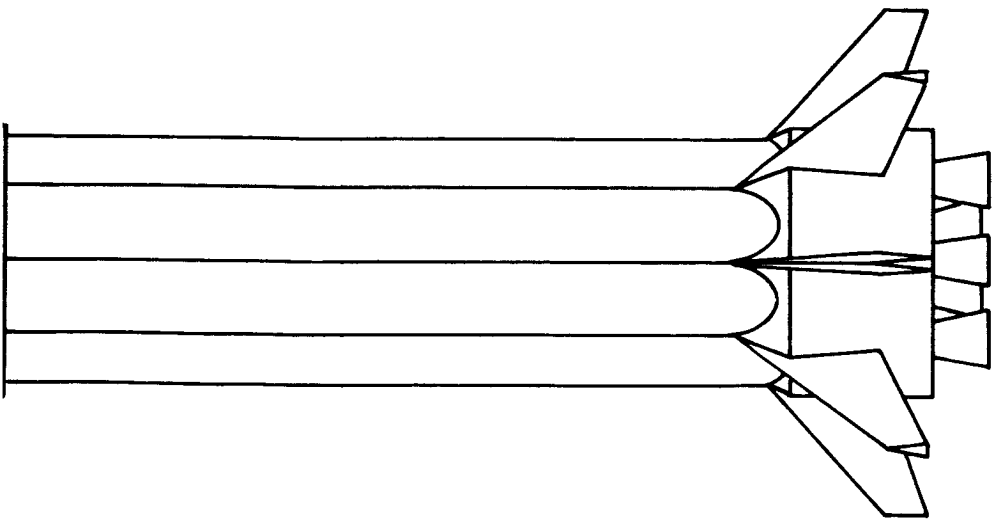


Fig. B-6 SA-203 Lumped-Load Centers of Pressure at $\alpha = 0$

B-10

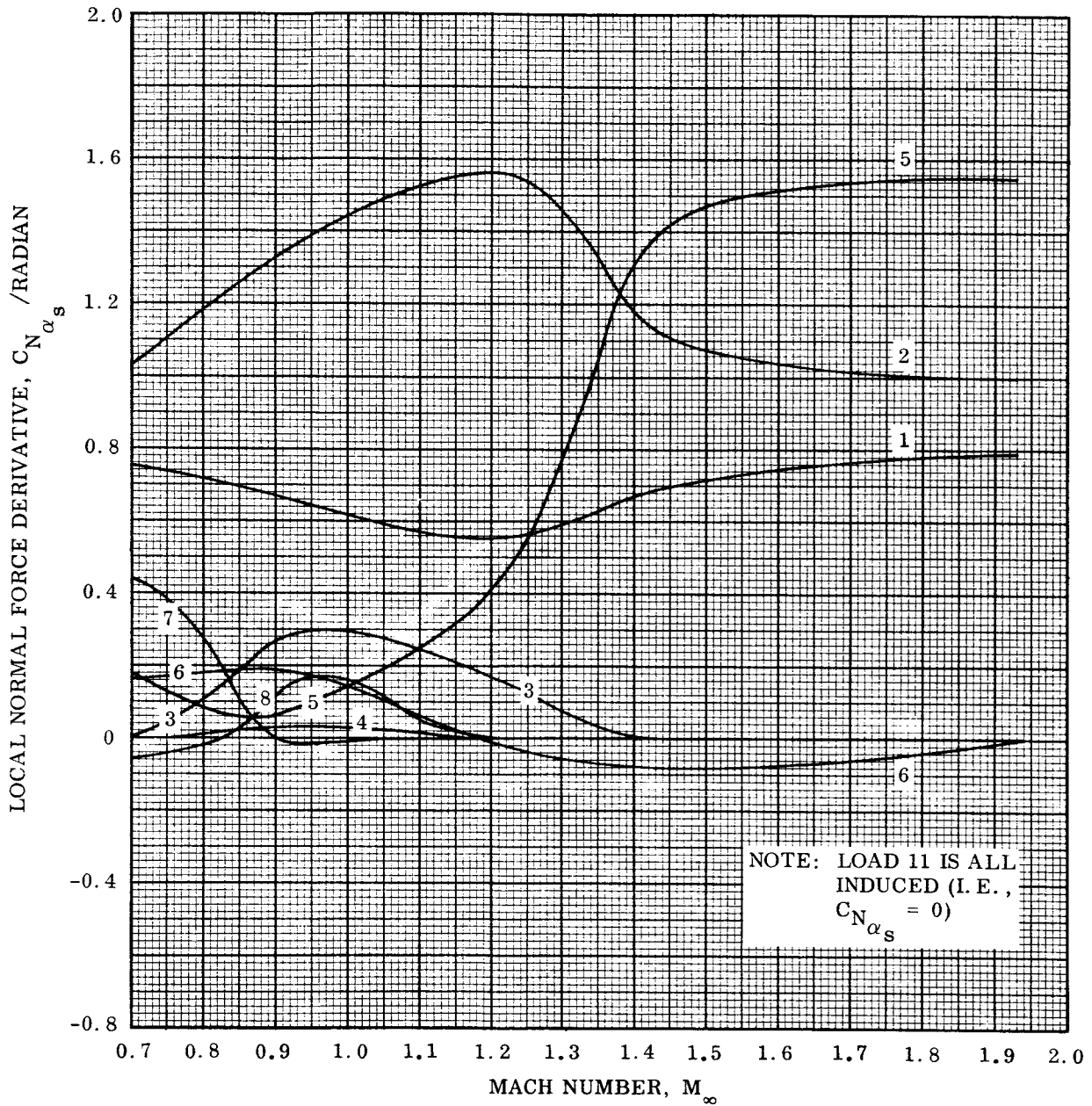


Fig. B-7 SA-203 Local Normal Force Derivatives at $\alpha = 4^\circ$

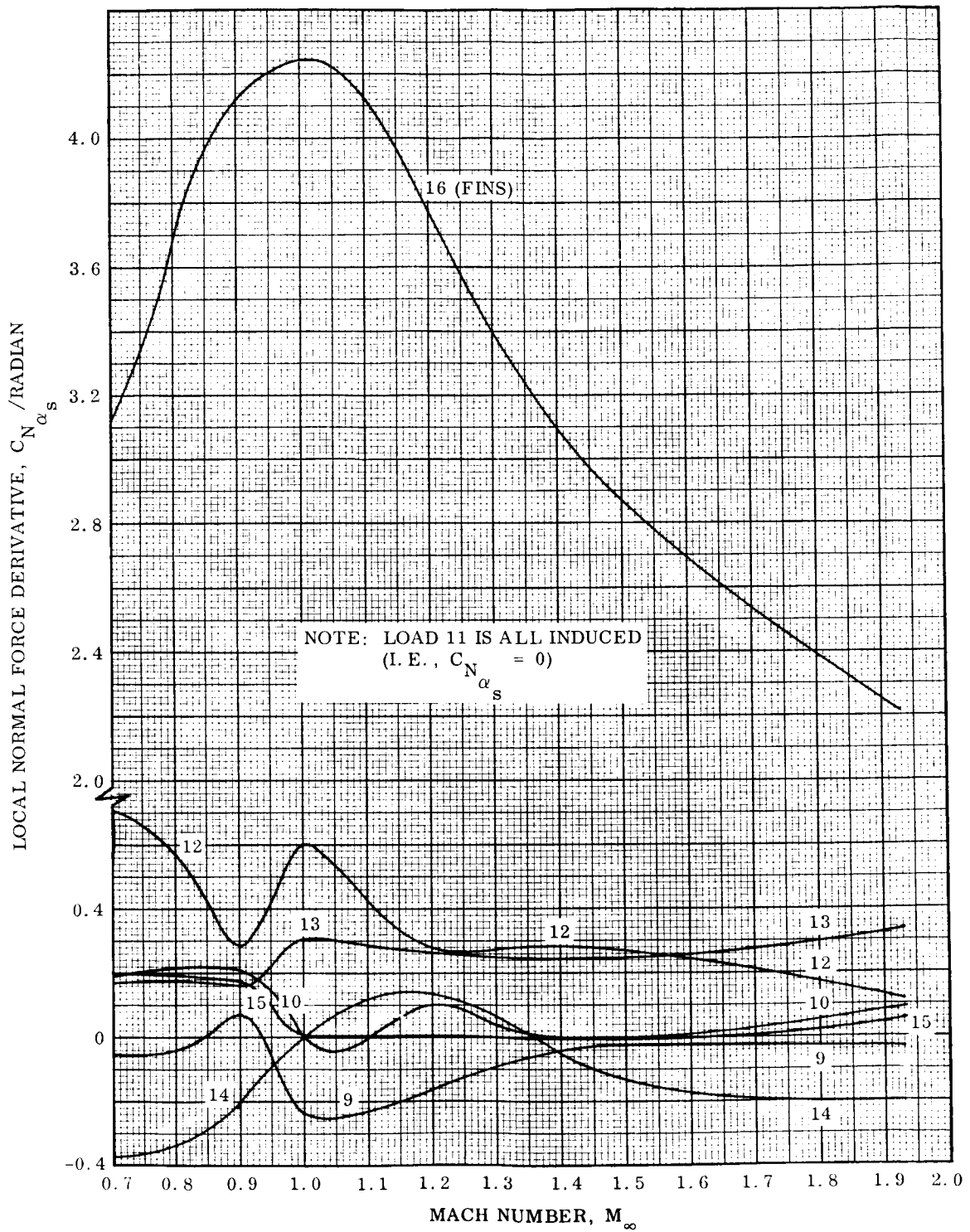


Fig. B-7 SA-203 Local Normal Force Derivatives at $\alpha = 4^\circ$ (Cont.)

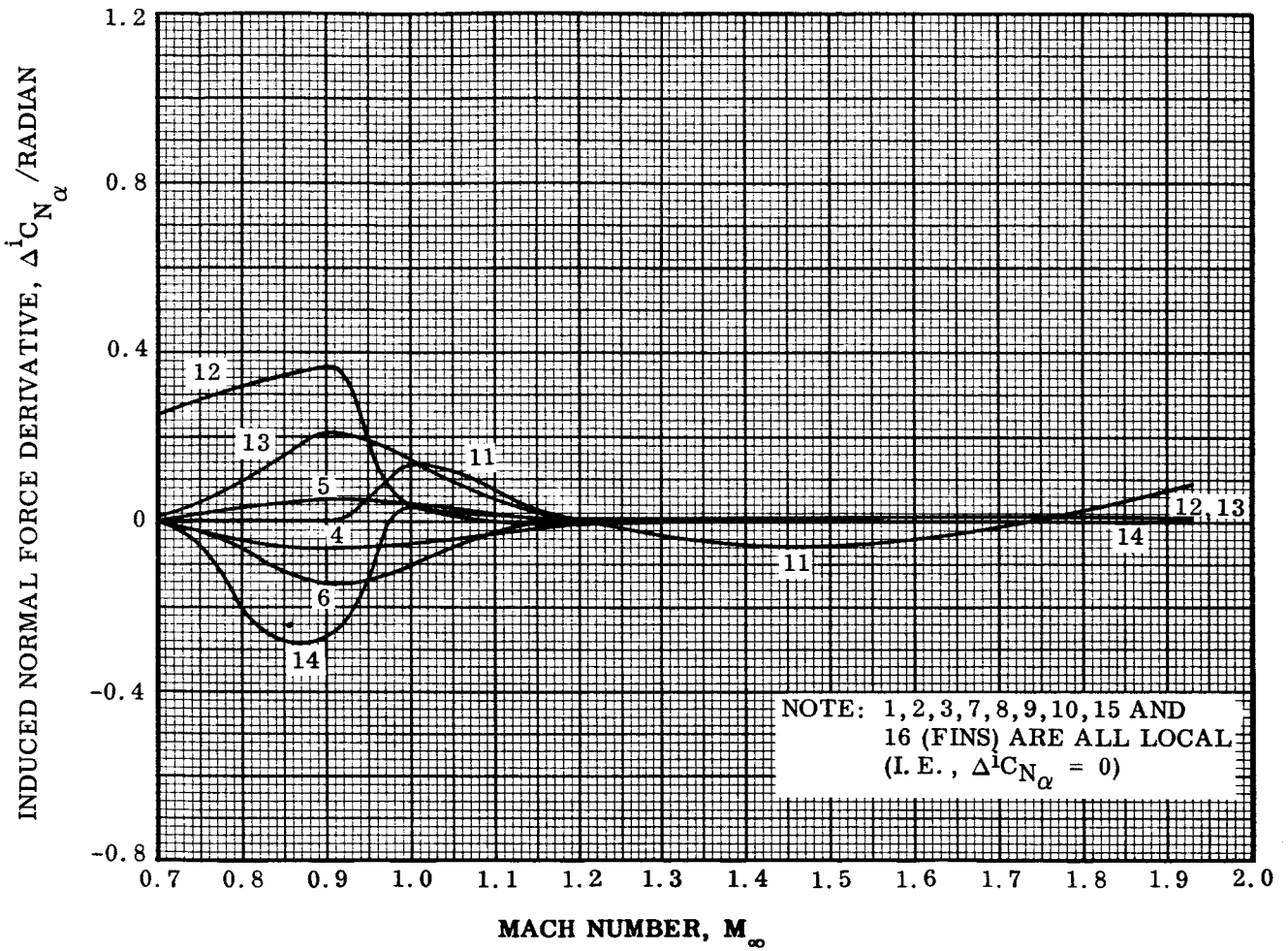


Fig. B-8 SA-203 Induced Normal Force Derivatives at $\alpha = 4^\circ$

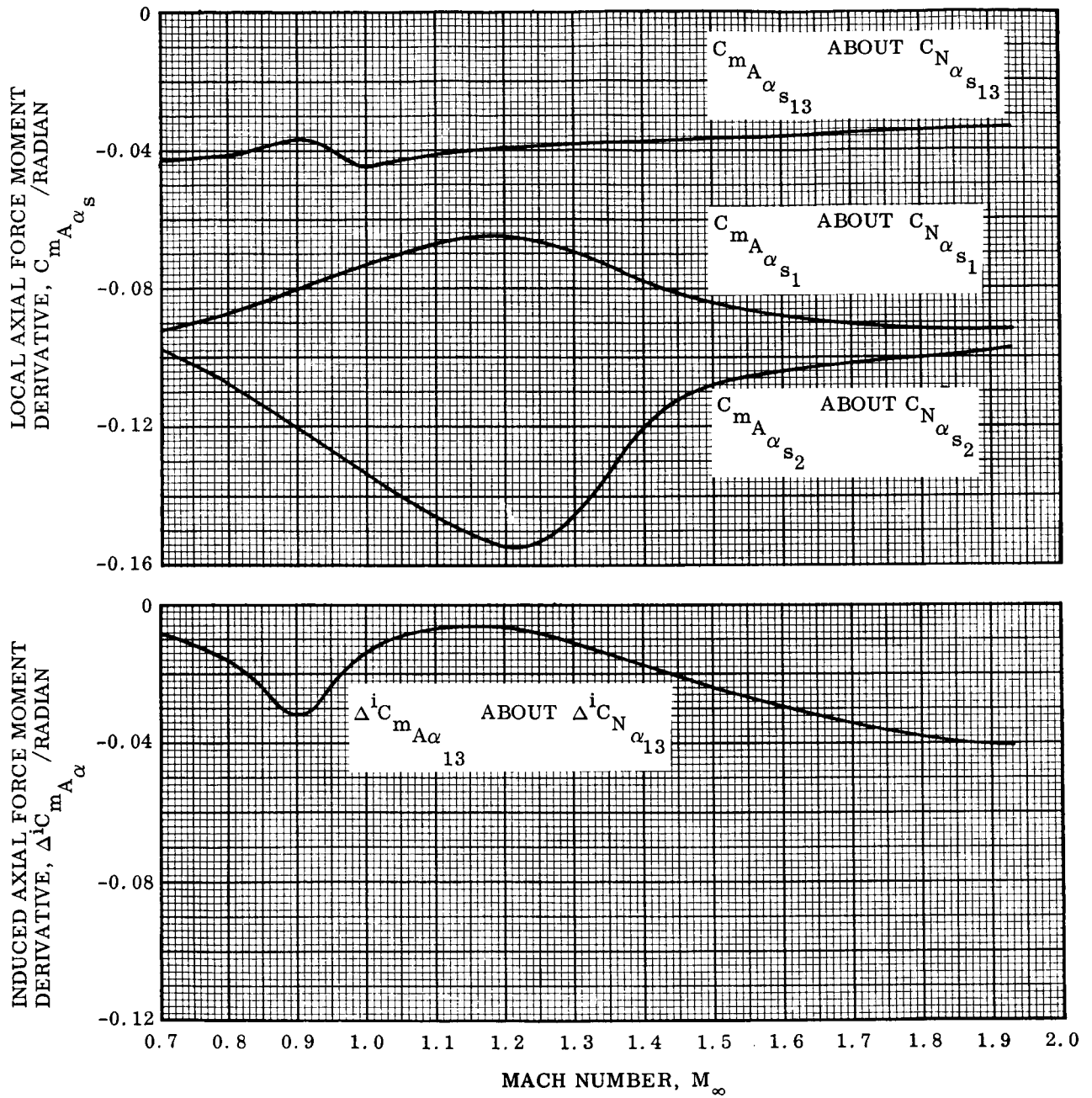
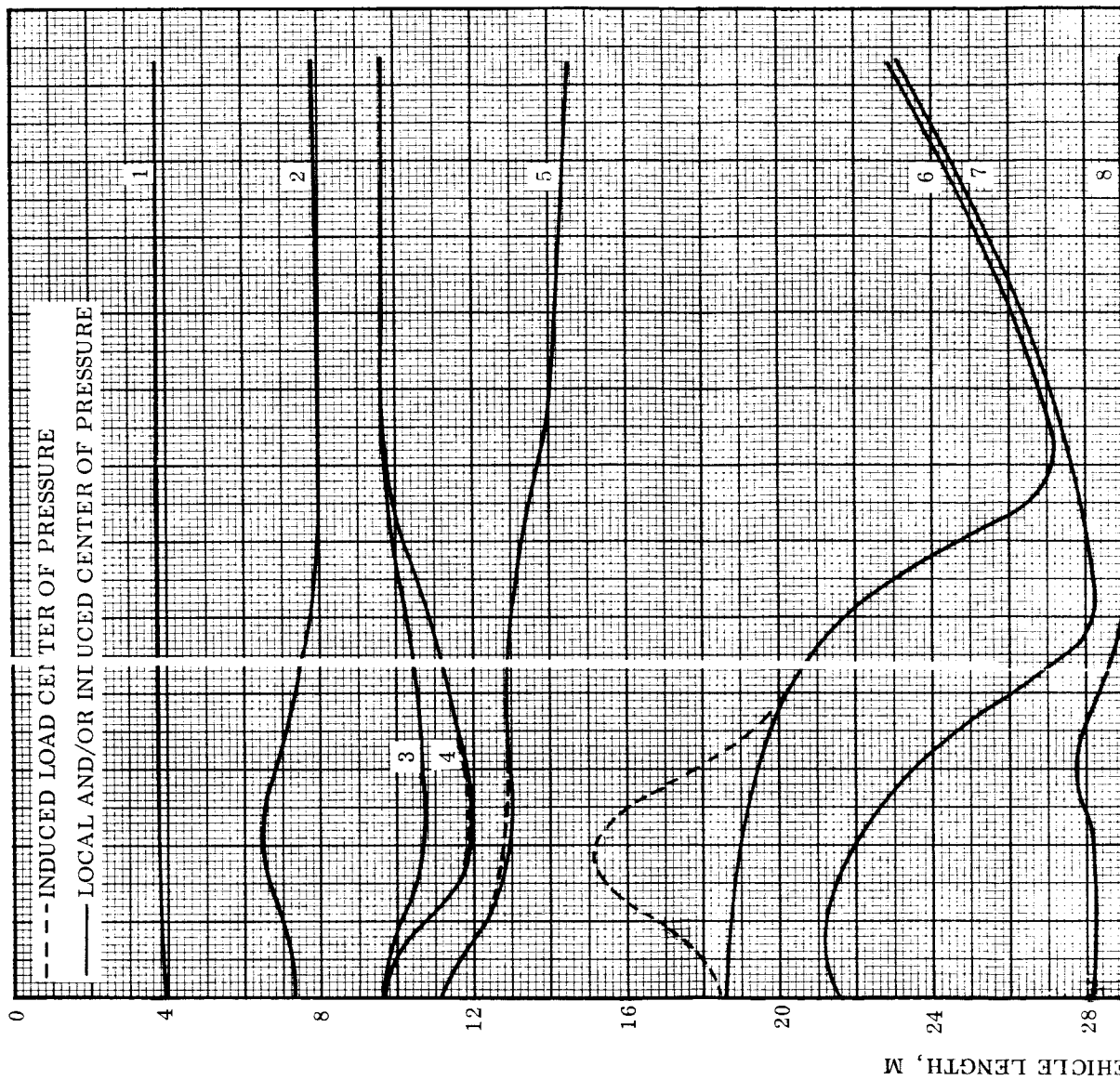
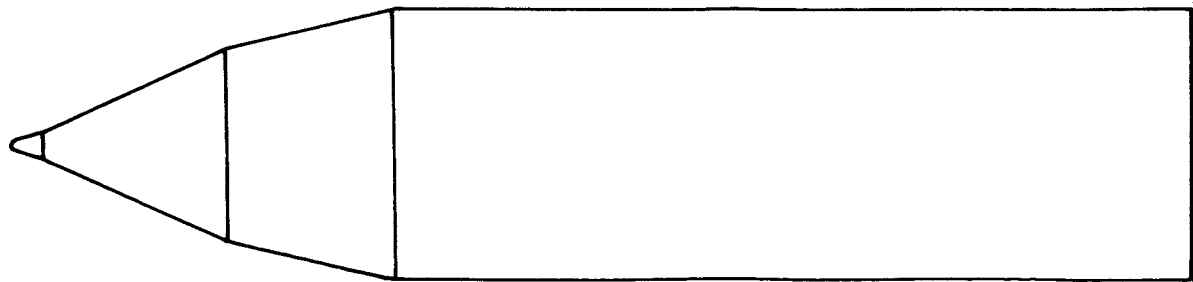
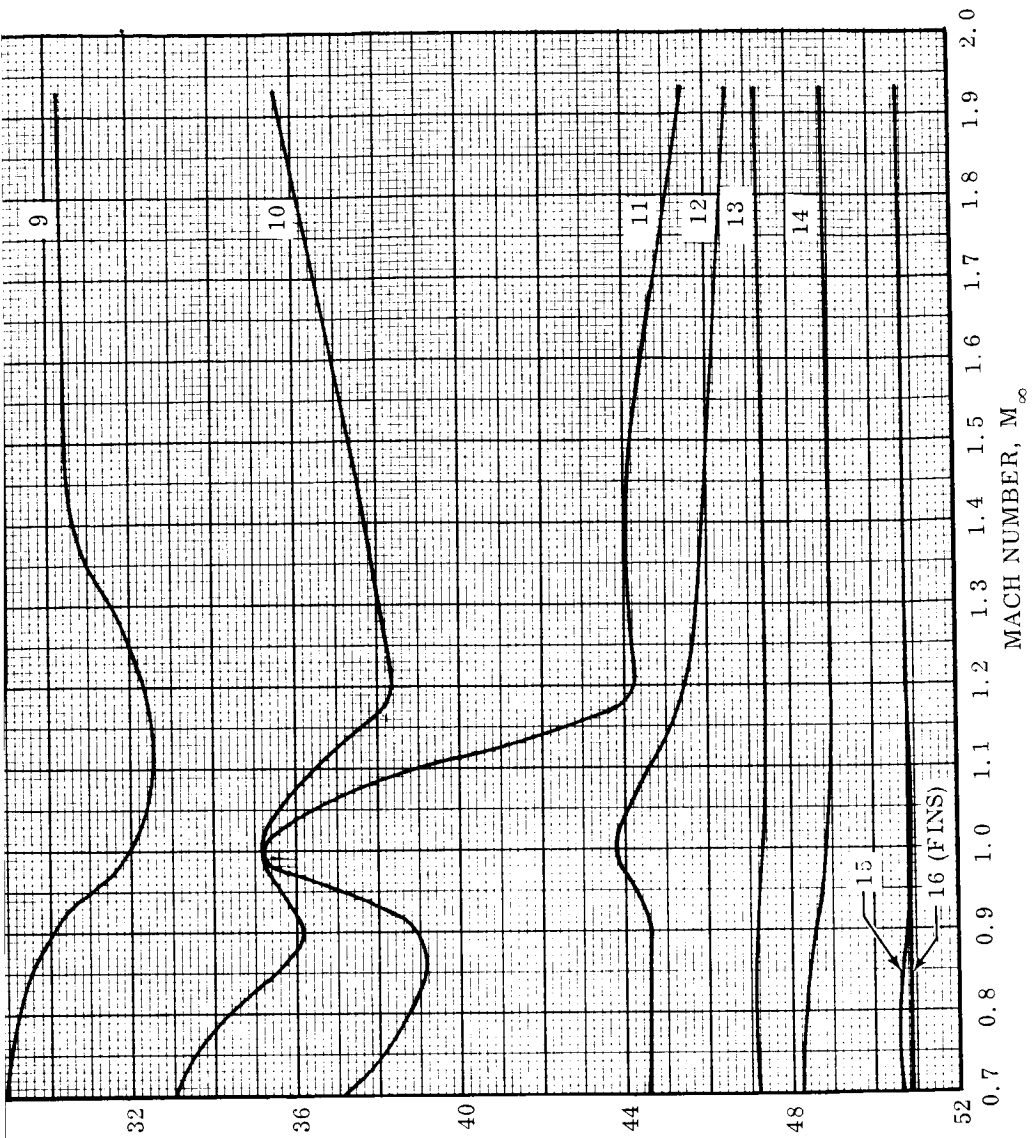


Fig. B-9 SA-293 Local and Induced Nose-Shroud and Interstage-Flare Axial-Force Moment Derivatives at $\alpha = 4^\circ$



B-15



IA

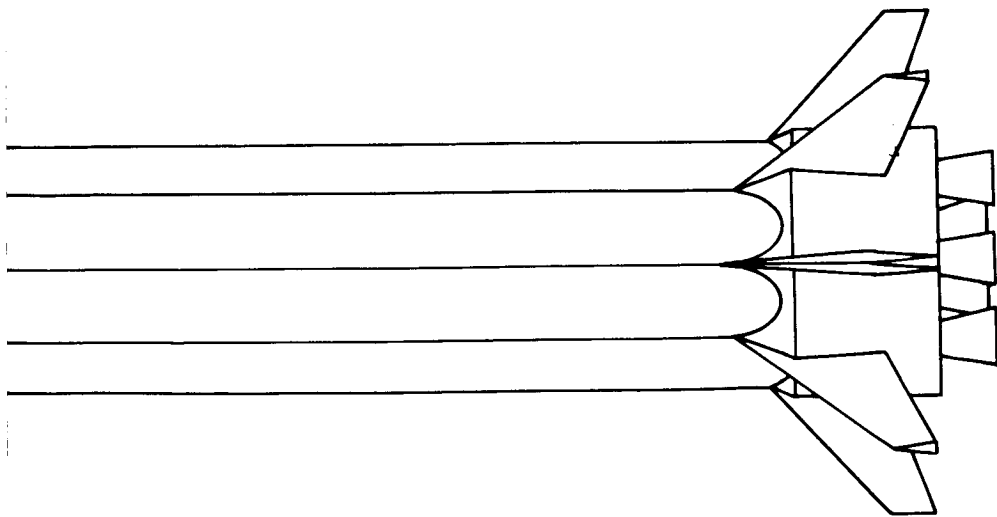


Fig. B-10 SA-203 Lumped-Load Centers of Pressure at $\alpha = 4^\circ$

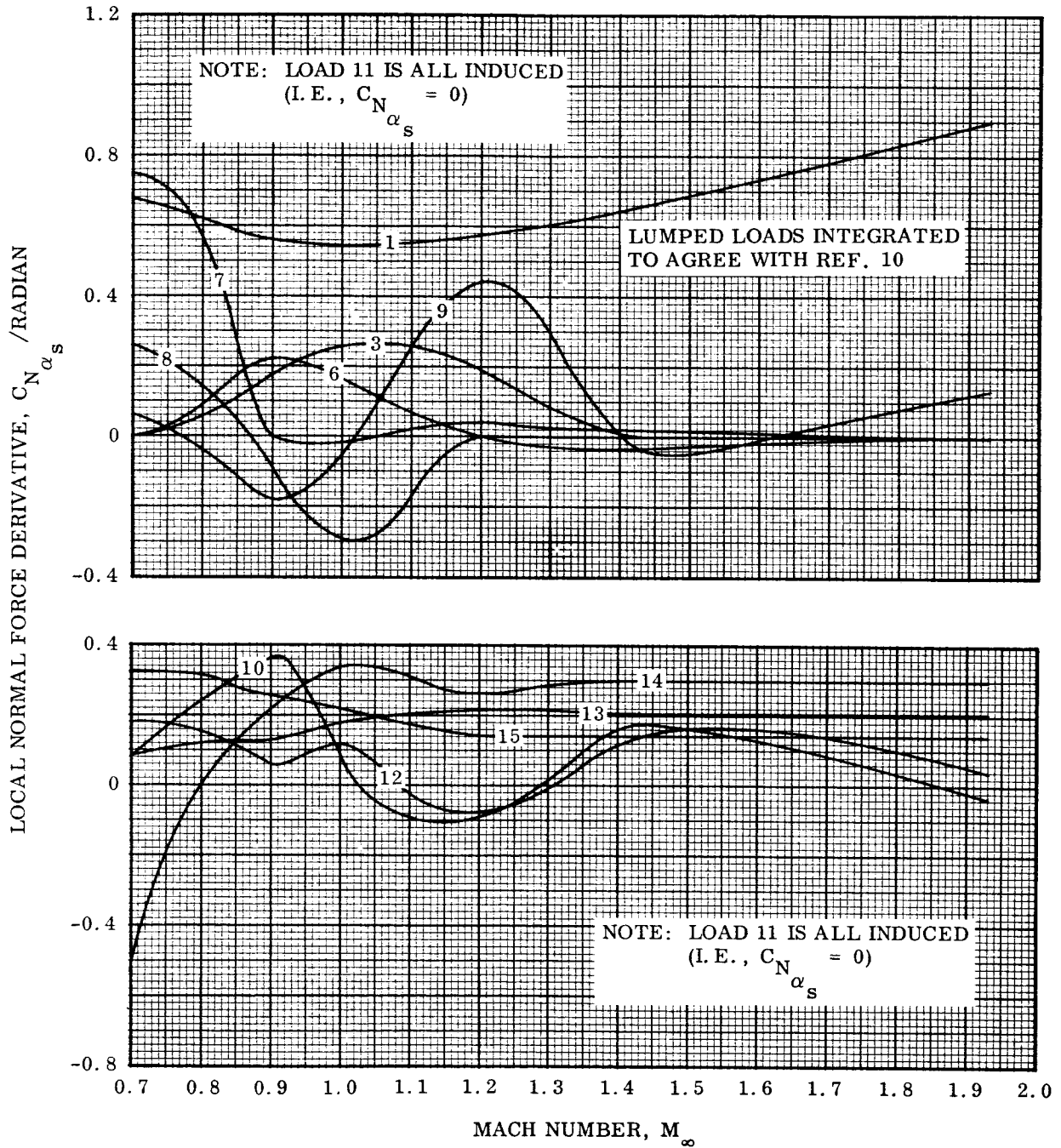


Fig. B-11 SA-203 Local Normal Force Derivatives at $\alpha = 8^\circ$

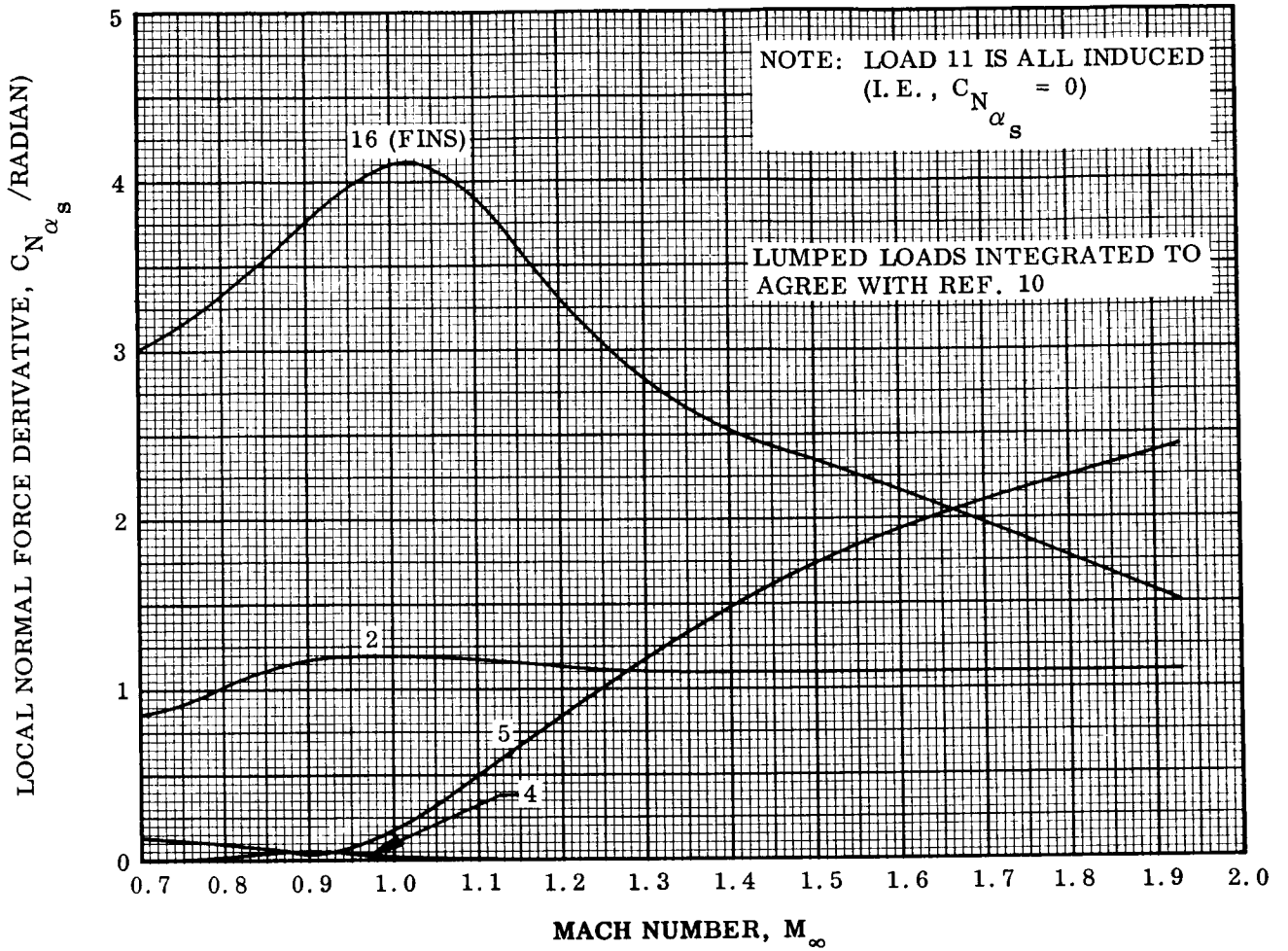


Fig. B-11 SA-203 Local Normal Force Derivatives at $\alpha = 8^\circ$ (Cont.)

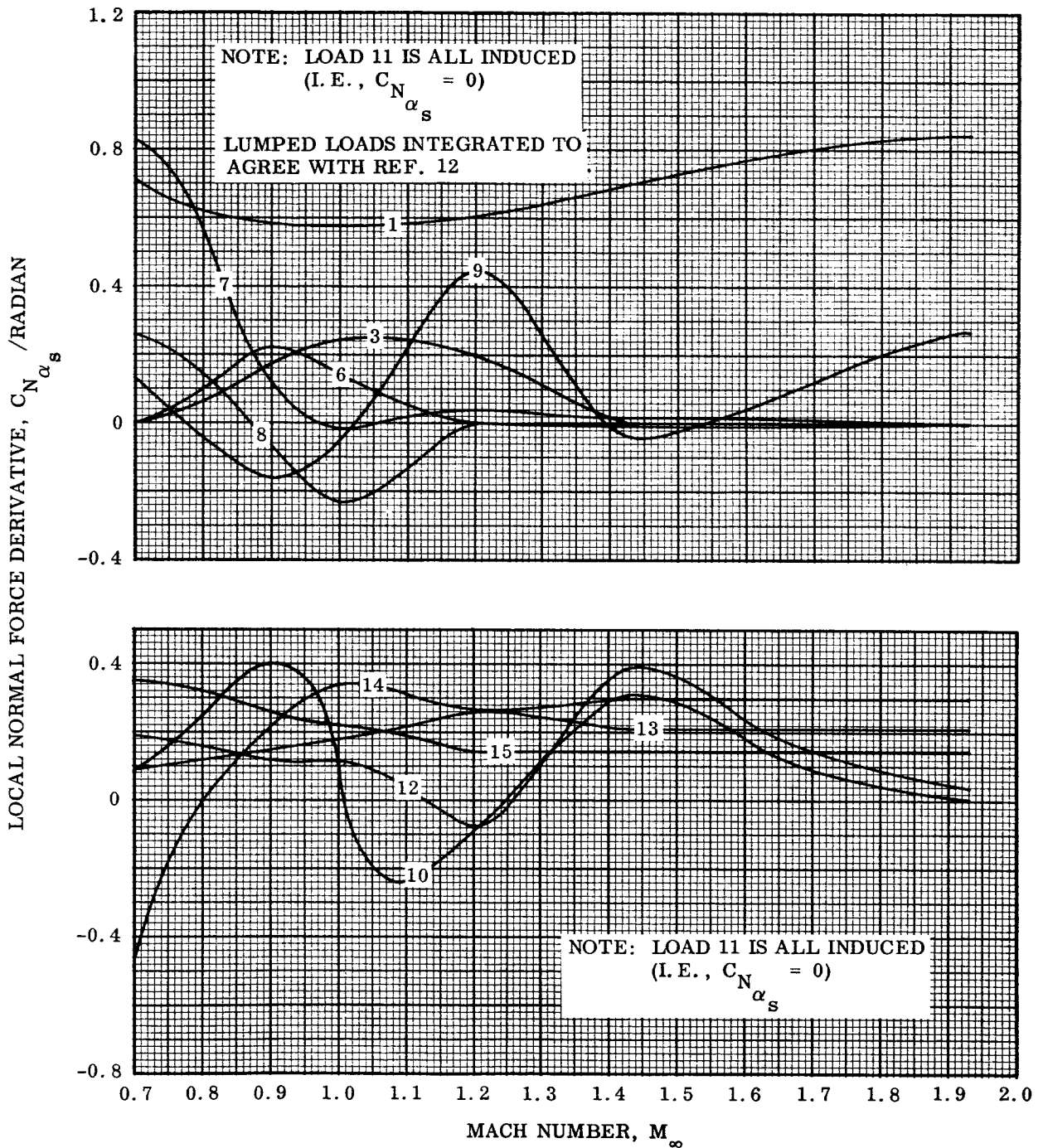
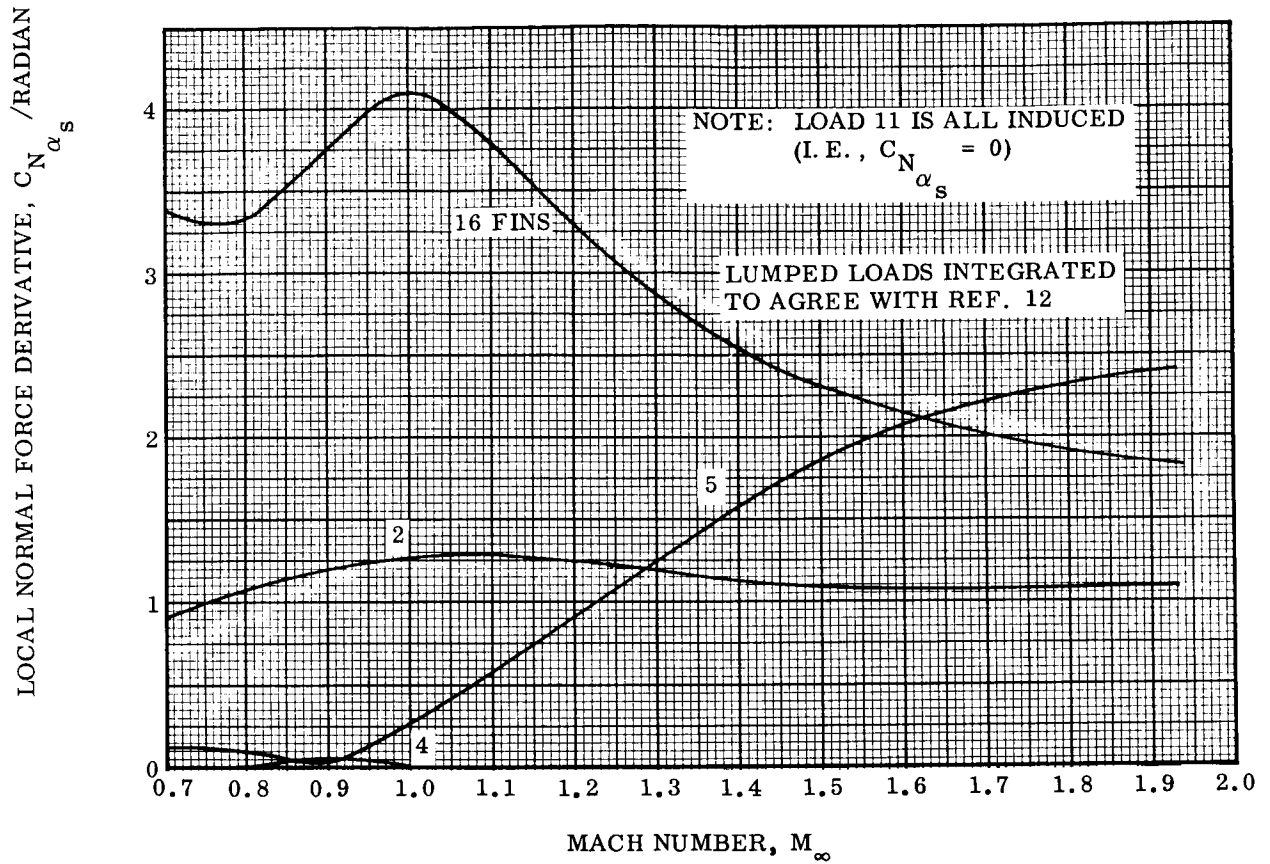


Fig. B-11 SA-203 Local Normal Force Derivatives at $\alpha = 8^\circ$ (Cont.)

Fig. B-11 SA-203 Local Normal Force Derivatives at $\alpha = 8^\circ$ (Cont.)

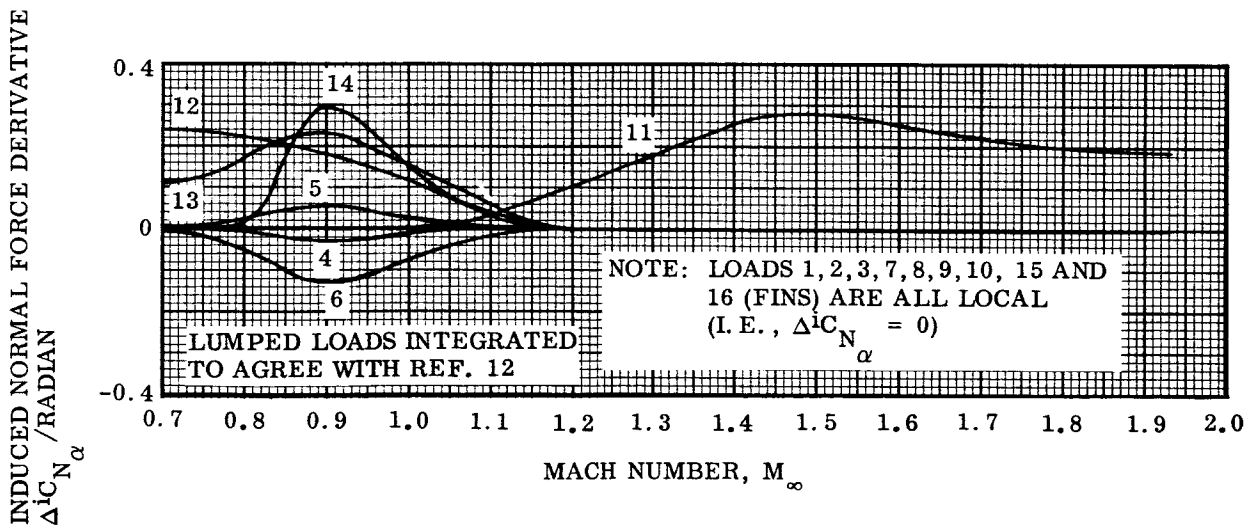
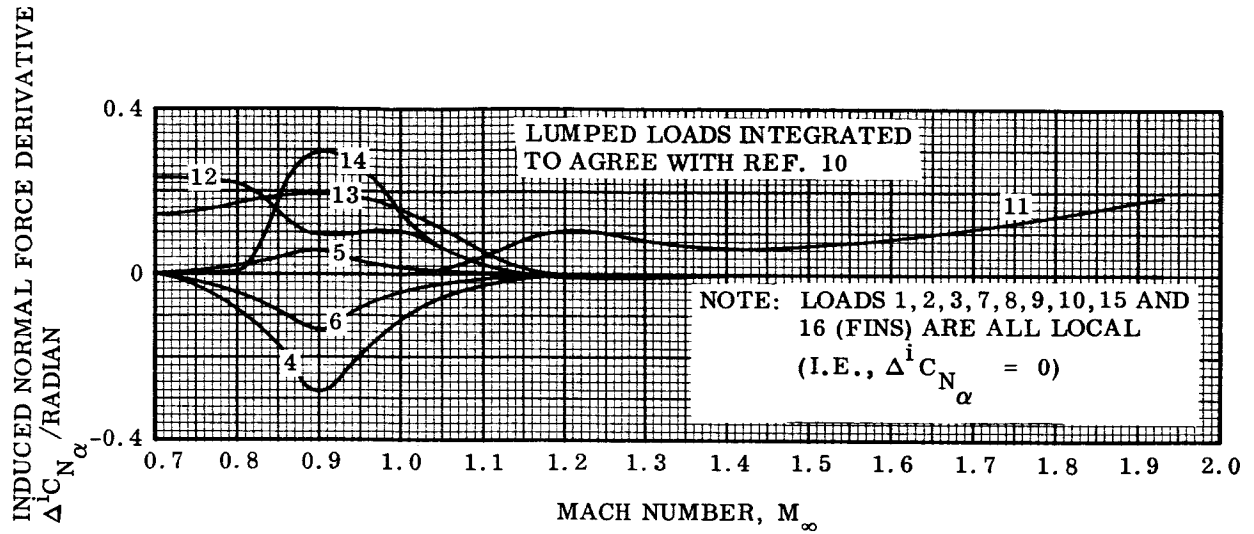


Fig. B-12 SA-203 Induced Normal Force Derivatives at $\alpha = 8^\circ$

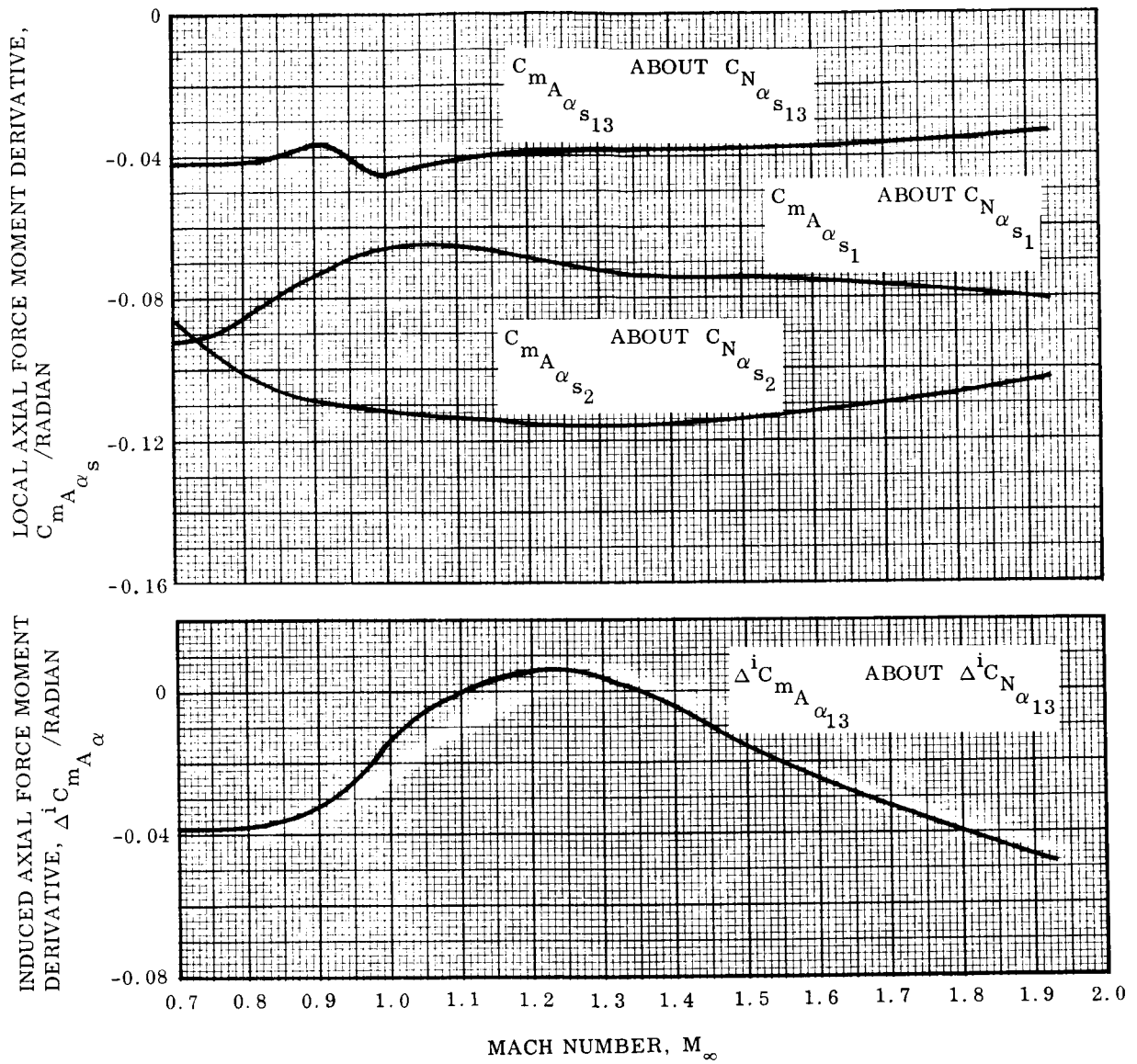
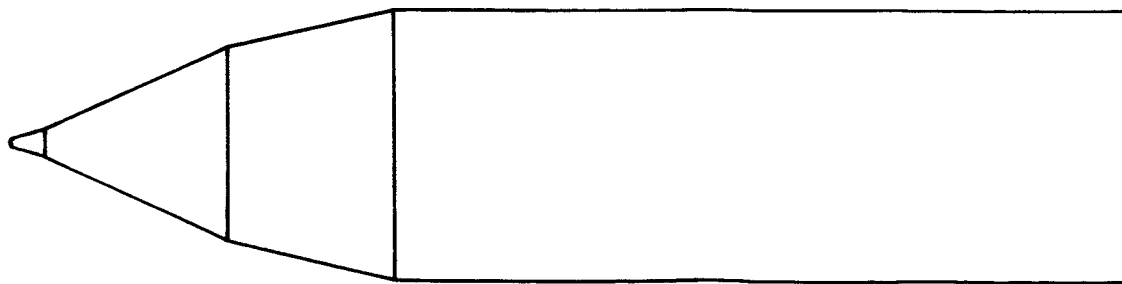
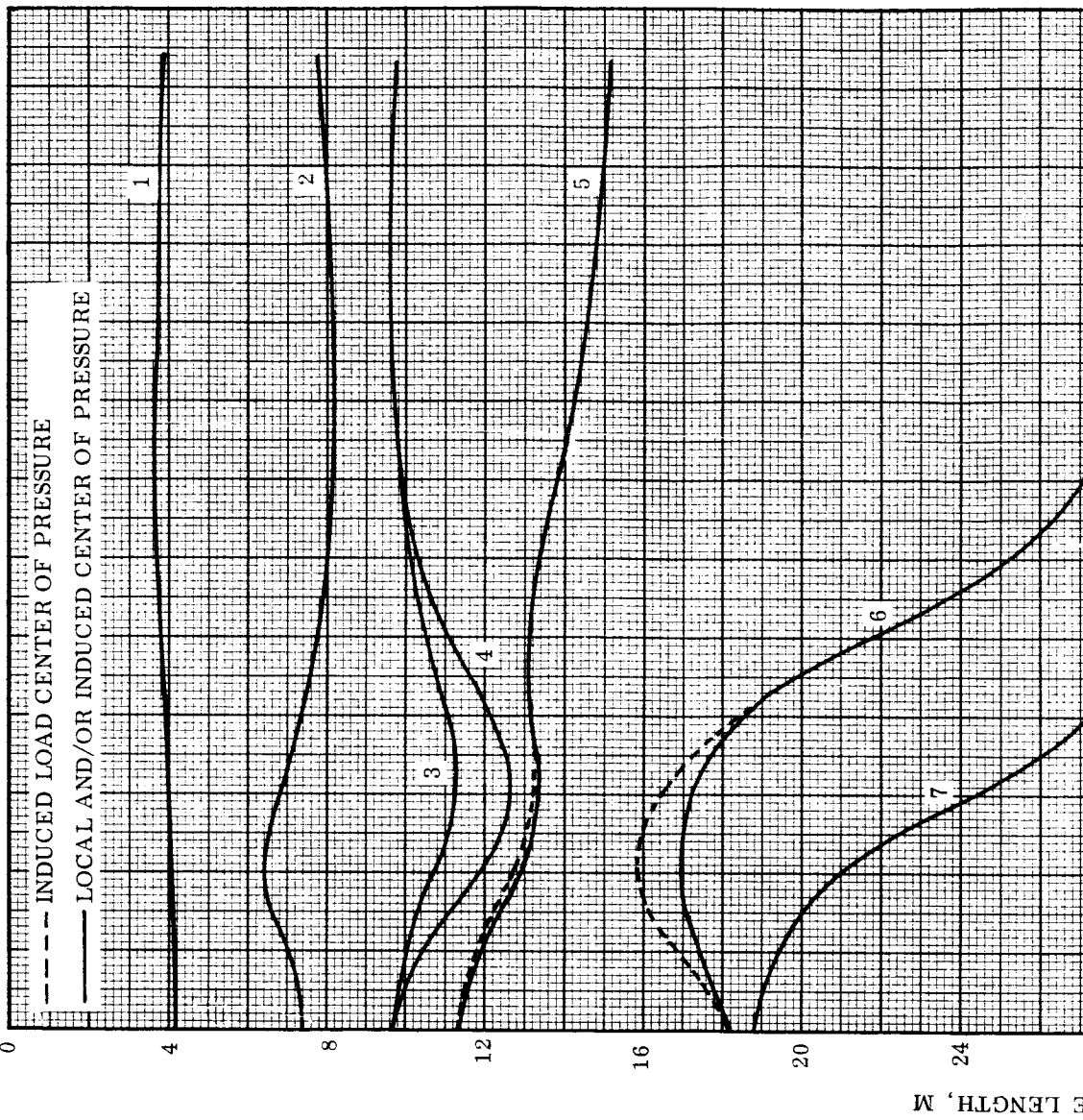


Fig. B-13 SA-203 Local and Induced Nose-Shroud and Interstage-Flare Axial-Force Moment Derivatives at $\alpha = 8^\circ$



B-23

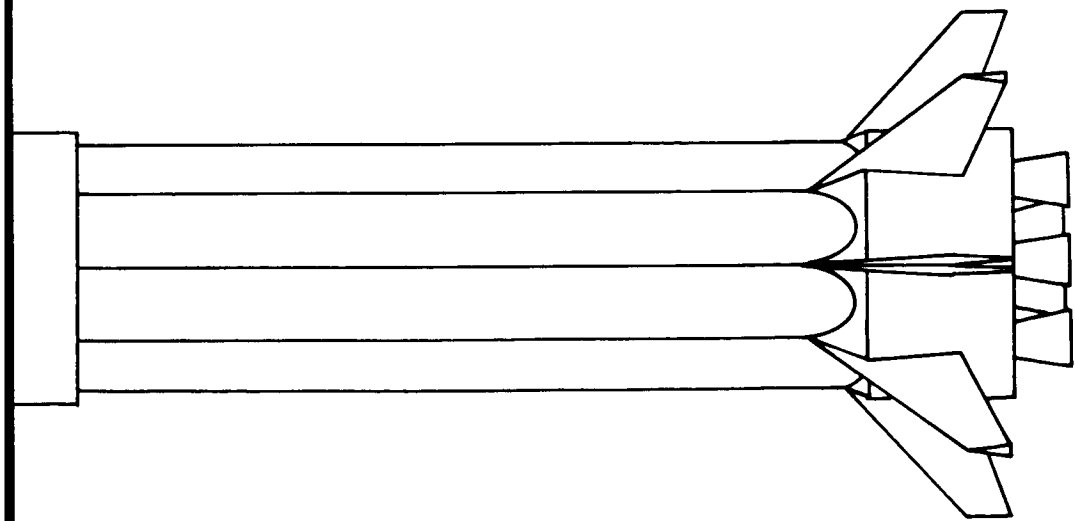
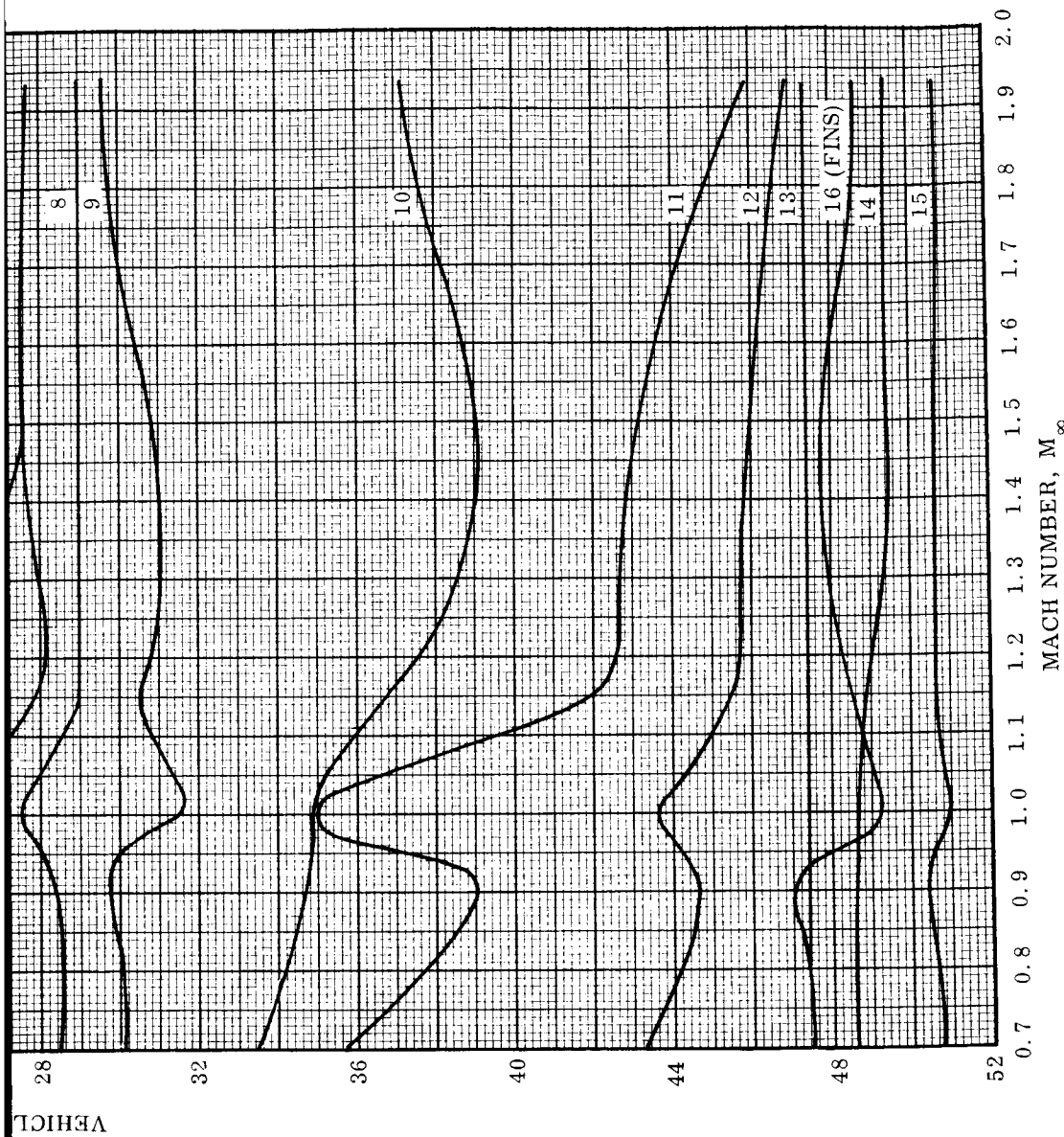


Fig. B-14 SA-203 Lumped-Load Centers of Pressure at $\alpha = 8^\circ$

~~SECRET~~
B-24

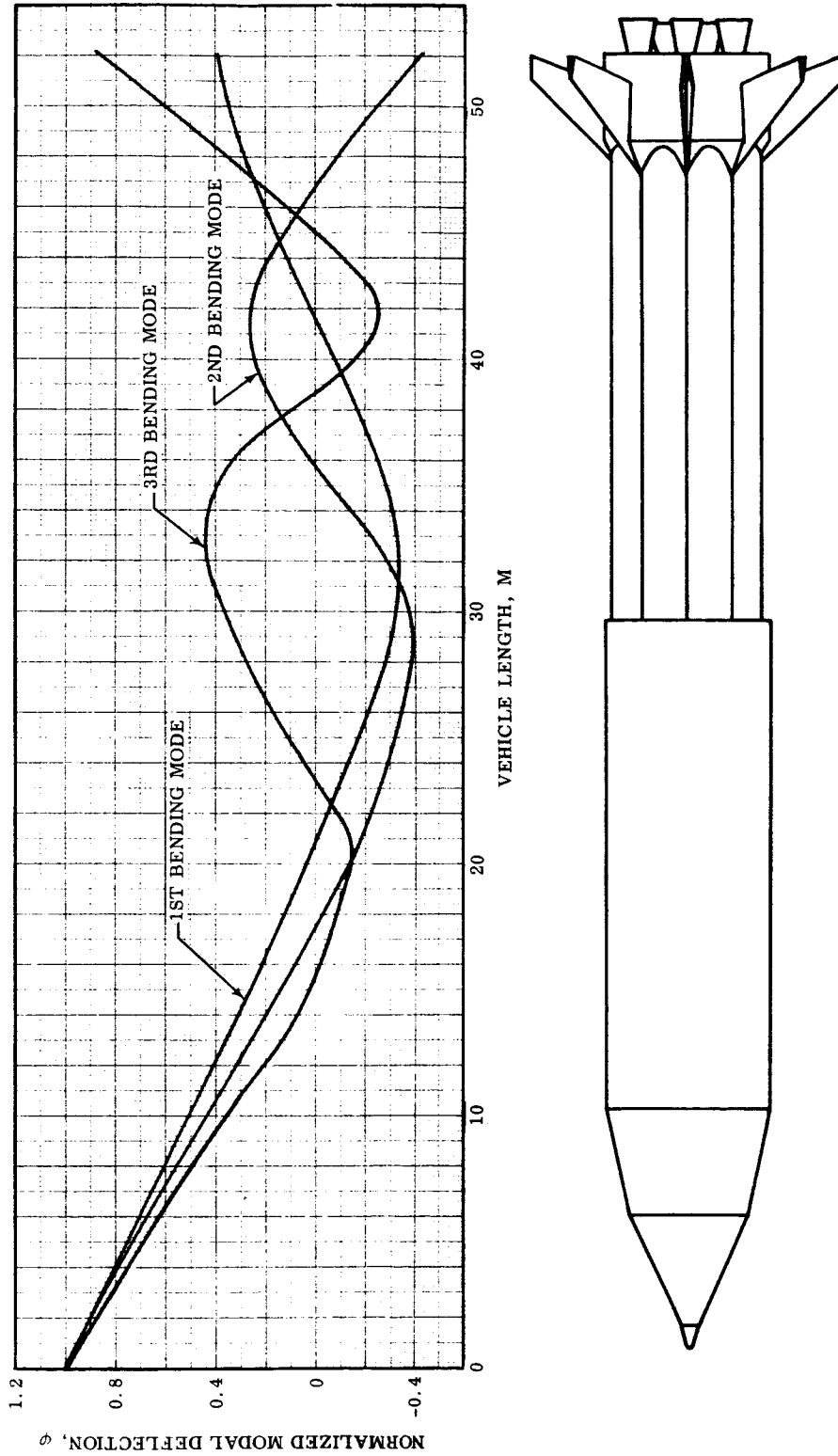


Fig. B-15 SA-203 Normalized Free-Free Bending-Mode Shapes

Appendix C

AEROELASTIC EFFECTS OF BOUNDARY LAYER-TERMINAL
SHOCK INTERACTION

C.1 INTRODUCTION

Slender cone-cylinder forebodies usually do not cause the aerodynamicist or dynamicist any problems. However, there is one somewhat frustrating exception. If a launch vehicle during the subsonic portion of its ascent reaches appreciable trim angles of attack (e.g., due to gusts) aeroelastic instability may result even for payloads with cone half angles below 15 degrees. The flow phenomenon responsible for this was first discovered by Robertson and Chevalier (Refs. 15-17). They discussed, however, only the buffet input, i.e., the forcing function, and did not concern themselves with the other half of the problem as it presents itself to the aeroelastician. That is, they did not consider the vehicle response. The gross bending response of the vehicle is not critically dependent upon the buffet input per se, but rather on the aerodynamic undamping caused by the separated flow pattern that produces the buffet input.

C.2 STATEMENT OF PROBLEM

Reviewing the experimental data obtained by Robertson and Chevalier (Ref. 16), the following distinct characteristics are found. At high subsonic speeds a terminal shock appears downstream of the cone-cylinder shoulder causing local boundary layer separation (Fig. C-1). When the angle of attack is increased to 4 degrees, the leeward side separation jumps forward to the cone shoulder. The tremendous jumpwise load change can best be appreciated by comparing it with the pressure change when the angle of attack is increased from zero to $\alpha = 2^\circ$. It is easy to see that this load will not change the rigid body moment (aft C.G.) as much as the bending moment of the elastic body (forward node). This jumpwise load change poses the most serious

aeroelastic problem, as will be demonstrated later. The jump to complete leeward side flow separation occurs at higher angle of attack the more slender the conical forebody is (Fig. C-2).

Figure C-3 shows another characteristic of the interaction between the terminal shock and the boundary layer. The leeward side shock moves forward of the windward side shock creating a negative cylinder load. This loading also has an adverse aeroelastic effect, as will be demonstrated, but it is insignificant compared to the jumpwise load change. The terminal shock moves back with increasing Mach number and with increasing cone angle (Figs. C-4 and C-5). In Fig. C-6 the opposite effects of increasing Mach number and increasing angle of attack are illustrated using a carpet plot (Ref. 24).

Assuming that the terminal shock strength is unchanged for small changes in angle of attack the shock-boundary layer interaction will only be governed by how the approaching boundary layer is affected by forebody crossflow and external flow velocity gradient. On the leeward side, an increasing angle of attack will produce an increasingly thick boundary layer as well as an increasingly adverse pressure gradient. The consequently weakened boundary layer profile cannot negotiate the pressure jump through the shock. Hence, the shock moves forward to a location where the boundary layer is strong enough to accept it (Figs. C-3 and C-6). In proximity to the cone-cylinder shoulder no such location can be found, and the shock jumps all the way forward to the shoulder causing the sudden and complete flow separation on the leeward side.

In the unsteady case both the boundary layer build-up and the external flow velocity gradient will be affected by the body pitching or bending (only one degree of freedom motions are analyzed here). The unsteady effect of boundary layer build-up has been described earlier for flare-shock induced boundary layer separations at low supersonic speeds (Ref. 2). The effect of velocity gradient changes through body pitching, the accelerated flow effect, requires, however, its own treatment.*

*For the geometries considered in Ref. 2 the accelerated flow effect is negligibly small compared with the downstream time lag effects in the crossflow influence on the boundary layer.

The pressure gradient of the external flow at the edge of the boundary layer is given by the complete Bernoulli equation

$$-\frac{1}{\rho_e} \frac{\partial p_e}{\partial x_1} = \frac{\partial U_e}{\partial t} + U_e \frac{\partial U_e}{\partial x_1} \quad (\text{C. 1})$$

Or with $\xi = \frac{x_1}{c}$

(c = reference length, e. g. cylinder caliber)

$$\frac{\partial p_e}{\partial \xi} = -\rho_e U_e \left[\frac{\partial U_e}{\partial t} \frac{c}{U_e} + \frac{\partial U_e}{\partial \xi} \right] \quad (\text{C. 2})$$

For constant vehicle velocity, U_e changed only through body pitching or bending. Thus,

$$\begin{aligned} \frac{\partial p_e}{\partial \xi} &= -\rho_e U_e \left[\frac{\partial U_e}{\partial \alpha} \frac{c \dot{\alpha}}{U_e} + \frac{\partial U_e}{\partial \xi} \right] \\ &= -\rho_e \frac{\partial}{\partial \alpha} \left(U_e^2/2 \right) \cdot \frac{c \dot{\alpha}}{U_e} - \rho_e \frac{\partial}{\partial \xi} \left(U_e^2/2 \right) \end{aligned}$$

i. e.,

$$\frac{\partial p_e}{\partial \xi} = \frac{\partial p_e}{\partial \alpha} \frac{c \dot{\alpha}}{U_e} + \frac{\partial p_e}{\partial \xi} \quad (\text{C. 3})$$

That is,

$$\frac{\partial p_e}{\partial \xi} = \left(\frac{\partial p_e}{\partial \xi} \right)_{\dot{\alpha}=0} + \frac{\partial p_e}{\partial \alpha} \cdot \frac{c \dot{\alpha}}{U_e} \quad (\text{C. 4})$$

or,

$$\frac{\partial C_{p_e}}{\partial \xi} = \left(\frac{\partial C_{p_e}}{\partial \xi} \right)_{\dot{\alpha}=0} + \frac{\partial C_{p_e}}{\partial \alpha} \cdot \frac{c\dot{\alpha}}{U_e} \quad (C.5)$$

For Prandtl-Meyer expansion, $\partial C_{p_e} / \partial \alpha$ is obtained as

$$\frac{\partial C_{p_e}}{\partial \alpha} = \frac{\partial}{\partial \alpha} \left(\frac{p_e - p_\infty}{\frac{\gamma}{2} M_\infty^2 p_\infty} \right) = - \frac{1}{\frac{\gamma}{2} M_\infty^2} \frac{\partial}{\partial \nu} \left(\frac{p_e}{p_\infty} \right) \quad (C.6)$$

i. e. ,

$$\frac{\partial C_{p_e}}{\partial \alpha} = -2 \left(\frac{M_e}{M_\infty} \right)^2 (M_e^2 - 1)^{-1/2}$$

e. g. ,

$$\left(\frac{\partial C_{p_e}}{\partial \alpha} \right)_{M_e = \sqrt{2}} = -4/M_\infty^2$$

Thus, the body pitching (or bending) motion, $c\dot{\alpha}/U > 0$, will decrease the pressure gradient $\partial C_{p_e} / \partial \xi$ and will, therefore, delay the boundary layer separation. That is, the separation will in the unsteady case lag behind its static or steady-state position. This lag, added to the lag in the boundary layer build-up, makes the separation have opposite effects on static and dynamic stability, and accounts for the sometimes drastic effect of the separation on vehicle dynamics.

C.3 ANALYTIC APPROACH

Quasi-steady methods are used to compute unsteady characteristics by use of experimental static characteristics (Ref. 2). The treatment of the boundary layer build-up effect in Ref. 2 is directly applicable to the present case. The quasi-steady means that accounts for the accelerated flow effect will be derived here.

Generally, the separation induced loading is determined solely by the shock motion. The shock strength remains constant within the approximations used here to compute first-order effects of the shock perturbations. The effect of body pitch on the external flow pressure gradient is given by Eq. (C.4) or Eq. (C.5). If the static force induced by a change in the pressure gradient were known, the unsteady force induced through the accelerated flow effect could be computed also. That is,

$$\Delta^i C_N(p_\xi) = \frac{\partial \Delta^i C_N}{\partial p_\xi} \frac{\partial p_\xi}{\partial \frac{c\dot{\alpha}}{U_e}} \frac{c\dot{\alpha}}{U_e} \quad (\text{C.7})$$

where, from Eq. (C.4)

$$\frac{\partial}{\partial \frac{c\dot{\alpha}}{U_e}} \left(\frac{\partial p_e}{\partial \xi} \right) = \frac{\partial p_\xi}{\partial \frac{c\dot{\alpha}}{U_e}} = \frac{\partial p}{\partial \alpha} \quad (\text{C.8})$$

$\Delta^i C_N$ results from the shock pressure increase ΔC_{p_s} acting over the projected area $\pi/4 \cdot c \cdot (\xi_{\text{windward}} - \xi_{\text{leeward}}) c$. With the reference area $S = \pi c^2/4$ the derivative $\partial \Delta^i C_N / \partial p_\xi$ becomes simply

$$\frac{\partial \Delta^i C_N}{\partial p_\xi} = \Delta C_{p_s} \frac{\partial \xi_s}{\partial p_\xi} \quad (\text{C.9})$$

Static experimental data can provide the sought derivatives, but not without considerable manipulations. The difficulty is to decouple boundary layer thickness effects, δ -effects, and effects of external flow pressure gradient, p_ξ -effects. All δ -effects are treated in the manner described in Ref. 2. How the p_ξ -effects are to be treated will be described.

One needs essentially to determine what the pressure gradient and shock position would have been in inviscid flow before one can differentiate between δ - and p_ξ -effects. The derivatives obtained directly from static experimental data include viscous effects; even with the assumption of constant shock strength the following multidependence still exists.

$$\frac{d\xi_s}{d\alpha} = \frac{\partial \xi_s}{\partial \delta} \frac{d\delta}{d\alpha} + \frac{\partial \xi_s}{\partial p_\xi} \frac{dp_\xi}{d\alpha} \quad (C. 10)$$

$$\frac{d\delta}{d\alpha} = \frac{\partial \delta}{\partial w_{AC}} \frac{dw_{AC}}{d\alpha} + \frac{\partial \delta}{\partial p_\xi} \frac{dp_\xi}{d\alpha}^* \quad (C. 11)$$

$$\frac{dp_\xi}{d\alpha} = \left(\frac{\partial p_\xi}{\partial \alpha} \right)_{\text{inviscid}} + \frac{\partial p_\xi}{\partial \delta} \frac{d\delta}{d\alpha} \quad (C. 12)$$

Even when $\partial \delta / \partial p_\xi$ in Eq. (C.11) is neglected, which is permissible within the framework of first-order effects sought here, the necessary separation of variables requires rather extensive analysis. The results of such an analysis (Ref. 18) will be discussed briefly.

* w_{AC} is the crossflow at the aerodynamic center upstream of the shock position. That is, forebody crossflow effects on the boundary layer build-up are lumped in the manner described in Ref. 2.

C.4 TERMINAL SHOCK AERODYNAMICS

The viscous effects, i. e., the effect of the boundary layer separation, is to move the terminal shock forward from its position in inviscid flow (Fig. C-7). This effect is largest at $M_\infty = 0.88$ and increases with increasing cone angle θ_c . When the shock moves closer to the cone cylinder shoulder with decreasing M_∞ (Fig. C-8), the effect of the boundary layer build-up, the δ -effect, decreases and has disappeared at $M_\infty = 0.86$ (for 20° cone angle)*. The shock movement is then determined only by the changing external flow pressure gradient represented by $\partial \Delta^i_{\xi_s} / \partial \theta_c$ in Fig. C-8. The force derivative induced by this shock movement is shown in Fig. C-9, as obtained by use of the shock pressure jump ΔC_{p_s} and an equation equivalent to Eq. (C.9).

That is,

$$\left(\frac{\partial \Delta^i C_N}{\partial \alpha} \right)_\delta = \Delta C_{p_s} \left(\frac{\partial \Delta^i_{\xi_s}}{\partial \alpha} \right)_\delta \quad (C.13)$$

$$\left(\frac{\partial \Delta^i C_N}{\partial \alpha} \right)_{p_\xi} = \Delta C_{p_s} \left(\frac{\partial \Delta^i_{\xi_s}}{\partial \alpha} \right)_{p_\xi} \quad (C.14)$$

The derivative $dp_\xi / d\theta_c$ can be obtained (Ref. 18) and, thus, $\left(\partial \Delta^i_{\xi_s} / \partial (p_\xi)_s \right)$ can be determined. The results are shown in Fig. C-10. For high cone angles $\left(\partial (p_\xi)_s / \partial \alpha \right)_\delta$ can apparently be obtained directly from static data. However, the boundary layer build-up effect $\left(\partial (p_\xi)_s / \partial \alpha \right)_{p_\xi}$ completely cancels the inviscid pressure gradient effect for slender cones. Prändtl-Meyer expansion over-estimates the derivative $\left(\partial (p_\xi)_s / \partial \alpha \right)_\delta$ by 10 to 20 percent.

*The 20° cone-cylinder body provides the more detailed information of the bodies tested in Ref. 16, and is therefore used here as the typical body.

When the shock approaches the cone-cylinder shoulder it will suddenly jump all the way forward to the shoulder. The cause is the weak boundary layer resulting from the very steep adverse pressure gradient at the shoulder. This is well illustrated by use of the boundary layer shape parameter, as was done by Robertson and Chevalier (Ref. 16 and Fig. C-11). The 30° cone-cylinder illustrates how the leeward side on the 20° cone-cylinder would appear at a moderate angle of attack. Their further research (Ref. 17) revealed that the flow could alternate between retarded shock induced separation and complete separation. Their results, shown in Fig. C-12, indicate that this jump from one flow condition to another could occur for a fixed model (within sting stiffness limitations) in a large $M_\infty - \alpha$ - region. For the blunter nose cones, only the windward side had this alternating flow; on the slender 15° cone-cylinder body, only the leeward side had it.

If the cone-cylinder body is describing pitch oscillations, $\theta(t)$, around a certain trim angle of attack, α_0 , the motion of the terminal shock can be described as follows, using quasi-steady methodology. (See Fig. C-13, Sketch 1.)

With $U(M_\infty)$ constant

$$\xi_s(t) = \xi_s(\alpha_0) + (\xi_s)_{\text{inv.}} (\alpha_0 + \theta(t)) + \Delta^i \xi_s(t)$$

$$\Delta^i \xi_s(t) = \left(\frac{\partial \Delta^i \xi_s}{\partial \alpha} \right)_{p_\xi} \cdot \tilde{\alpha}_{AC}(t - \Delta t) + \left(\frac{\partial \Delta^i \xi_s}{\partial (p_\xi)_s} \right) \left[\left(\frac{\partial (p_\xi)_s}{\partial \alpha} \right)_\delta \cdot \tilde{\alpha}_s(t) + \left(\frac{\partial p_s}{\partial \alpha} \right)_\delta \frac{c\dot{\theta}}{(U_e)_s} \right]^*$$

(C.15)

$$\left. \begin{aligned} \tilde{\alpha}_{AC}(t - \Delta t) &= \theta(t - \Delta t) + (\xi_{AC} - \bar{\xi}) \frac{c\dot{\theta}(t - \Delta t)}{U} \\ \tilde{\alpha}_s(t) &= \theta(t) + (\xi_s - \bar{\xi}) \frac{c\dot{\theta}(t)}{U} \end{aligned} \right\} \quad \text{(C.16)}$$

*Only $\Delta^i \xi_s(t)$ is of interest here, as the inviscid shock position is assumed to adjust instantaneously to θ and can be included in the attached flow characteristics.

For slow oscillations [i.e., for rigid body oscillations and bending oscillations in third or lower bending modes (Ref. 5)]

$$\begin{aligned}\tilde{\alpha}_{AC}(t - \Delta t) &= \theta(t) - \Delta t \dot{\theta}(t) + (\xi_{AC} - \bar{\xi}) \frac{c\dot{\theta}(t)}{U} \\ &= \theta - \left(\frac{U\Delta t}{c} + \bar{\xi} - \xi_{AC} \right) \frac{c\dot{\theta}}{U}\end{aligned}\quad (C.17)$$

$$\Delta t = (\xi_s - \xi_{AC}) c/\bar{U}$$

$\bar{U} \approx 0.8U$ [Convection velocity in turbulent boundary layer at subsonic and transonic speeds (Ref. 25).] Thus Eq. (C.15) becomes

$$\begin{aligned}\Delta^i_{\xi_s}(t) &= \left(\frac{\partial \Delta^i_{\xi_s}}{\partial \alpha} \right)_{p_\xi} \left\{ \theta - \left[1.25 (\xi_s - \xi_{AC}) + \bar{\xi} - \xi_{AC} \right] \frac{c\dot{\theta}}{U} \right\} \\ &+ \left(\frac{\partial \Delta^i_{\xi_s}}{\partial (p_\xi)_s} \right)_\delta \left\{ \left(\frac{\partial p_\xi}{\partial \alpha} \right)_\delta \left[\theta + (\xi_s - \bar{\xi}) \frac{c\dot{\theta}}{U} \right] + \left(\frac{\partial p_s}{\partial \alpha} \right)_\delta \frac{U}{(U_e)_s} \frac{c\dot{\theta}}{U} \right\}\end{aligned}\quad (C.18)$$

$$\begin{aligned}\frac{\partial \Delta^i_{\xi_s}}{\partial \frac{c\dot{\theta}}{U}} &= \Delta^i_{\xi_s \dot{\theta}} = - \left(\frac{\partial \Delta^i_{\xi_s}}{\partial \alpha} \right)_{p_\xi} \left[1.25 (\xi_s - \xi_{AC}) + \bar{\xi} - \xi_{AC} \right] \\ &+ \left(\frac{\partial \Delta^i_{\xi_s}}{\partial (p_\xi)_s} \right)_\delta \left[\left(\frac{\partial (p_\xi)_s}{\partial \alpha} \right)_\delta (\xi_s - \bar{\xi}) + \left(\frac{\partial p_s}{\partial \alpha} \right)_\delta \frac{U}{(U_e)_s} \right]\end{aligned}\quad (C.19)$$

$$\Delta^i C_{N\dot{\theta}} = \Delta C_{p_s} \cdot \Delta^i \xi_{s\dot{\theta}} \quad (C.20)$$

When the adverse pressure gradient at the intended shock position exceeds a critical value, the shock jumps all the way to the cone shoulder. The critical value can be expressed in the following form:

In the static case,

$$\left(\frac{dp_s}{d\xi} \right)_{\text{crit}} = p_{\xi_s}(\alpha_{\text{crit}}) \quad (C.21)$$

In the unsteady case, a higher angle of attack, $\alpha_{\text{crit}} + \Delta_p \alpha_{\text{crit}}$, can be reached due to the accelerated flow effect on the pressure gradient; and

$$\begin{aligned} \left(\frac{dp_s}{d\xi} \right)_{\text{crit}} &= p_{\xi_s}(\alpha_{\text{crit}}) + \left(\frac{\partial(p_{\xi_s})}{\partial\alpha} \right)_{\delta} \Delta_p \alpha_{\text{crit}} \\ &+ \left(\frac{\partial(p_{\xi_s})}{\partial\alpha} \right)_{\delta} (\xi_s - \bar{\xi}) \frac{c\dot{\theta}}{U} + \left(\frac{\partial p_s}{\partial\alpha} \right)_{\delta} \frac{c\dot{\theta}}{(U_e)_s} \end{aligned} \quad (C.22)$$

That is,

$$\Delta_p \alpha_{\text{crit}} = \left[\bar{\xi} - \xi_s - \frac{\left(\frac{\partial p_s}{\partial\alpha} \right)_{\delta}}{\left(\frac{\partial(p_{\xi_s})}{\partial\alpha} \right)_{\delta}} \frac{U}{(U_e)_s} \right] \frac{c\dot{\theta}}{U} \quad (C.23)$$

For the blunter nose shapes, this comprises all the delay, as the δ -effect goes to zero near the nose (Fig. C-8). For more slender nose shapes, however, the boundary layer build-up also has an effect. If the δ -effect was solely responsible for the jump to

complete separation, the delay for the pitching body would be determined simply by the time lag Δt in the boundary layer build-up. That is,

$$(\delta_s)_{\text{crit}} = \delta(\alpha_0) + \frac{d\delta}{d\alpha} \cdot \tilde{\alpha}_{AC}(t - \Delta t) \quad (\text{C. 24})$$

where

$$\Delta t = 1.25(\xi_s - \xi_{AC}) c/U$$

That is,

$$\Delta_{\delta} \alpha_{\text{crit}} = \left[1.25(\xi_s - \xi_{AC}) + \bar{\xi} - \xi_{AC} \right] \frac{c \dot{\theta}}{U} \quad (\text{C. 25})$$

Using the shock motion sensitivity to δ - and p_{ξ} -changes (Fig. C-8) as a guide, the total delay $\Delta \alpha_{\text{crit}}$ may be expressed as follows:

$$\Delta \alpha_{\text{crit}} = \frac{\left(\frac{\partial \Delta i_{\xi_s}}{\partial \alpha} \right)_{\delta}}{\frac{d \Delta i_{\xi_s}}{d \alpha}} \Delta p_{\alpha_{\text{crit}}} + \frac{\left(\frac{\partial \Delta i_{\xi_s}}{\partial \alpha} \right)_{p_{\xi}}}{\frac{d \Delta i_{\xi_s}}{d \alpha}} \Delta_{\delta} \alpha_{\text{crit}} \quad (\text{C. 26})$$

and, through Eqs. (C. 23) and (C. 25),

$$\Delta\alpha_{\text{crit}} = \left\{ 1.25 (\xi_s - \xi_{AC}) \frac{\left(\frac{\partial \Delta^i \xi_s}{\partial \alpha} \right) p_\xi}{\frac{d\Delta^i \xi_s}{d\alpha}} \right. \\ \left. + \left[\bar{\xi} - \xi_s - \frac{\left(\frac{\partial p_s}{\partial \alpha} \right) \delta}{\left(\frac{\partial (p_\xi)_s}{\partial \alpha} \right) \delta} \frac{U}{(U_e)_s} \frac{\left(\frac{\partial \Delta^i \xi_s}{\partial \alpha} \right) \delta}{\frac{d\Delta^i \xi_s}{d\alpha}} \right] \frac{c\dot{\theta}}{U} \right. \quad (C.27)$$

C.5 VEHICLE DYNAMICS

The equation of motion of the elastic vehicle describing single degree-of-freedom bending oscillations can be written as follows, using standard notations:

$$\tilde{m} \left[\ddot{q}(t) + 2\zeta\omega\dot{q}(t) + \omega^2 q(t) \right] = F(t) \quad (C.28)$$

The generalized force $F(t)$ is given by the virtual work done by the aerodynamic forces on the vehicle.

$$F(t) = \int \frac{dN}{dx} \varphi(x) dx + \int \frac{dM_A}{dx} \varphi'(x) dx \quad (C.29)$$

Only the force $F_s(t)$, induced by the terminal shock-boundary layer interaction, needs special consideration.

$$F_s(t) = \frac{\rho U^2}{2} S \Delta^i C_N(t) \varphi(x_s)$$

$$\Delta^i C_N(t) = \Delta C_{p_s} \Delta^i \xi_s(t) \quad (C.30)$$

$\Delta^i \xi_s(t)$ is given by Eq. (C.15) where for the elastic body (See Fig. C-13, Sketch 2), the following holds:

$$\left. \begin{aligned} \tilde{\alpha} &= \theta + \frac{\dot{z}}{U} \\ z &= -\varphi(x)q(t) \\ \theta &= \varphi'(x)q(t) \end{aligned} \right\} \quad (C.31)$$

Thus, Eqs. (C.15) through (C.17) transform to

$$\Delta^i \xi_s(t) = \left(\frac{\partial \Delta^i \xi_s}{\partial \alpha} \right)_{p_\xi} \left\{ \varphi'(x_{AC})q(t) \right.$$

$$- \left[1.25(\xi_s - \xi_{AC})c\varphi'(x_{AC}) + \varphi(x_{AC}) \right] \frac{\dot{q}(t)}{U} \left. \right\}$$

$$+ \left(\frac{\partial \Delta^i \xi_s}{\partial (p_\xi)_s} \right)_\delta \left\{ \left(\frac{\partial (p_\xi)_s}{\partial \alpha} \right)_\delta \varphi'(x_s)q(t) \right.$$

$$- \left[\left(\frac{\partial (p_\xi)_s}{\partial \alpha} \right)_\delta \varphi(x_s) - \left(\frac{\partial p_s}{\partial \alpha} \right)_\delta \frac{U}{U_e} c\varphi'(x_s) \right] \frac{\dot{q}(t)}{U} \left. \right\} \quad (C.32)$$

Substituting

$$x_1 = c\xi = x_0 - x$$

the corresponding generalized force becomes:

$$F_s(t) = \frac{\rho U^2}{2} S \Delta C_{p_s} \Delta^i \xi_s(t) \varphi(\xi_s) \quad (C. 33)$$

or

$$F_s(t) = \frac{\rho U^2}{2} S \left[K_s q(t) + D_s \frac{\dot{q}(t)}{U} \right]$$

$$K_s = \frac{\varphi(\xi_s)}{c} \Delta C_{p_s} \left\{ \left(\frac{\partial \Delta^i \xi_s}{\partial \alpha} \right)_{p_\xi} \frac{\partial \varphi}{\partial \xi} (\xi_{AC}) + \left(\frac{\partial \Delta^i \xi_s}{\partial \alpha} \right)_\delta \frac{\partial \varphi}{\partial \xi} (\xi_s) \right\}$$

$$D_s = -\varphi(\xi_s) \Delta C_{p_s} \left\{ \left(\frac{\partial \Delta^i \xi_s}{\partial \alpha} \right)_{p_\xi} \left[\varphi(\xi_{AC}) + 1.25 (\xi_{AC} - \xi_s) \frac{\partial \varphi}{\partial \xi} (\xi_{AC}) \right] \right\}$$

$$+ \left(\frac{\partial \Delta^i \xi_s}{\partial (p_\xi)_s} \right)_\delta \left\{ \left(\frac{\partial (p_\xi)_s}{\partial \alpha} \right)_\delta \varphi(\xi_s) + \left(\frac{\partial p_s}{\partial \alpha} \right)_\delta \frac{U}{U_e} \frac{\partial \varphi}{\partial \xi} (\xi_s) \right\} \quad (C. 34)$$

$$U/U_e = (M_\infty/M_s) \left(1 + \frac{\gamma-1}{2} M_s^2 \right)^{1/2} \left(1 + \frac{\gamma-1}{2} M_\infty^2 \right)^{-1/2}$$

For attached flow the generalized force may be expressed similarly as

$$F_a(t) = \frac{\rho U^2}{2} S \left[K_a q(t) + D_a \frac{\dot{q}(t)}{U} \right] \quad (C. 35)$$

Combining Eqs. (C. 28), (C. 34), and (C. 35) gives:

$$\ddot{q}(t) + 2\omega \left[\zeta - \frac{B}{2\omega U} (D_s + D_a) \right] \dot{q}(t) + \omega^2 \left[1 - \frac{B}{\omega^2} (K_s + K_a) \right] q(t) = f(t)$$

$$B = \frac{\rho U^2}{2} S/\tilde{m} \quad (C. 36)$$

$f(t) = F_b(t)/\tilde{m}$; Forcing function, e. g. buffeting forces

C. 5. 1 Aerodynamic Damping

One requirement for stability is that the amplitude $|q(t)|$ is bounded; i. e. , does not increase with time beyond all bounds. This implies that the coefficient for $\dot{q}(t)$ in Eq. (C. 36) cannot be negative, i. e. ,

$$\zeta - (B/2\omega U) (D_s + D_a) \geq 0 \quad (C. 37)$$

In presence of a forcing function, $f(t)$, the requirement of limiting the amplitude to a certain value gives

$$\zeta - (B/2\omega U) (D_s + D_a) \geq \zeta_{\min} \quad (C. 38)$$

D_s and D_a are the aerodynamic damping contributions from separated and attached flow regions, respectively. They correspond to the damping derivative for a rigid body, a negative value indicating damped oscillations. The multiplication factor $-B/2\omega U$ brings the aerodynamic damping in the same form as the structural damping. Thus, the damping contributions from the separated and attached flow regions have the following ratios to the critical damping:

$$\left. \begin{aligned} \zeta_s &= -(\rho US/4\omega\tilde{m}) D_s \\ \zeta_a &= -(\rho US/4\omega\tilde{m}) D_a \end{aligned} \right\} \quad (C. 39)$$

Using the 20° cone cylinder data (Figs. C-8 through C-10), the SA-203 vehicle would experience the undamping effect (ξ_s) shown in Fig. C-14, when oscillating in its second bending mode.

C.5.2 Nonlinear Damping

When accounting for the dynamic effects of the jumping between retarded shock-induced separation and complete separation, special techniques are needed. The damping as defined by Eqs. (C.34) through (C.39) is valid only for infinitesimal amplitudes, or for finite amplitudes only for linear aerodynamic characteristics. For nonlinear characteristics a measure of the damping at finite amplitudes can be defined as follows (Ref. 26).

Let \bar{D} be the constant describing the energy dissipation (E) during one cycle of oscillation (period T).

$$\begin{aligned}
 E &= \int_{t_0}^{t_0+T} F_s(t) dq = \int_{t_0}^{t_0+T} F_s(t) \dot{q} dt \\
 &= \frac{\rho U^2}{2} S \int_{t_0}^{t_0+T} C_N(t) \varphi(\xi_s) \dot{q} dt \\
 &= \frac{\rho U^2}{2} S \int_{t_0}^{t_0+T} \bar{D} \frac{\dot{q}}{U} \dot{q} dt
 \end{aligned} \tag{C.40}$$

That is

$$\bar{D} = \frac{\int_{t_0}^{t_0+T} C_N(t) \varphi(\xi_g) \dot{q} dt}{\int_{t_0}^{t_0+T} (\dot{q})^2 dt} \quad (C.41)$$

For harmonic oscillations, $q = |q| \sin \omega t$, where $|q| = \Delta q$ and ω are assumed constant during one cycle of oscillation, $\bar{D} = D(\xi)$ can be expressed as follows:

$$\begin{aligned} \bar{D} &= \frac{\int_{t_0}^{t_0+T} C_N(t) \varphi(\xi) \Delta q \cos \omega t \omega dt}{\frac{\omega \Delta q}{U} \int_{t_0}^{t_0+T} \Delta q \cos^2 \omega t \omega dt} \\ &= \frac{\int_{\psi_0}^{\psi_0+2\pi} C_N(\psi) \varphi(\xi) \cos \psi d\psi}{\frac{\omega \Delta q}{U} \int_{\psi_0}^{\psi_0+2\pi} \cos^2 \psi d\psi} \end{aligned} \quad (C.42)$$

i. e. , the effective damping \bar{D} is

$$\bar{D} = \frac{\varphi(\xi)}{\pi \frac{\omega \Delta q}{U}} \int_{\psi_0}^{\psi_0+2\pi} C_N(\psi) \cos \psi d\psi \quad (C.43)$$

where $\psi = \omega t$, $2\pi = \psi T$.

The effective aerodynamic spring \bar{K} can be defined similarly as follows:

$$\int_0^{\Delta q} C_N(q) \varphi(\xi_s) q dq = \int_0^{\Delta q} \bar{K} q dq$$

i. e. ,

$$\bar{K} = \frac{2\varphi(\xi_s)}{(\Delta q)^2} \int_0^{\Delta q} C_N(q) q dq \quad (C.44)$$

The nonlinear characteristics associated with the jump to complete separation can be represented as follows: (Fig. C-15, Sketch 3).

Both C_{N_1} and C_{N_2} can be written:*

$$C_N = \begin{cases} C_{N_{\alpha_o}} \alpha & ; |\alpha| \leq \alpha_{crit} \\ C_{N_{\alpha_L}} \alpha + \left(C_{N_{\alpha_o}} - C_{N_{\alpha_L}} \right) \alpha_{crit} + \frac{\alpha}{|\alpha|} \Delta C_{N_d} & ; |\alpha| > \alpha_{crit} \end{cases} \quad (C.45)$$

or, with

$$C_N = C_{N_\alpha} \left[\alpha_o + \varphi'(\xi) q \right] + C_{N_q} \frac{\dot{q}}{U} + C_{N_o} \quad (C.46)$$

*Only characteristics close to α_{crit} are of interest, allowing use of linear characteristics with a discrete step. No static hysteresis effects are included here (see Ref. 26 for hysteresis effects) as the data do not indicate such a possibility (e. g. , see Fig. C-12).

$$C_N = \begin{cases} C_{N_{\alpha_0}} [\alpha_0 + \varphi'(\xi)] + C_{N_{\dot{q}_0}} \frac{\dot{q}}{U} & ; |\tilde{\alpha}_i| \leq \alpha_{crit} \\ C_{N_{\alpha_L}} [\alpha_0 + \varphi'(\xi)] + C_{N_{\dot{q}_L}} \frac{\dot{q}}{U} + [C_{N_{\alpha_0}} - C_{N_{\alpha_L}}] \alpha_{crit} + \frac{\tilde{\alpha}_i}{|\tilde{\alpha}_i|} \Delta C_{N_d} & ; |\tilde{\alpha}_i| > \alpha_{crit} \end{cases}$$

(C. 47)

The step ΔC_{N_d} (negative for C_{N_1} and positive for C_{N_2}) occurs when the separation moves to the cone-cylinder shoulder. For the δ -effects, this event is guided by the crossflow at ξ_{AC} . For the p_ξ -effects, it is guided by the crossflow angle at the shock, ξ_s . The δ - and p_ξ -effects can be separated as indicated earlier [Eq. (C. 26)]. For both effects, the guiding angle $\tilde{\alpha}_i$ can be written*

$$\tilde{\alpha}_i(t) = \alpha_0 + \varphi'(\xi_s) q(t) - \Delta\alpha_{crit} \quad (C. 48)$$

where for the δ - and P_ξ -effects, respectively,

$$\Delta_\delta \alpha_{crit} = \varphi(\xi_{AC}) \left[1 + 1.25 (\xi_s - \xi_{AC}) \frac{c\varphi'(\xi_{AC})}{\varphi(\xi_{AC})} \right] \frac{\dot{q}}{U} \quad (C. 49)$$

$$\Delta_{p_\xi} \alpha_{crit} = \varphi(\xi_s) \left[1 - \frac{\left(\frac{\partial p_s}{\partial \alpha} \right)_\delta}{\left(\frac{\partial (p_\xi)_s}{\partial \alpha} \right)_\delta} \frac{U}{(U_e)_s} \frac{c\varphi'(\xi_s)}{\varphi(\xi_s)} \right] \frac{\dot{q}}{U} \quad (C. 50)$$

That is, $\Delta\alpha_{crit}$ can be written

$$\Delta\alpha_{crit} = a \frac{\dot{q}}{U} \quad (C. 51)$$

*Any local delay in realizing the force change after $\alpha_{crit} + \Delta\alpha_{crit}$ at ξ_s has been reached is neglected.

For harmonic oscillations, $q = \Delta q \sin \omega t$

$$\begin{aligned}\tilde{\alpha}_i &= \alpha_o + \varphi'(\xi_s) \Delta q \sin \omega t - a \frac{\omega \Delta q}{U} \cos \omega t \\ &= \alpha_o + \varphi'(\xi_s) \Delta q \left[\sin \omega t - \frac{a}{c\varphi'(\xi_s)} \frac{c\omega}{U} \cos \omega t \right]\end{aligned}$$

i. e. ,

$$\left. \begin{aligned}\tilde{\alpha}_i &= \alpha_o + \frac{\Delta q \varphi'(\xi_s)}{\cos \beta} \sin (\psi - \beta) \\ \tan \beta &= b = \frac{a}{c\varphi'(\xi_s)} \cdot \frac{\omega c}{U} \\ \psi &= \omega t\end{aligned}\right\} \quad (C. 52)$$

The variation of $\tilde{\alpha}_i$ during one cycle of oscillation is described in Fig. C-15, sketch 4, and Eq. (C. 53) below:

$$\left. \begin{aligned}\sin \psi_1 &= \frac{\alpha_o - \alpha_{\text{crit}}}{\Delta q \varphi'(\xi_s)} \cos \beta \\ \sin \psi_2 &= \frac{\alpha_o + \alpha_{\text{crit}}}{\Delta q \varphi'(\xi_s)} \cos \beta\end{aligned}\right\} \quad (C. 53)$$

\bar{D}_s is then given by Eqs. (C. 43), (C. 47), and (C. 53):

$$\bar{D}_s = \frac{\varphi(\xi)}{\pi \frac{\Delta q}{c} \frac{\omega c}{U}} \left\{ \int_{\beta-\psi_2}^{\beta-\psi_1} C_{N_{\alpha_0}}(\psi) \cos \psi d\psi + \int_{\beta-\psi_1}^{\pi+\beta+\psi_1} C_{N_{\alpha_L}}(\psi) \cos \psi d\psi \right. \\ \left. + \int_{\pi+\beta+\psi_1}^{\pi+\beta+\psi_2} C_{N_{\alpha_0}}(\psi) \cos \psi d\psi + \int_{\pi+\beta+\psi_2}^{2\pi+\beta-\psi_2} C_{N_{\alpha_L}}(\psi) \cos \psi d\psi \right\}$$

$$C_{N_{\alpha_0}}(\psi) = C_{N_{\alpha_0}} \left[\alpha_0 + \varphi'(\xi_s) \Delta q \sin \psi \right] + \frac{\omega c}{U} \frac{\Delta q}{c} C_{N_{\dot{q}_0}} \cos \psi$$

$$C_{N_{\alpha_L}}(\psi) = C_{N_{\alpha_L}} \left[\alpha_0 + \varphi'(\xi_s) \Delta q \sin \psi \right] + \frac{\omega c}{U} \frac{\Delta q}{c} C_{N_{\dot{q}_L}} \cos \psi$$

$$+ \left(C_{N_{\alpha_0}} - C_{N_{\alpha_L}} \right) \alpha_{\text{crit}} + \frac{\tilde{\alpha}_i}{|\tilde{\alpha}_i|} \Delta C_{N_d} \quad (\text{C. 54})$$

The integration gives the following result:

$$\frac{\bar{D}_s}{\varphi(\xi)} = C_{N_{\dot{q}_L}} - \frac{1}{\pi} \frac{\Delta C_{N_d}}{\frac{\Delta q}{c}} \frac{1}{\frac{\omega c}{U}} \frac{2b}{1+b^2} \\ \cdot \left[\sqrt{1+b^2 - \left(\frac{\alpha_0 + \alpha_{\text{crit}}}{\Delta q \varphi'(\xi_s)} \right)^2} + \sqrt{1+b^2 - \left(\frac{\alpha_0 - \alpha_{\text{crit}}}{\Delta q \varphi'(\xi_s)} \right)^2} \right] \\ + \frac{C_{N_{\dot{q}_0}} - C_{N_{\dot{q}_L}}}{\pi} \left\{ \arcsin \frac{\alpha_0 + \alpha_{\text{crit}}}{\Delta q \varphi'(\xi_s) \sqrt{1+b^2}} - \arcsin \frac{\alpha_0 - \alpha_{\text{crit}}}{\Delta q \varphi'(\xi_s) \sqrt{1+b^2}} \right\}$$

$$\begin{aligned}
& + \frac{1 - b^2}{(1 + b^2)^2} \left[\frac{\alpha_o + \alpha_{crit}}{\Delta q \varphi'(\xi_s)} \sqrt{1 + b^2 - \left(\frac{\alpha_o + \alpha_{crit}}{\Delta q \varphi'(\xi_s)} \right)^2} \right. \\
& \quad \left. - \frac{\alpha_o - \alpha_{crit}}{\Delta q \varphi'(\xi_s)} \sqrt{1 - b^2 - \left(\frac{\alpha_o - \alpha_{crit}}{\Delta q \varphi'(\xi_s)} \right)^2} \right] \\
- & \frac{2 \left(C_{N_{\alpha_o}} - C_{N_{\alpha_L}} \right)}{\pi} \frac{1}{\frac{\omega c}{U}} \frac{b^3}{(1 + b^2)^2} \cdot \left[\frac{\alpha_o + \alpha_{crit}}{\Delta q \varphi'(\xi_s)} \sqrt{1 + b^2 - \left(\frac{\alpha_o - \alpha_{crit}}{\Delta q \varphi'(\xi_s)} \right)^2} \right. \\
& \quad \left. - \frac{\alpha_o - \alpha_{crit}}{\Delta q \varphi'(\xi_s)} \sqrt{1 + b^2 - \left(\frac{\alpha_o - \alpha_{crit}}{\Delta q \varphi'(\xi_s)} \right)^2} \right] \quad (C.55)
\end{aligned}$$

In the quasi-steady analysis, it is implicitly assumed that $(\omega c/U)^2 \ll 1$ which, in general, also makes $b^2 \ll 1$. For the elastic vehicle, the amplitudes will rarely be large enough to catch both jumps, i. e. ,

$$\left| \frac{\alpha_o + \alpha_{crit}}{\Delta q \varphi'(\xi_s)} \right| \text{ or } \left| \frac{\alpha_o - \alpha_{crit}}{\Delta q \varphi'(\xi_s)} \right|$$

is larger than unity and either $\psi_2 = \pi/2$ or $\psi_1 = \pi/2$. Assuming $\alpha_o > 0$, Eq. (C.55) becomes with the above assumptions:

$$\begin{aligned}
\frac{\bar{D}_s}{\varphi(\xi)} = & \frac{C_{N_{\dot{q}_o}} + C_{N_{\dot{q}_L}}}{2} - \frac{2}{\pi} \frac{\Delta C_{N_d}}{\Delta q} \frac{b}{\frac{\omega c}{U}} \sqrt{1 - \left(\frac{\alpha_o - \alpha_{crit}}{\Delta q \varphi'(\xi_s)} \right)^2} \\
& - \frac{C_{N_{\dot{q}_o}} - C_{N_{\dot{q}_L}}}{\pi} \left\{ \arcsin \frac{\alpha_o - \alpha_{crit}}{\Delta q \varphi'(\xi_s)} + \frac{\alpha_o - \alpha_{crit}}{\Delta q \varphi'(\xi_s)} \sqrt{1 - \left(\frac{\alpha_o - \alpha_{crit}}{\Delta q \varphi'(\xi_s)} \right)^2} \right\}
\end{aligned}$$

where,

$$\begin{aligned}
 & b/\frac{\omega c}{U} = a/c \varphi'(\xi_s) \\
 a = \varphi(\xi_s) \cdot & \left\{ \begin{array}{l} \frac{\varphi(\xi_{AC})}{\varphi(\xi_s)} \left[1 + 1.25 (\xi_s - \xi_{AC}) \frac{c \varphi'(\xi_{AC})}{\varphi(\xi_{AC})} \right] : \delta\text{-effect} \\ \left[1 - \frac{(\partial p_s / \partial \alpha)}{(\partial (p\xi)_s / \partial \alpha)} \frac{\delta}{\delta} \frac{U}{(U_e)_s} \frac{c \varphi'(\xi_s)}{\varphi(\xi_s)} \right] : P_\xi\text{-effect} \end{array} \right. \quad (C. 56)
 \end{aligned}$$

When $\alpha_o = \alpha_{crit}$, i. e., when the jump effects are maximum,

$$(\bar{D}_s)_{\max} = \varphi(\xi) \left\{ \frac{C_{N\dot{q}_o} + C_{N\dot{q}_L}}{2} - \frac{2a}{\pi} \frac{\Delta C_{N_d}}{\Delta q \varphi'(\xi_s)} \right\} \quad (C. 57)$$

Returning to Fig. C-13, Sketch 2, $\Delta q \varphi'(\xi_s)$ can be expressed as

$$\Delta q \varphi'(\xi_s) = \frac{\varphi'(\xi_s)}{\varphi'(\xi_N)} \Delta q \varphi'(\xi_N) \quad (C. 58)$$

i. e.,

$$\Delta q \varphi'(\xi_s) = \frac{\varphi'(\xi_s)}{\varphi'(\xi_N)} \Delta \theta_N$$

$\Delta\theta_N$ is the angular amplitude at the nose. Equation (C.57) thus becomes:

$$\begin{aligned}
 (\bar{D}_s)_{\max} &= \varphi(\xi) \frac{C_{N\dot{q}_0}}{2} + \varphi(\xi) \frac{C_{N\dot{q}_L}}{2} + \Delta(\bar{D}_s)_{\max} \\
 \Delta(\bar{D}_s)_{\max} &= -\frac{2}{\pi} \frac{\Delta C_{N_d} \frac{\partial \varphi}{\partial \xi}(\xi_N)}{\Delta\theta_N \frac{\partial \varphi}{\partial \xi}(\xi_s)} \varphi(\xi) \\
 &\quad \left\{ \begin{array}{l} \varphi(\xi_{AC}) + 1.25 (\xi_{AC} - \xi_s) \frac{\partial \varphi}{\partial \xi}(\xi_{AC}) ; \delta\text{-effect} \\ \varphi(\xi_s) + \frac{\left(\frac{\partial p_s}{\partial \alpha}\right)_{\delta}}{\left(\frac{\partial(p_{\xi_s})}{\partial \alpha}\right)_{\delta}} \frac{\partial \varphi}{\partial \xi}(\xi_s) \frac{U}{(U_e)_s} ; p_{\xi}\text{-effect} \end{array} \right. \quad (C.59)
 \end{aligned}$$

$\varphi(\xi) C_{N\dot{q}_0}$ and $\varphi(\xi) C_{N\dot{q}_L}$ are given by Eq. (C.34) as D_s for $\alpha < \alpha_{crit}$ and $\alpha > \alpha_{crit}$, respectively. At $\alpha > \alpha_{crit}$, the leeward side is completely separated (imbedded in "dead air"), and its contribution to the damping is negligible compared to the windward side attached flow contribution. That is,

$$\left(\varphi(\xi) \frac{C_{N\dot{q}_L}}{2} \right)_1 + \left(\varphi(\xi) \frac{C_{N\dot{q}_L}}{2} \right)_2 = \frac{1}{2} (D_s)_{\alpha > \alpha_{crit}} \approx 0 \quad (C.60)$$

The contribution for $\alpha < \alpha_{\text{crit}}$ is

$$\left(\varphi(\xi) \frac{C_{N, \dot{q}_0}}{2} \right)_1 + \left(\varphi(\xi) \frac{C_{N, \dot{q}_0}}{2} \right)_2 = \frac{1}{2} (D_s)_{\alpha < \alpha_{\text{crit}}} \quad (\text{C. 61})$$

where $(D_s)_{\alpha < \alpha_{\text{crit}}}$ is given by Eq. (C. 34).

Thus, the total separation induced contribution to the damping can be expressed as follows when using Eq. (C. 26) to relate δ - and p_ξ -effects:

$$\begin{aligned} (\bar{D}_s)_{\text{max}} &= \frac{1}{2} (D_s)_{\alpha < \alpha_{\text{crit}}} + \Delta_1 (\bar{D}_s)_{\text{max}} + \Delta_2 (\bar{D}_s)_{\text{max}} \\ (D_s)_{\alpha < \alpha_{\text{crit}}} &= -\varphi(\xi_s) \Delta C_{p_s} \left\{ \left(\frac{\partial \Delta^i \xi_s}{\partial \alpha} \right)_{p_\xi} \left[\varphi(\xi_{AC}) + 1.25 (\xi_{AC} - \xi_s) \frac{\partial \varphi}{\partial \xi} (\xi_{AC}) \right] \right. \\ &\quad \left. + \left(\frac{\partial \Delta^i \xi_s}{\partial \alpha} \right)_\delta \left[\left(\frac{\partial (p_\xi)_s}{\partial \alpha} \right)_\delta \varphi(\xi_s) + \left(\frac{\partial p_s}{\partial \alpha} \right)_\delta \frac{\partial \varphi}{\partial \xi} (\xi_s) \left(\frac{U}{U_e} \right)_s \right] \right\} \end{aligned}$$

$$\Delta_n(\bar{D}_s)_{\max} = -\frac{2}{\pi} \frac{\Delta C_{Nd}}{\Delta \theta_N} \frac{\frac{\partial \varphi}{\partial \xi}(\xi_N)}{\frac{\partial \varphi}{\partial \xi}(\xi_s)} \varphi(\xi_s) \cdot \varphi(\xi_n)^*$$

$$\cdot \left\{ \frac{\left(\frac{\partial \Delta^i \xi_s}{\partial \alpha} \right) p_\xi}{\frac{d \Delta^i \xi_s}{d \alpha}} \frac{\varphi(\xi_{AC})}{\varphi(\xi_s)} \left[1 + 1.25 (\xi_{AC} - \xi_s) \frac{\frac{\partial \varphi}{\partial \xi}(\xi_{AC})}{\varphi(\xi_{AC})} \right] \right.$$

$$\left. + \frac{\left(\frac{\partial \Delta^i \xi_s}{\partial \alpha} \right) \delta}{\frac{d \Delta^i \xi_s}{d \alpha}} \left[1 + \frac{\left(\frac{\partial p_s}{\partial \alpha} \right) \delta}{\left(\frac{\partial (p_\xi)_s}{\partial \alpha} \right) \delta} \frac{\frac{\partial \varphi}{\partial \xi}(\xi_s)}{\varphi(\xi_s)} \frac{M_\infty}{M_s} \left[\frac{1 + \frac{\gamma-1}{2} M_s^2}{1 + \frac{\gamma-1}{2} M_\infty^2} \right]^{1/2} \right] \right\}$$

(C. 62)

$(D_s)_{\alpha < \alpha_{crit}}$ is positive and contributes undamping [$\xi_s \sim -D_s$, Eq. (C. 39)] as was illustrated in Fig. C-14. $\Delta_1(D_s)_{\max}$ is determined in sign entirely by $\Delta_1 C_{Nd}$, as the nodal point is well downstream of ξ_s . Hence, as $\Delta_1 C_{Nd} < 0$ (Figs. C-2 and C-15, Sketch 5), $\Delta_1(D_s)_{\max}$ is positive, i. e., indicative of undamping. The magnitude of the undamping ratio to critical damping [Eq. (C. 39)] is inversely proportional to the nose amplitude $\Delta \theta_N$. When the nodal point is downstream of ξ_2 , the sign of $\Delta_2(D_s)_{\max}$ is also determined only by $\Delta_2 C_{Nd}$, and as $\Delta_2 C_{Nd} > 0$ (Fig. C-2 and Fig. C-15, Sketch 3) the contribution $\Delta_2(\bar{D}_s)_{\max}$ is then damping. However, when the nodal point moves upstream of ξ_2 , also $\Delta_2(\bar{D}_s)_{\max}$ may contribute undamping.

*n = 1 or 2.

The separation-induced elastic body damping in percent of critical $(\xi_s)_{\alpha < \alpha_{crit}}$ and $(\Delta\xi_s)_{min}$, is obtained by applying Eq. (C.39) to Eqs. (C.34) and (C.62), respectively. The damping derivative $(C_{m\dot{\theta}_s})_{\alpha < \alpha_{crit}}$ and $(\Delta C_{m\dot{\theta}})_{max}$ for rigid body oscillations around $\xi_{CG} = \bar{\xi}$ is obtained by using the rigid body mode, i. e.,

$$\left. \begin{aligned} \varphi(\xi) &= \bar{\xi} - \xi \\ q(t) &= \theta(t) \cdot c \end{aligned} \right\} \quad (C.63)$$

where $\theta(t)$ is the body attitude perturbation from the trim angle of attack α_o

$$\left[\alpha_o = \alpha_{crit} \text{ for } (\Delta C_{m\dot{\theta}})_{max} \right].$$

C.6 DISCUSSION

The effect of the shock-boundary layer interaction on the aeroelastic stability at $\alpha < \alpha_{crit}$ is very modest, causing slightly decreased damping (Fig. C-14). The effect at $\alpha = \alpha_{crit}$ is, however, appreciable (Fig. C-16) and may cause concern especially in regard to aeroelastic stability, where the allowable nose amplitude $\Delta\theta_N$ is small. Figure C-16 shows $(\Delta\xi_s)_{min}$ for a Saturn booster in its second bending mode. The actual payload is the $25^\circ - 12.5^\circ$ biconic nose shown. Using 20° cone data (Refs. 16, 17) the $(\Delta\xi_s)_{min}$ due to accelerated flow effects alone would be as shown. This would represent the total effects at $\alpha_{crit} < 0$, where the boundary layer buildup, the δ -effect, is negligible. The loading caused by $\Delta\theta_N$ corresponds roughly to the static loading at an order-of-magnitude higher angle of attack ($\alpha_{stat} \approx 10\Delta\theta_N$). At $\alpha_{crit} > 0$ the δ -effect becomes dominant and greatly aggravates the undamping effect (Fig. C-17). For 0.25 degree nose amplitude the undamping increases from -0.5 percent at $\alpha_{crit} < 0$ to -1.5 percent at $\alpha_{crit} = 4^\circ$. That there are reasons for concern is obvious. 0.5 percent is a rather typical value for the structural damping, and $\Delta\theta_N = 0.25^\circ$ is probably a representative value for the allowable nose amplitude. The effect of mode shape is shown in Fig C-18, where the damping has been normalized

to the same generalized mass (that of the second bending mode, \tilde{m}_2). The first bending mode is less affected than second and third modes. The rigid body mode with its more aft node, the body C.G., would be even less influenced than the first mode.

Experimental verification of this undamping effect is hard to come by. Data obtained at the NASA Langley Research Center on an 8-percent elastic model of the Saturn I booster (Ref. 27) indicate the probable occurrence of this phenomenon (Fig. C-19). The 12.5° Jupiter nose cone by itself would not have experienced any complete separation at reasonable angles of attack. However, the presence of the downstream conical frustum with its adverse effects on the forebody pressure gradient is very likely to cause the sudden complete separation to occur. This would then account for the large drop in damping at $M = 0.9$ for positive angles of attack. A more direct verification of the discussed adverse dynamic effects of the "sudden separation" is provided by dynamic wind tunnel tests of rigid cylinder-flare bodies (Ref. 26). Figure C-20 shows the effects of the jumpwise change of flow pattern. Even at the employed amplitudes of above 4° the effect of catching the jump are drastic. The separation-induced load change on a cylinder-flare body with a hemispherical nose (Fig. C-21) shows great similarity with the slender payload phenomenon (Fig. C-1). The associated undamping effect (Fig. C-22) was largely due to the induced flare load with its additional time lag effect (Ref. 26) (the time delay before the separation affects the flare after it has taken place locally at the nose). The accelerated flow effect was neglected on the cylinder-flare bodies (Ref. 26). However, the accelerated flow effects may well have been non-negligible and could provide a more plausible explanation than the shown 1° static α -hysteresis (Fig. C-20).

It is certain that the "sudden separation" has a greatly undamping effect, and that the effect could be catastrophic on an elastic vehicle (if the separation is caught, that is). If one considers this effect catchable only at discrete α - M combinations, represented by the boundaries shown in Fig. C-12, then the probability of an aeroelastic catastrophe is small indeed. However, in the regions of alternating flow, shown in

Fig. C-12, the random separation occurrence for a fixed model (Refs. 15 and 17), does not preclude the possibility that an oscillating model would drive the separation. It is not unlikely that the alternating flow described by Chevalier and Robertson is nothing but a body flow response to a random disturbance at $\alpha_0 = \alpha_{crit}$, e.g., a tunnel flow disturbance. In that case, the regions shown in Fig. C-12 would represent the aeroelastic danger zones, making the problem a great deal more real.

In view of what has been shown so far, it is understandable that the so-called generalized payload on Saturn IB SA-203, the 25°-12.5° biconic nose shown in Figs. C-14 and C-16, was regarded with suspicion and anxiety. However, careful testing failed to show the occurrence of this disastrous "sudden separation." The shadowgraphs in Fig. C-23 reveal why. The first shoulder or cusp between the 25° cone and the 12.5° conical frustum causes the boundary layer to separate ahead of the conical frustum cylinder shoulder, and the reattaching boundary layer is strong enough to negotiate the cone-cylinder shoulder. This beneficial effect of "preseparation" of the boundary layer has also been observed on blunt nose shapes. Figure C-24 shows two nose shapes with the same Newtonian fore-body drag. The elliptical nose has extensive separation, starting at the nose-cylinder shoulder. The flat-face nose with elliptic shoulder fairing, however, has almost no separation. This is again the effect of "preseparating" the boundary layer at the flat face-elliptic fairing juncture. The long elliptic fairing allows the boundary layer to reattach before the cylindrical section, and the boundary layer is able to negotiate the nose-cylinder juncture without extensive separation.

The pressure distribution over the forebody of the SA-203 vehicle varies with angle of attack as shown in Fig. C-25. The additional feature compared to the cone-cylinder data discussed earlier is the 25° cone -12.5° frustum shoulder. The flow expands to supersonic speeds at this shoulder and then shocks out at a Mach number of roughly 1.4 for $\alpha \geq 0$. That is, the conditions on the 12.5° conical frustum are relatively insensitive to positive angles of attack, indicated by the "bend up" of the $p(\xi) = f(\alpha)$ curves for $\alpha > 0$. This obviously will decrease the "accelerated-flow effect", and if it was insignificant on the cone-cylinder bodies (Fig. C-14), it certainly

will be negligible on the SA-203. That is, the methods derived in Refs. 1 and 2 are sufficient to describe the aeroelastic characteristics of SA-203. Figures C-26 and C-27 illustrate the effect of Mach number on the flow over the forward portion of the cylinder (Saturn IV B stage). The aft movement of the terminal shock with increasing Mach number is very pronounced, as was the case on the cone-cylinder bodies. The distinct difference between the double-cone and simple-cone forebodies lies in the α - effect. Figure C-28 shows that the terminal shock after the biconic payload moves practically all the way up to the shoulder without causing complete flow separation. This is, of course, the beneficial effect of the "preseparation" at the cone-cone shoulder discussed earlier.

C.7 CONCLUSIONS

A conical payload, even with a half-angle of 15° or less, can have two kinds of aero-elastically destabilizing effects at high subsonic speeds. One is a commonly occurring linear, moderately undamping effect caused by the continuous interaction between the terminal shock and the separating boundary layer on the booster just aft of the cone-cylinder juncture. The other is a rarely occurring nonlinear, immensely undamping effect caused by the discontinuous load change effected by a sudden jump forward of the flow separation to the cone-cylinder shoulder.

The so-called generalized payload on vehicle SA-203, i. e., the $25^\circ - 12.5^\circ$ double cone, effectively eliminates the dangerous "sudden separation" and also reduces the "accelerated-flow effect." That is, the generalized payload has indeed general usage and the demonstrated beneficial effects of preseparation should be kept in mind when considering other payload shapes, e. g., hammerhead payloads.

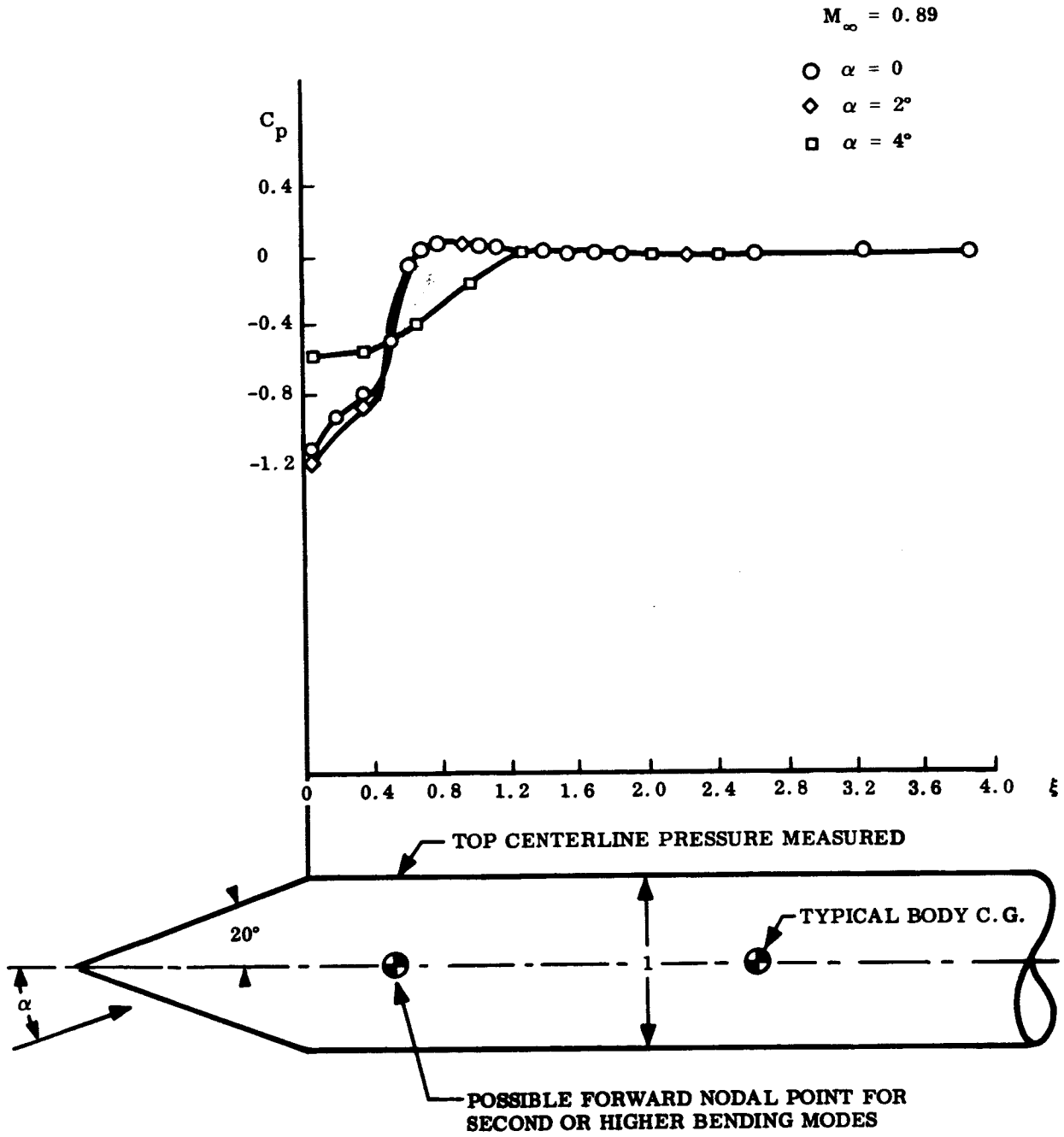


Fig. C-1 Aerodynamic Characteristics at $M_\infty = 0.89$ of a 20° Cone-Cylinder Body With Separated Flow

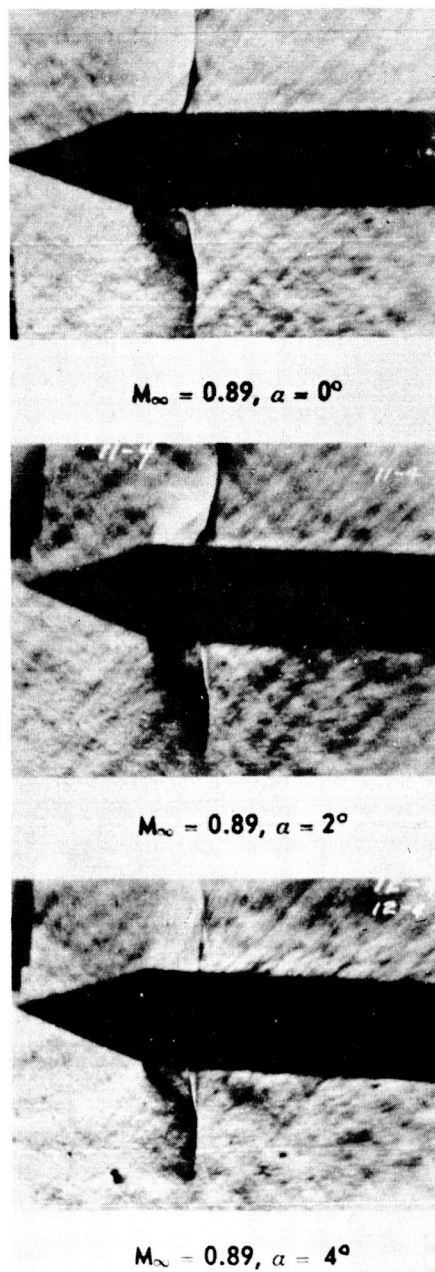


Fig. C-1 Aerodynamic Characteristics at $M_\infty = 0.89$ of a 20° Cone-Cylinder Body With Separated Flow (Cont.)

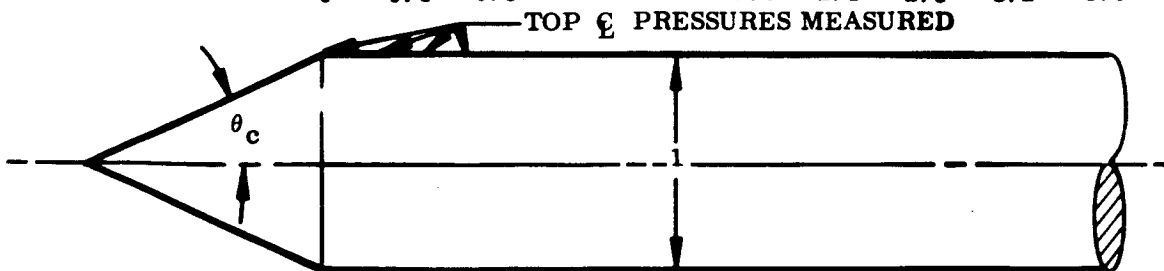
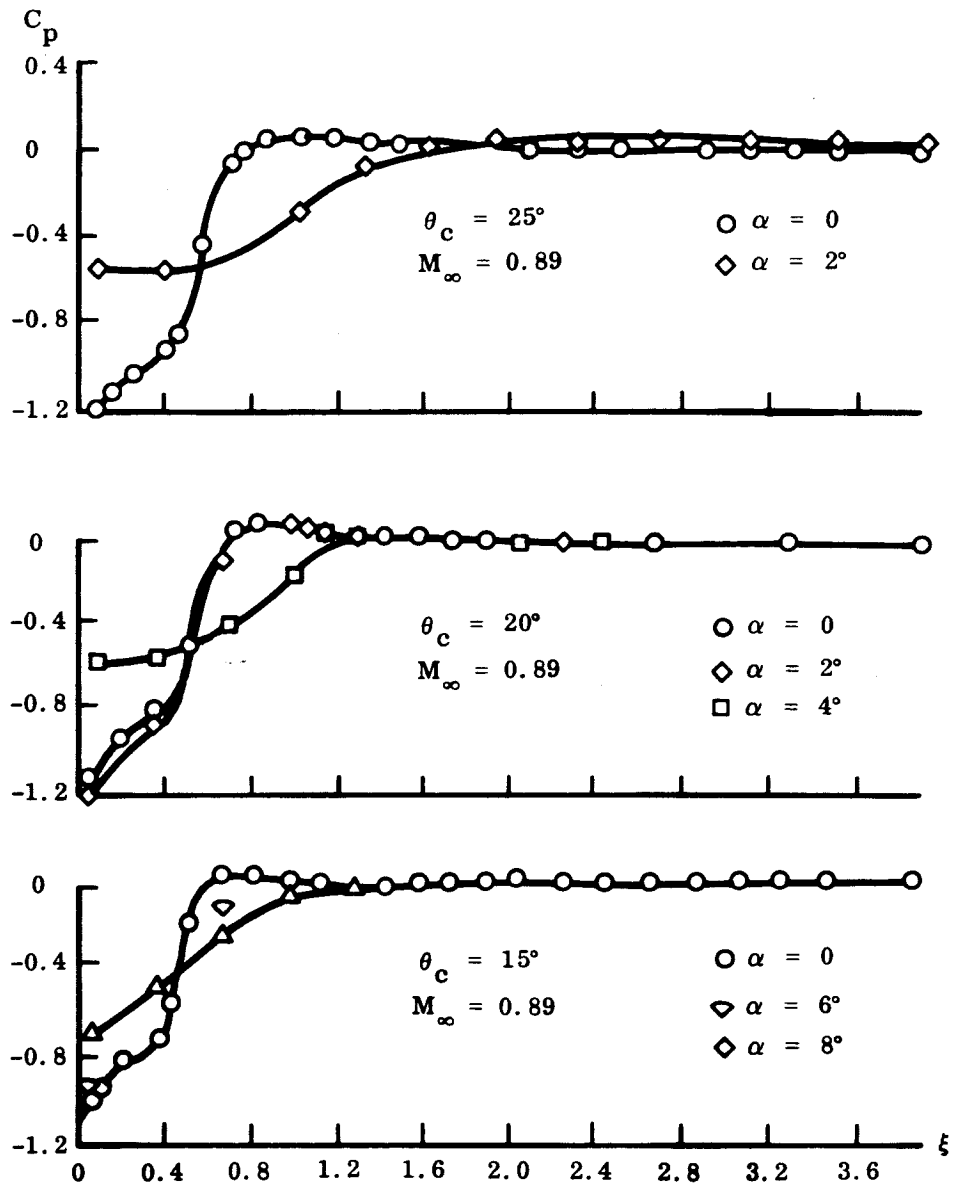


Fig. C-2 Effect of Cone Angle on Occurrence of Complete Flow Separation at $M_\infty = 0.89$

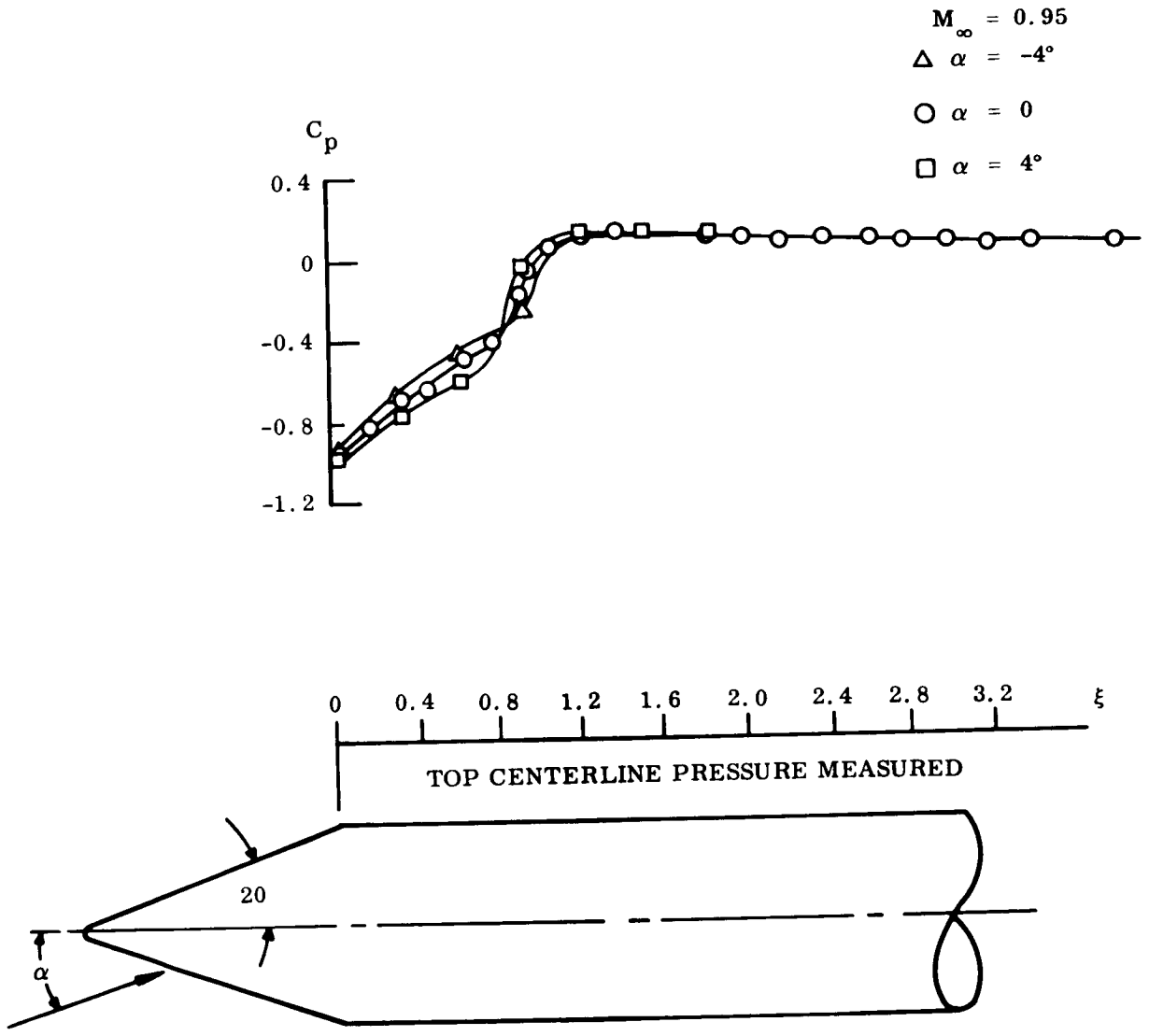


Fig. C-3 Effect of Angle of Attack on Terminal-Shock Location on a 20° Cone-Cylinder Body at $M_\infty = 0.95$

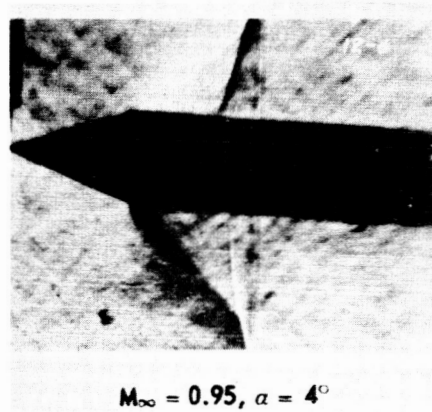
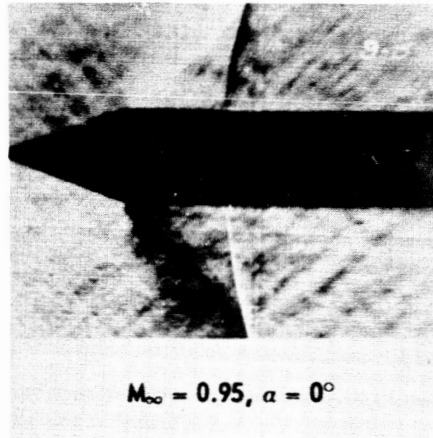


Fig. C-3 Effect of Angle of Attack on Terminal-Shock Location on a 20° Cone-Cylinder Body at $M_{\infty} = 0.95$ (Cont.)

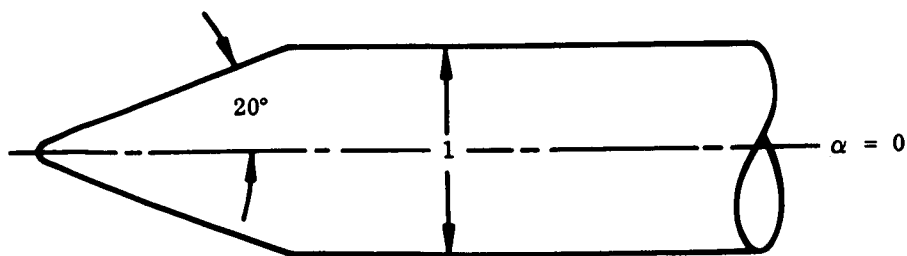
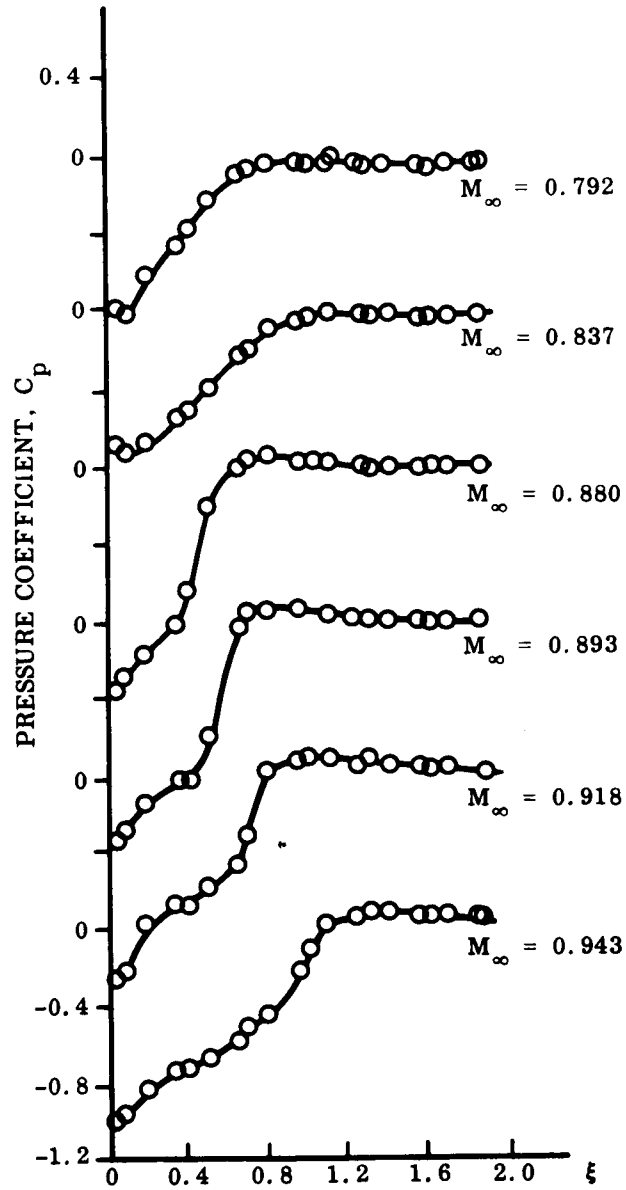
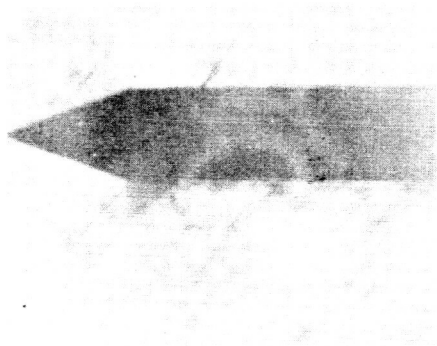
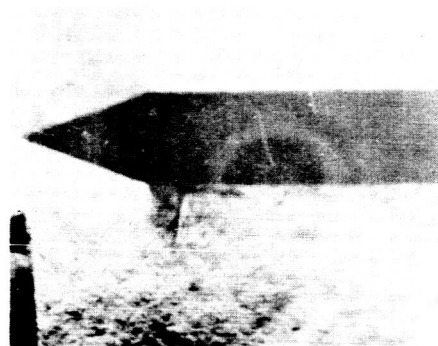


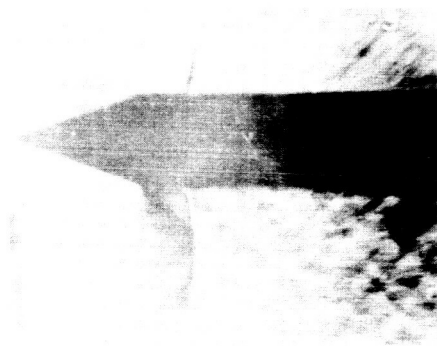
Fig. C-4 Effect of Mach Number on Terminal-Shock Location on a 20° Cone-Cylinder Body at $\alpha = 0$



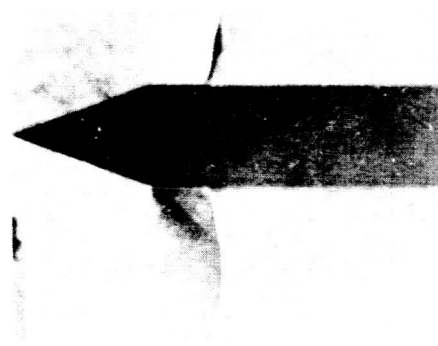
$M_{\infty} = 0.792$



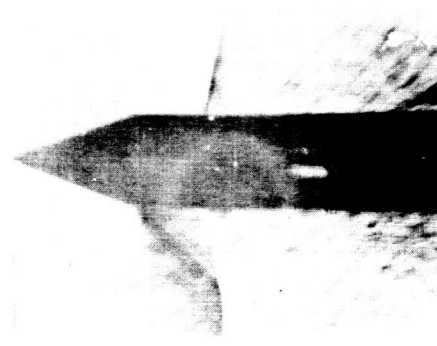
$M_{\infty} = 0.837$



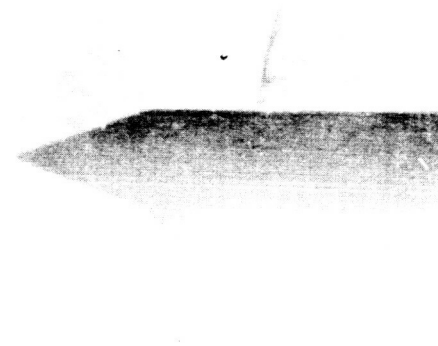
$M_{\infty} = 0.880$



$M_{\infty} = 0.893$



$M_{\infty} = 0.918$



$M_{\infty} = 0.943$

Fig. C-4 Effect of Mach Number on Terminal-Shock Location on a 20° Cone-Cylinder Body at $\alpha = 0$ (Cont.)

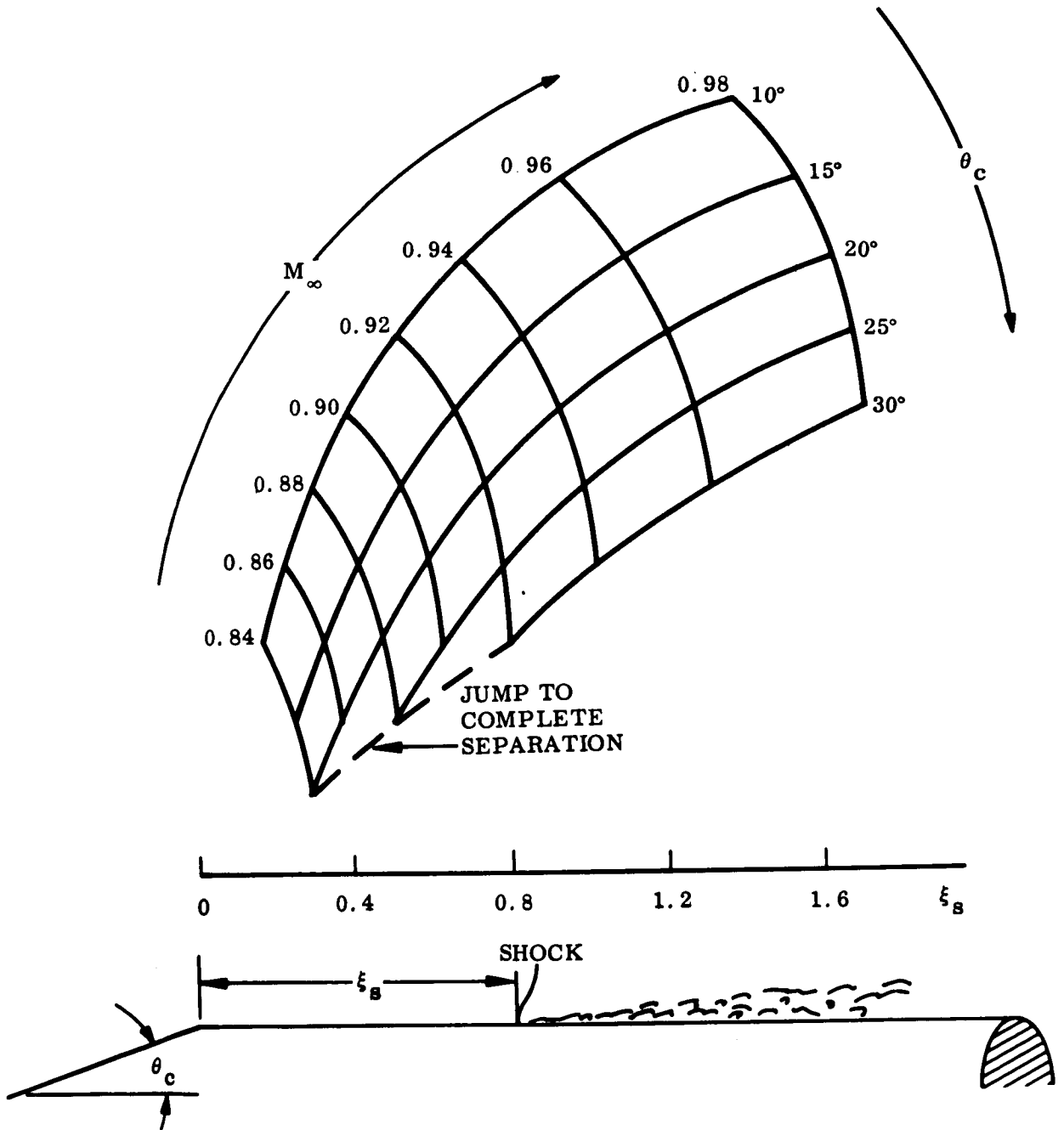


Fig. C-5 Combined Effect of Mach Number and Cone Angle on the Terminal-Shock Location on Cone-Cylinder Bodies at $\alpha = 0$

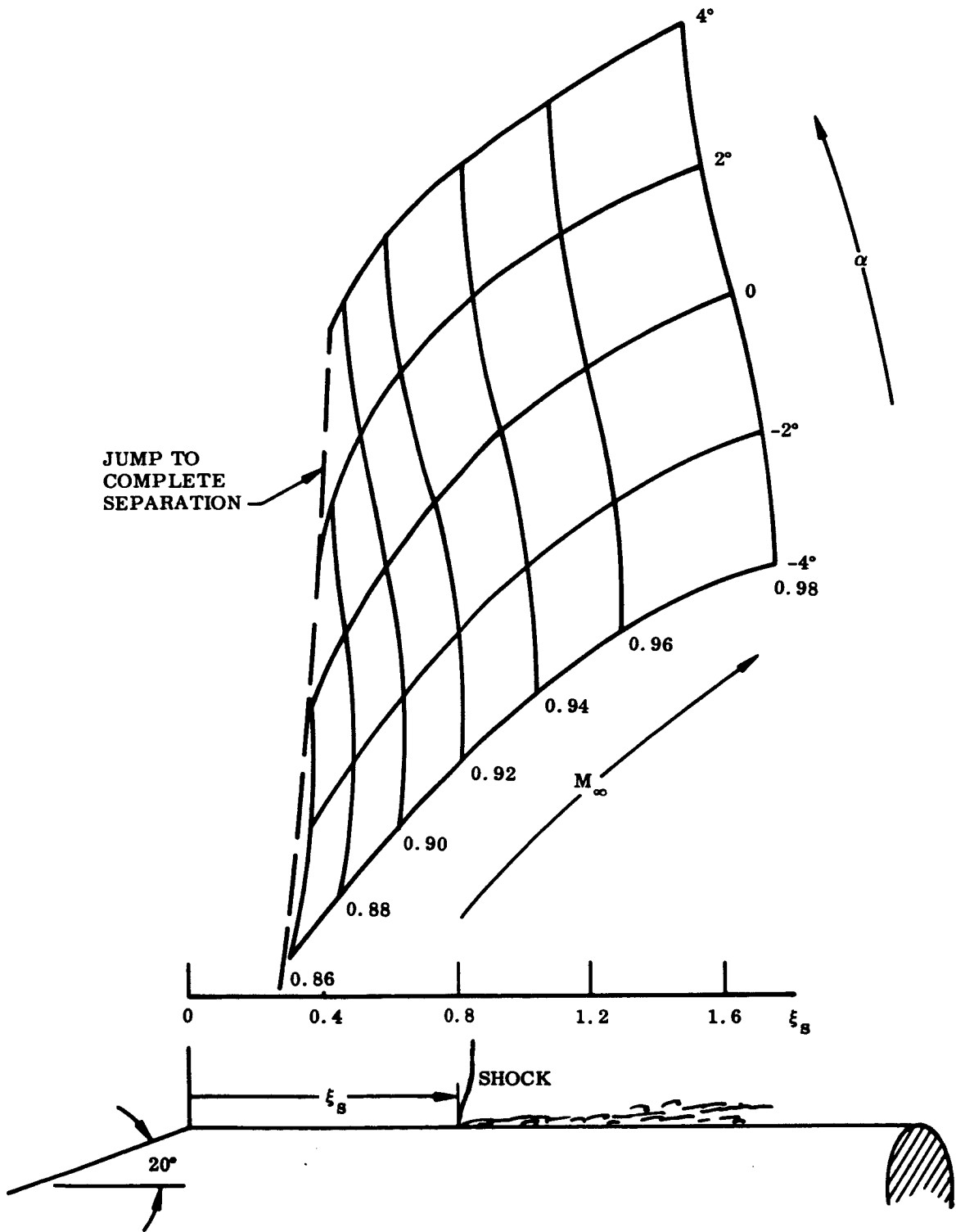


Fig. C-6 Combined Effect of Mach Number and Angle of Attack on the Terminal-Shock Location on a 20° Cone-Cylinder Body

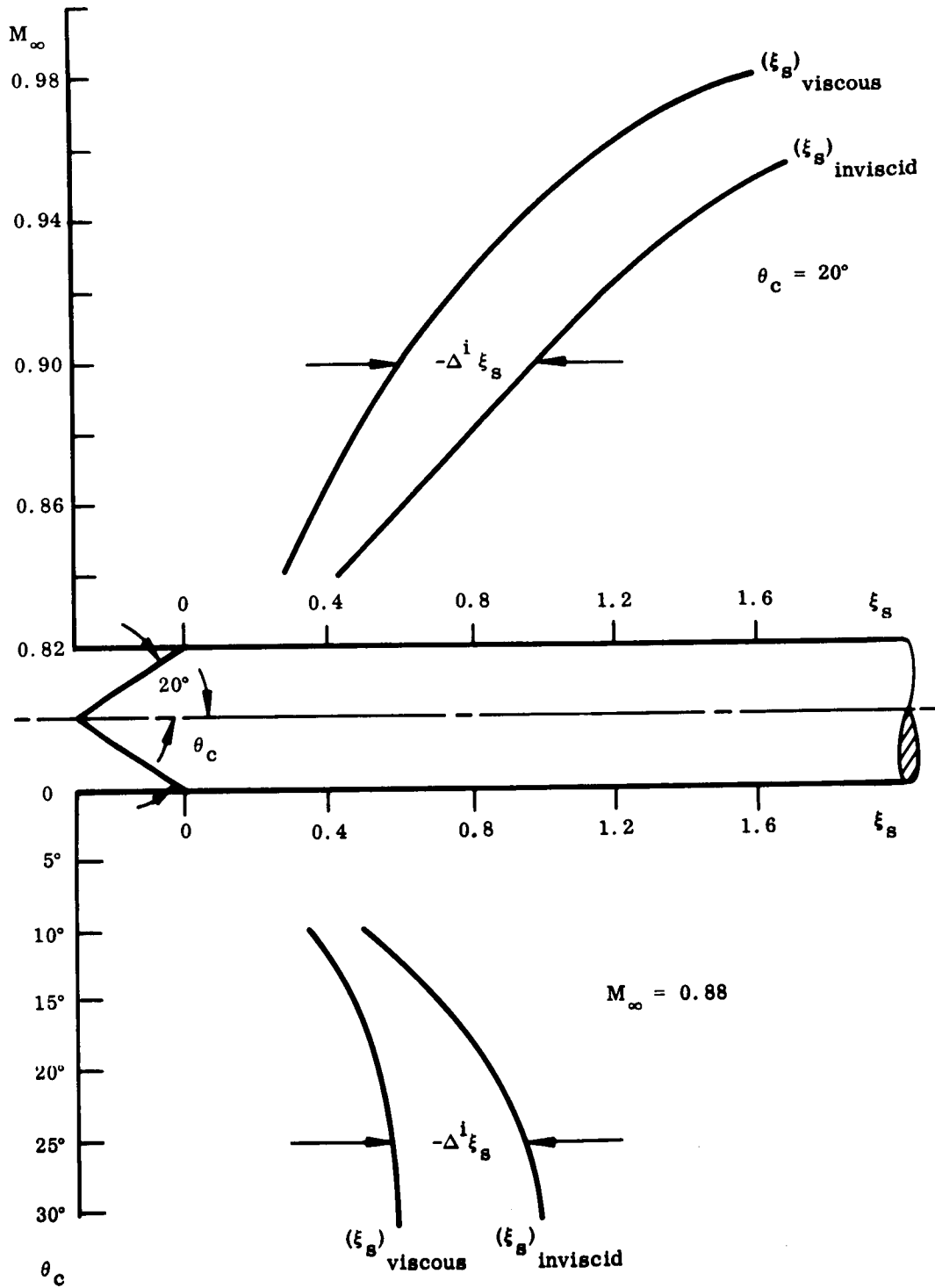


Fig. C-7 Terminal Shock Location in Inviscid and Viscous Flow on Cone-Cylinder Bodies

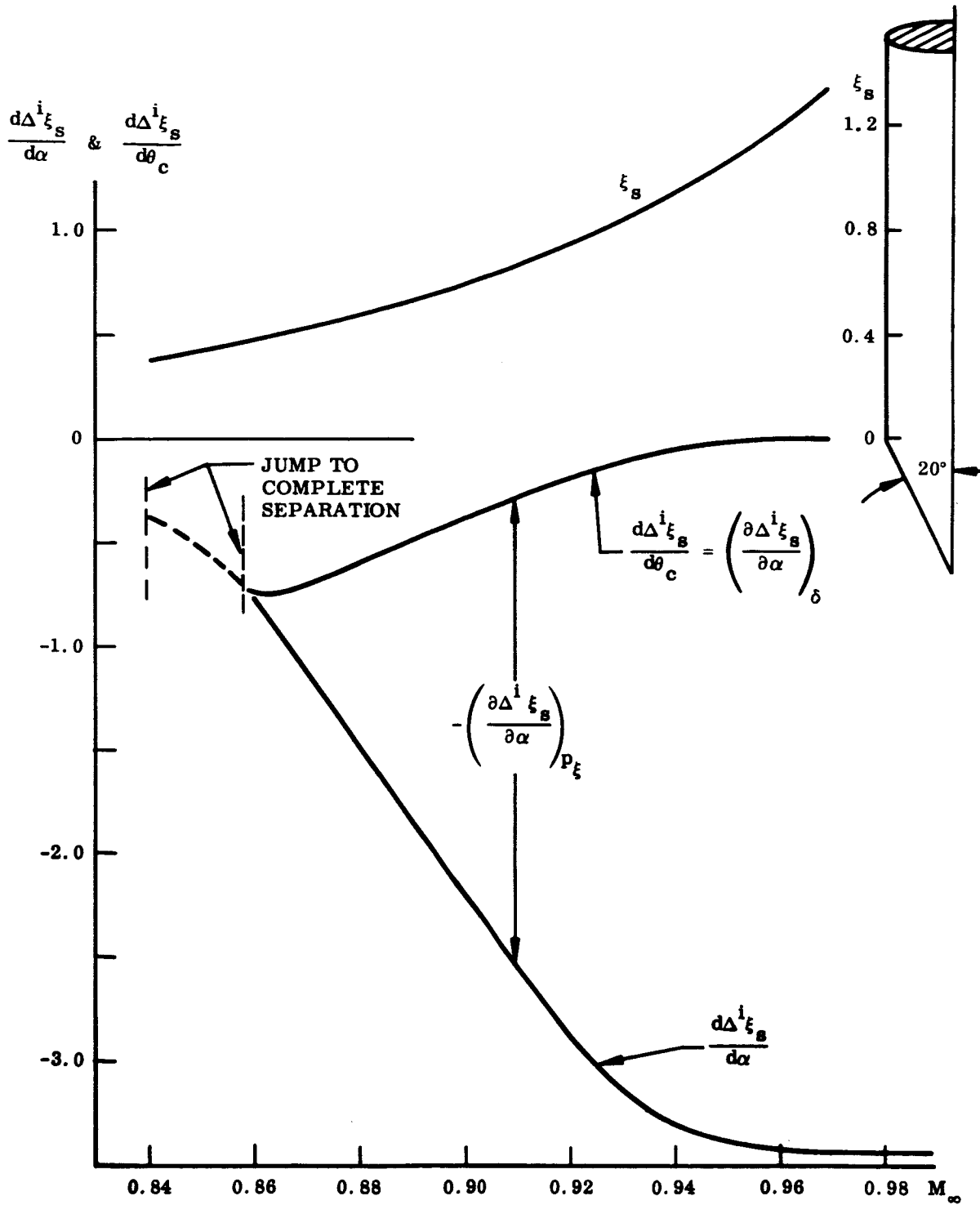


Fig. C-8 Effect of Boundary Layer Thickness and Pressure Gradient on the Terminal-Shock Movement on a 20° Cone-Cylinder Body at $\alpha = 0$ and High Subsonic Mach Numbers

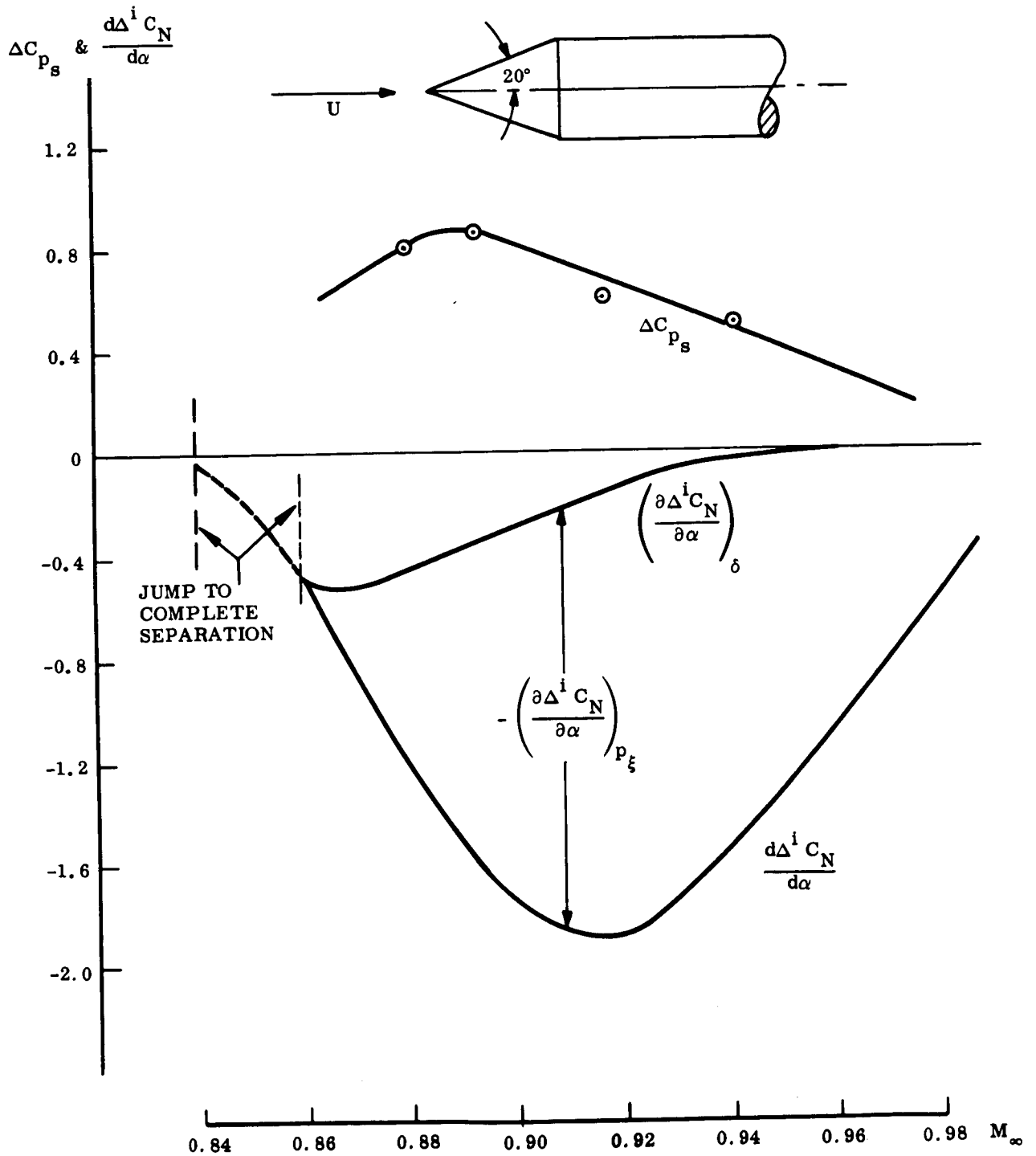


Fig. C-9 Normal Force Derivatives Induced by the Terminal-Shock Movement on a 20° Cone-Cylinder Body at $\alpha = 0$ and High Subsonic Mach Numbers

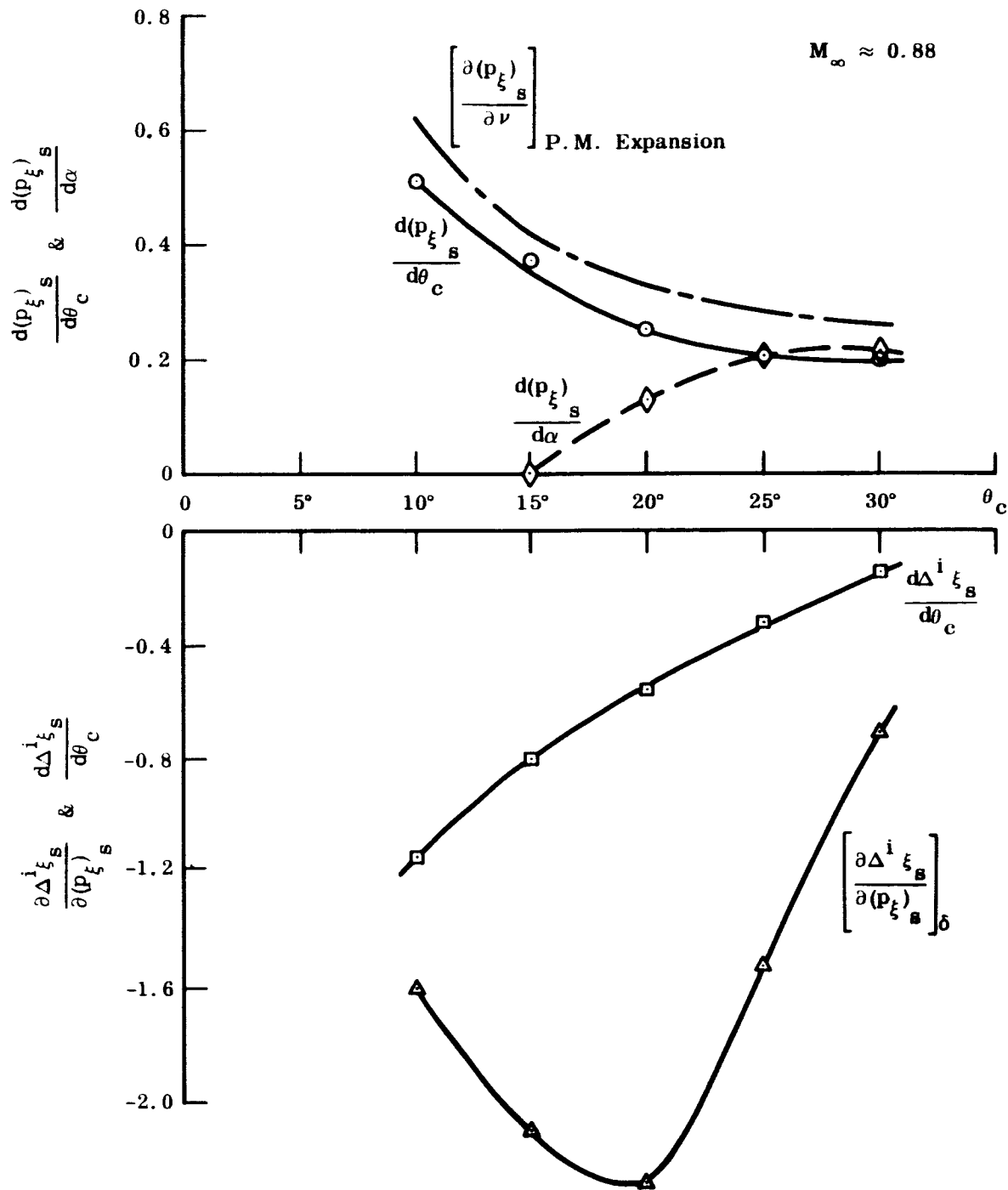


Fig. C-10 Effect of Cone Angle and Angle of Attack on the Terminal-Shock Movements at $M_\infty \approx 0.88$

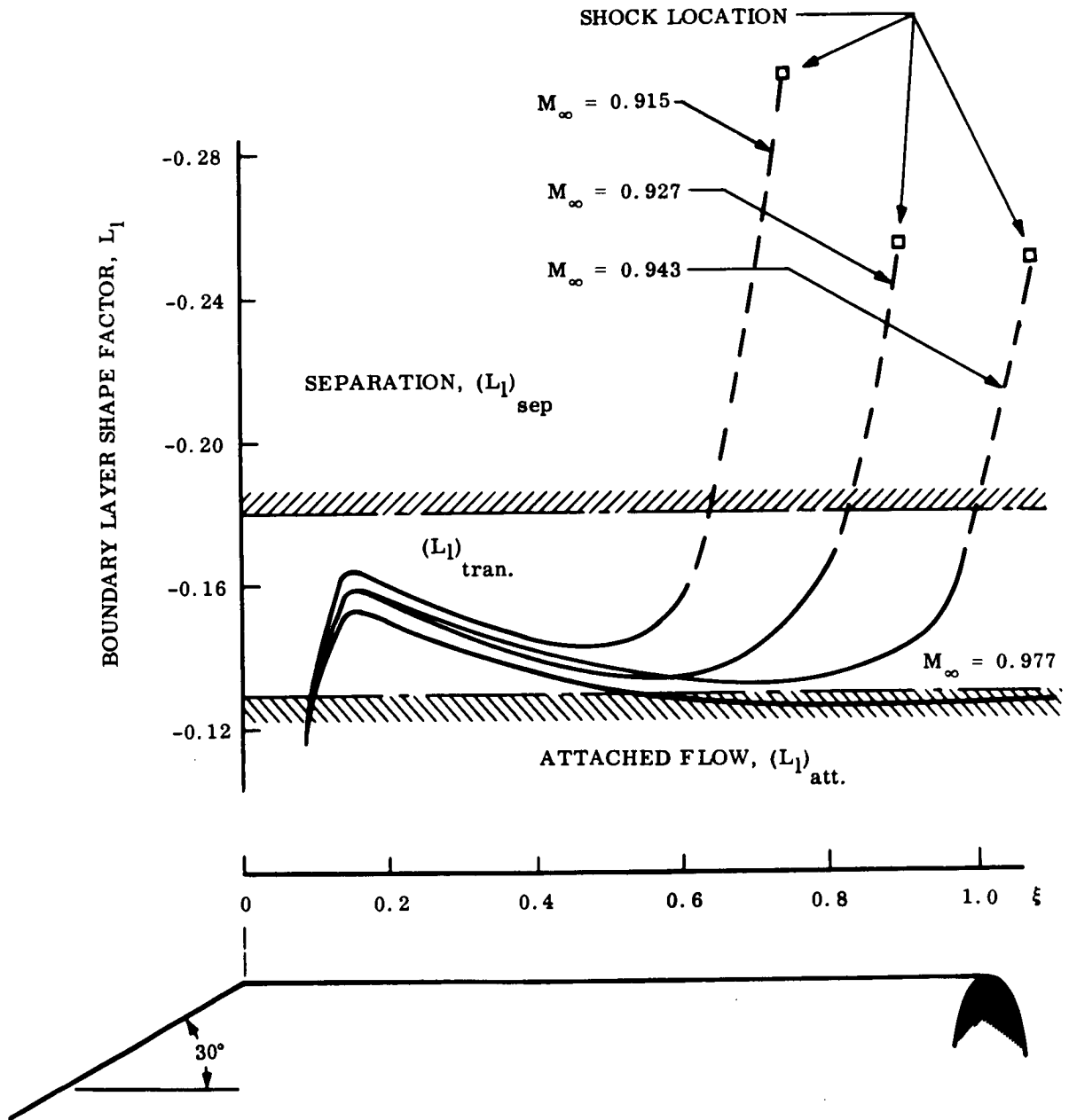


Fig. C-11 Axial Variation of the Boundary Layer Auxiliary Shape Factor on a 30° Cone-Cylinder Body at $\alpha = 0$ and Various Mach Numbers

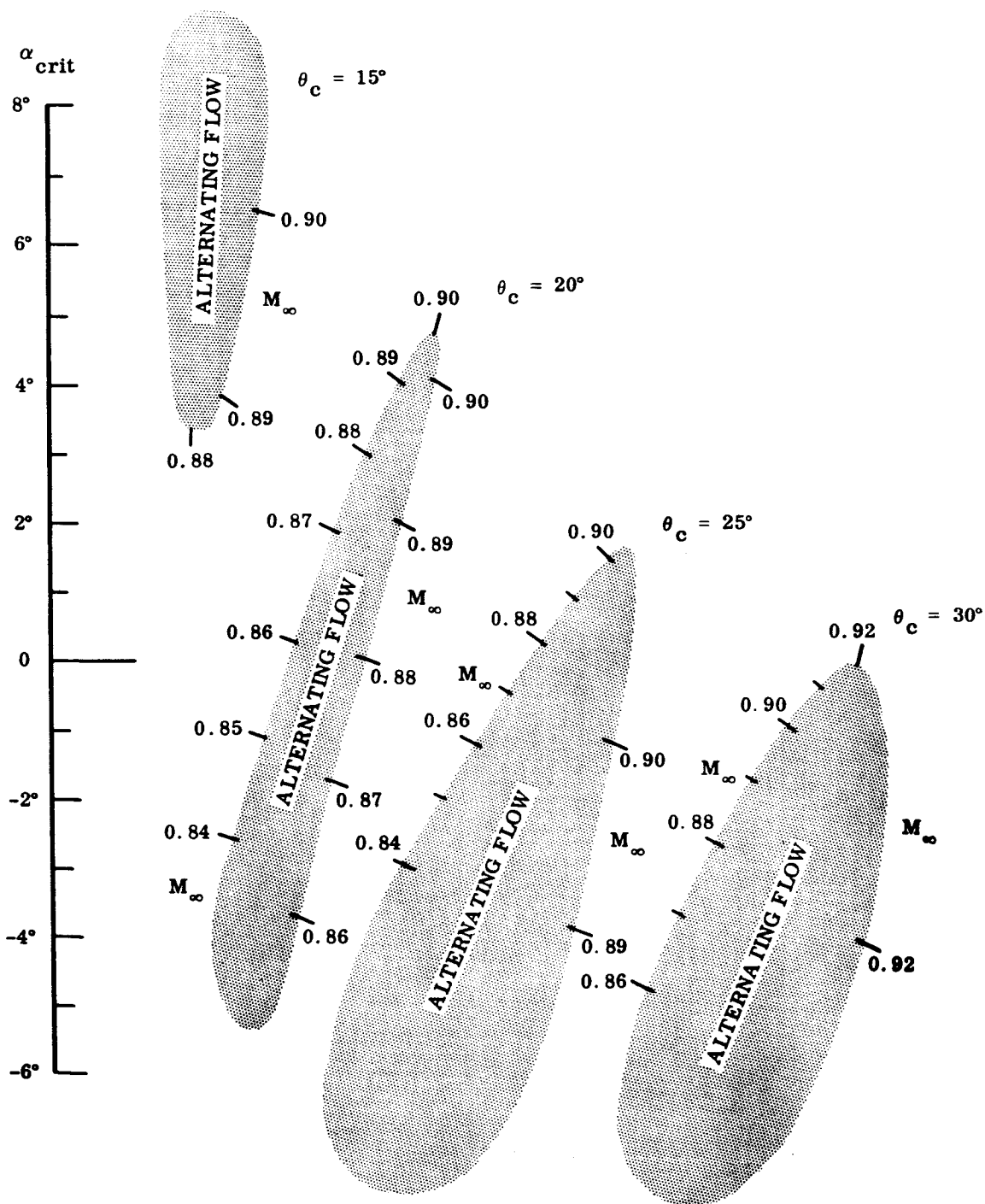
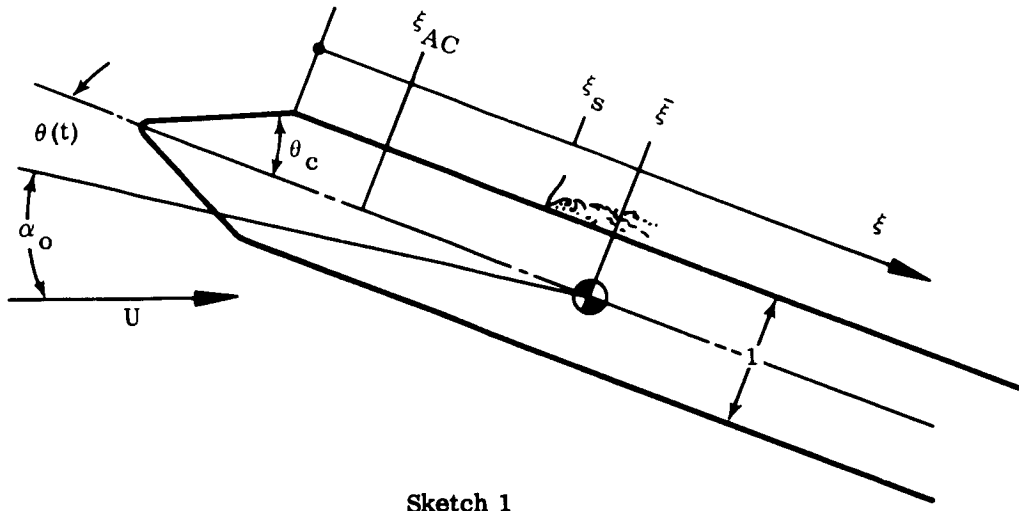
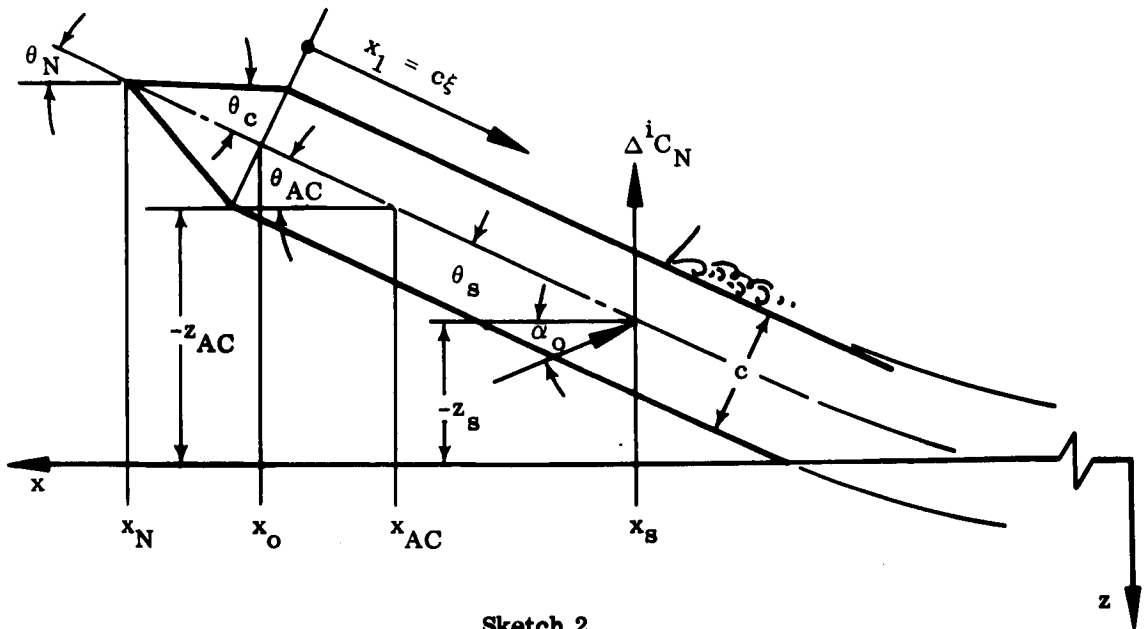


Fig. C-12 α - M_∞ -Regions for Fluctuating Flow on Cone-Cylinder Bodies with Various Cone Half-Angles



Sketch 1



Sketch 2

Fig. C-13 Coordinate Systems

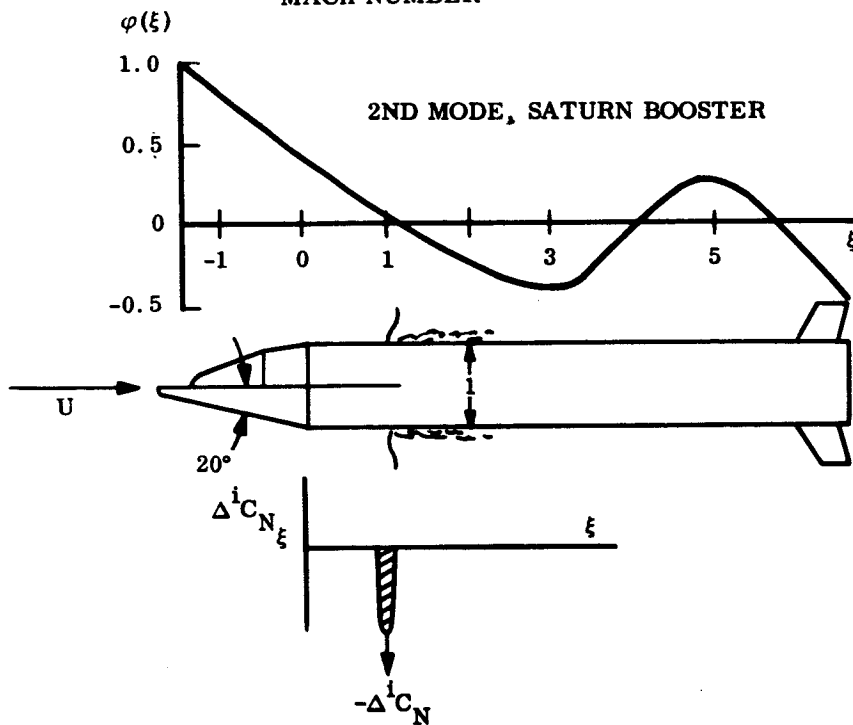
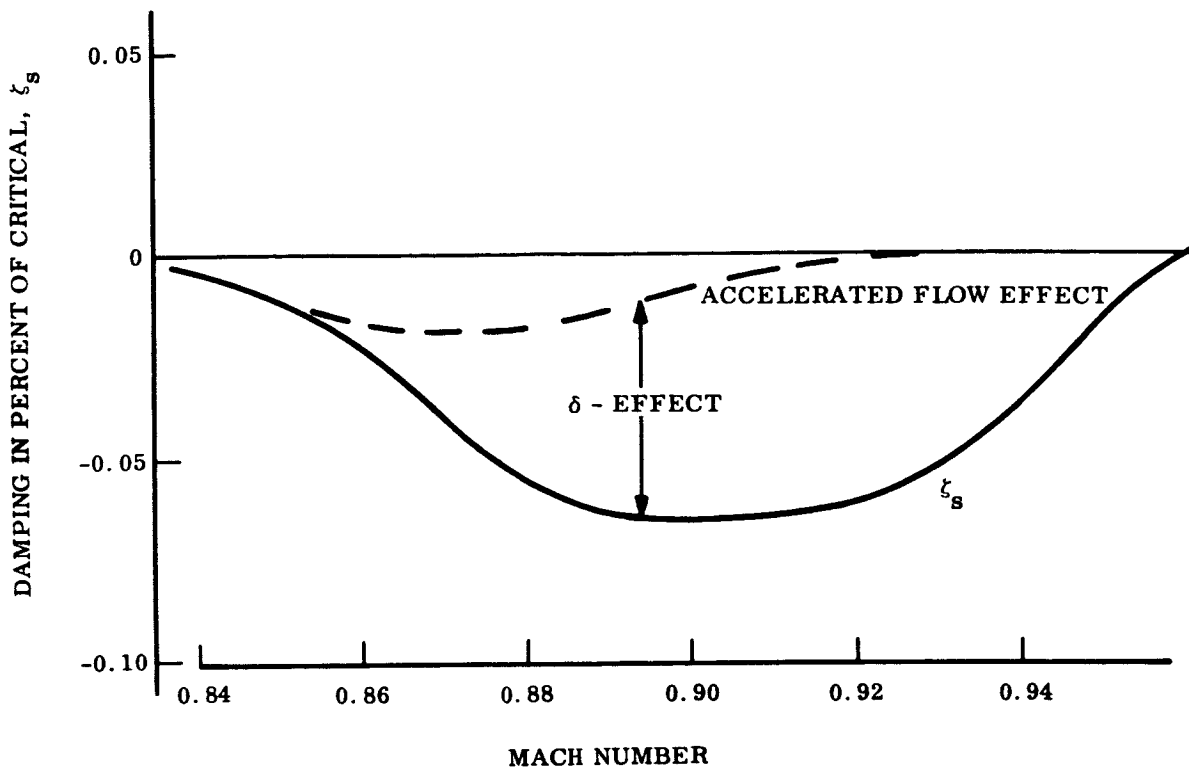
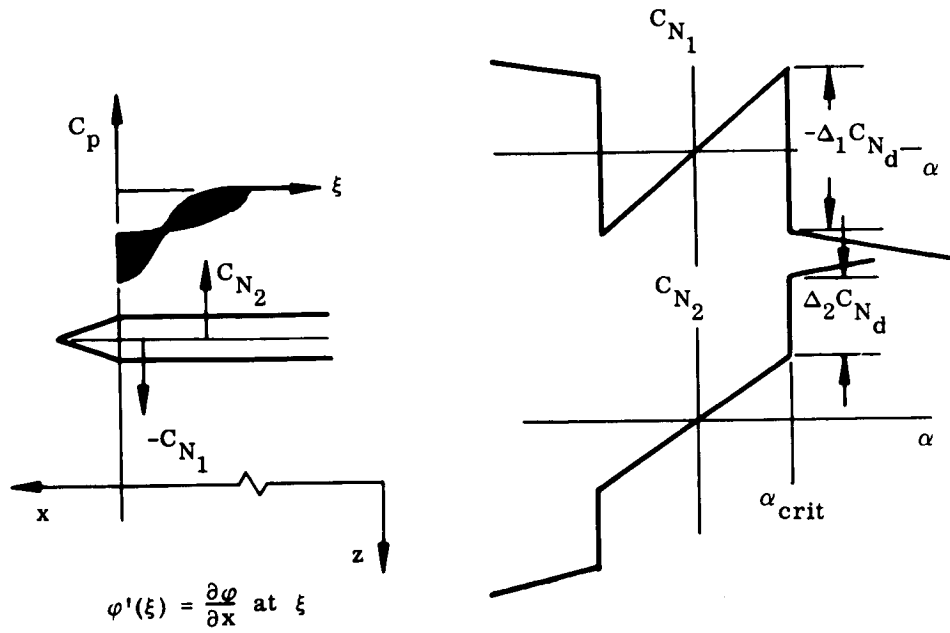
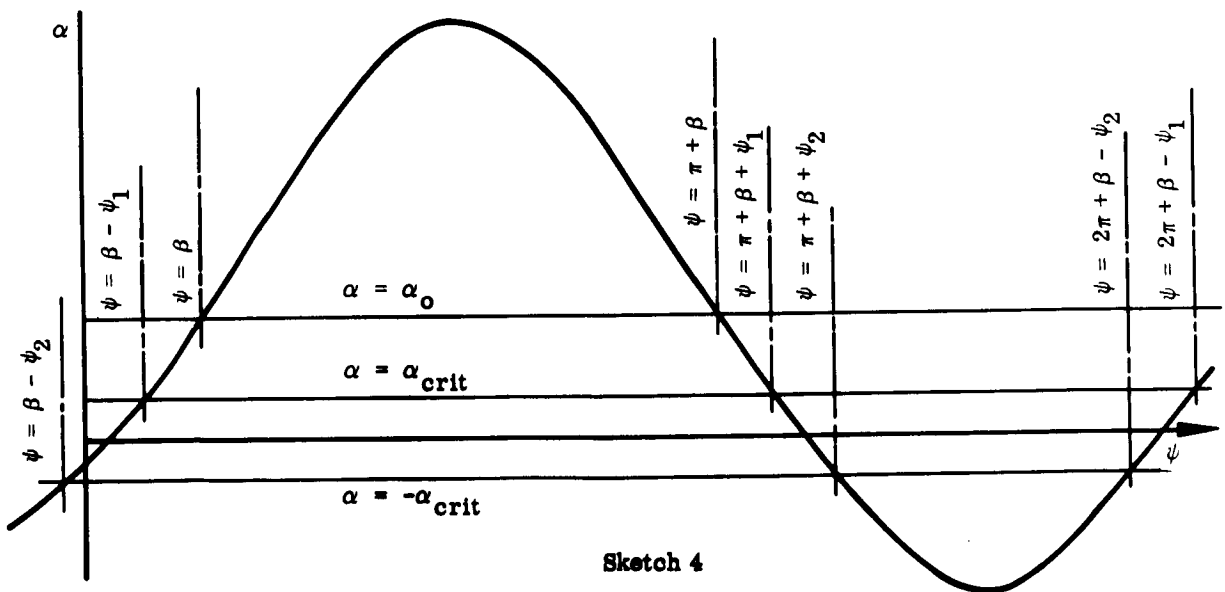


Fig. C-14 Effect of Separation-Induced Terminal-Shock Movement on the Damping of an Elastic Vehicle Oscillating in its Second Bending Mode



Sketch 3



Sketch 4

Fig. C-15 Schematic Characteristics

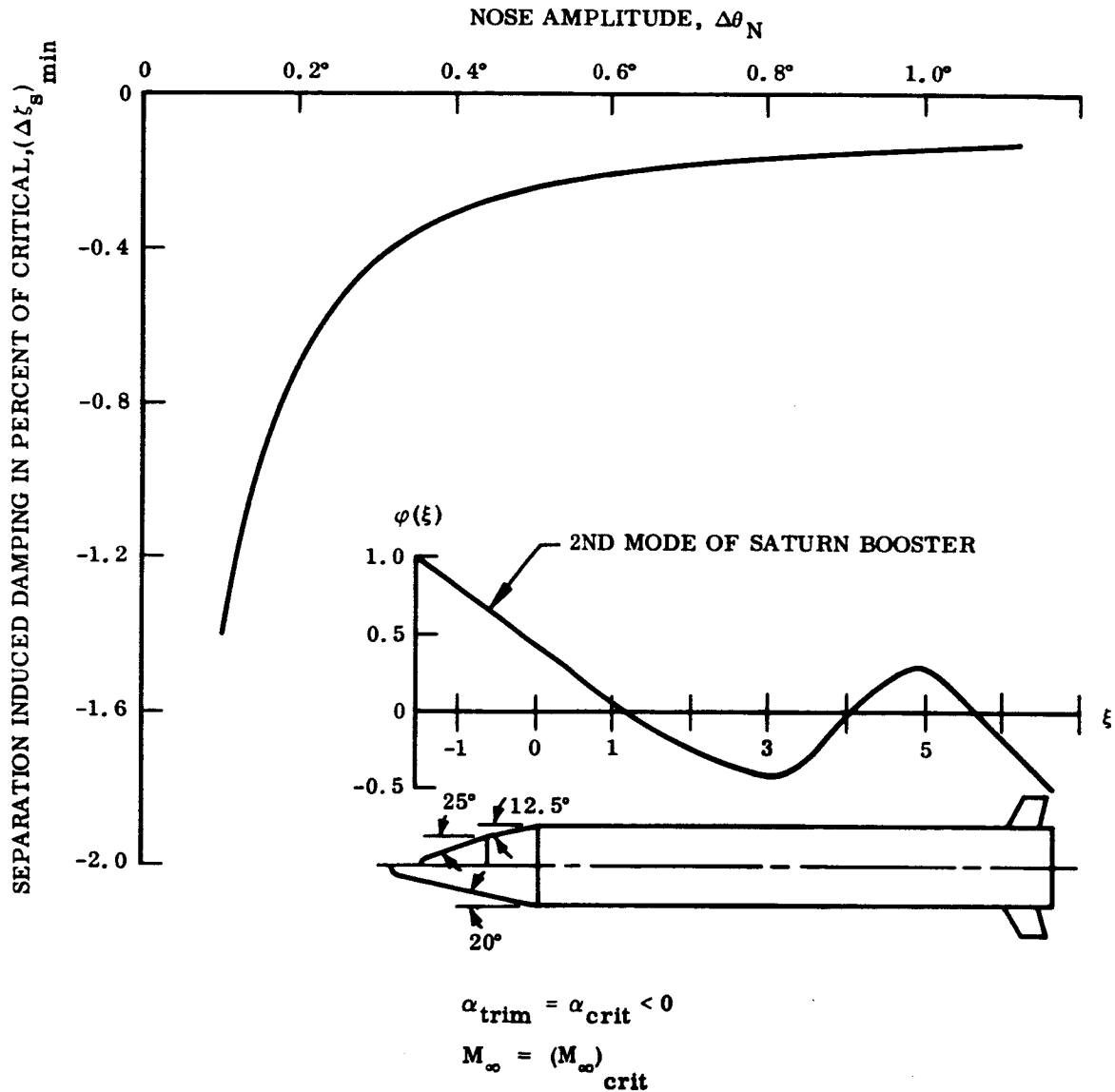


Fig. C-16 Effect of Complete Windward-Side Flow Separation in the Damping of an Elastic Vehicle Oscillating in its Second Bending Mode at Various Nose Amplitudes

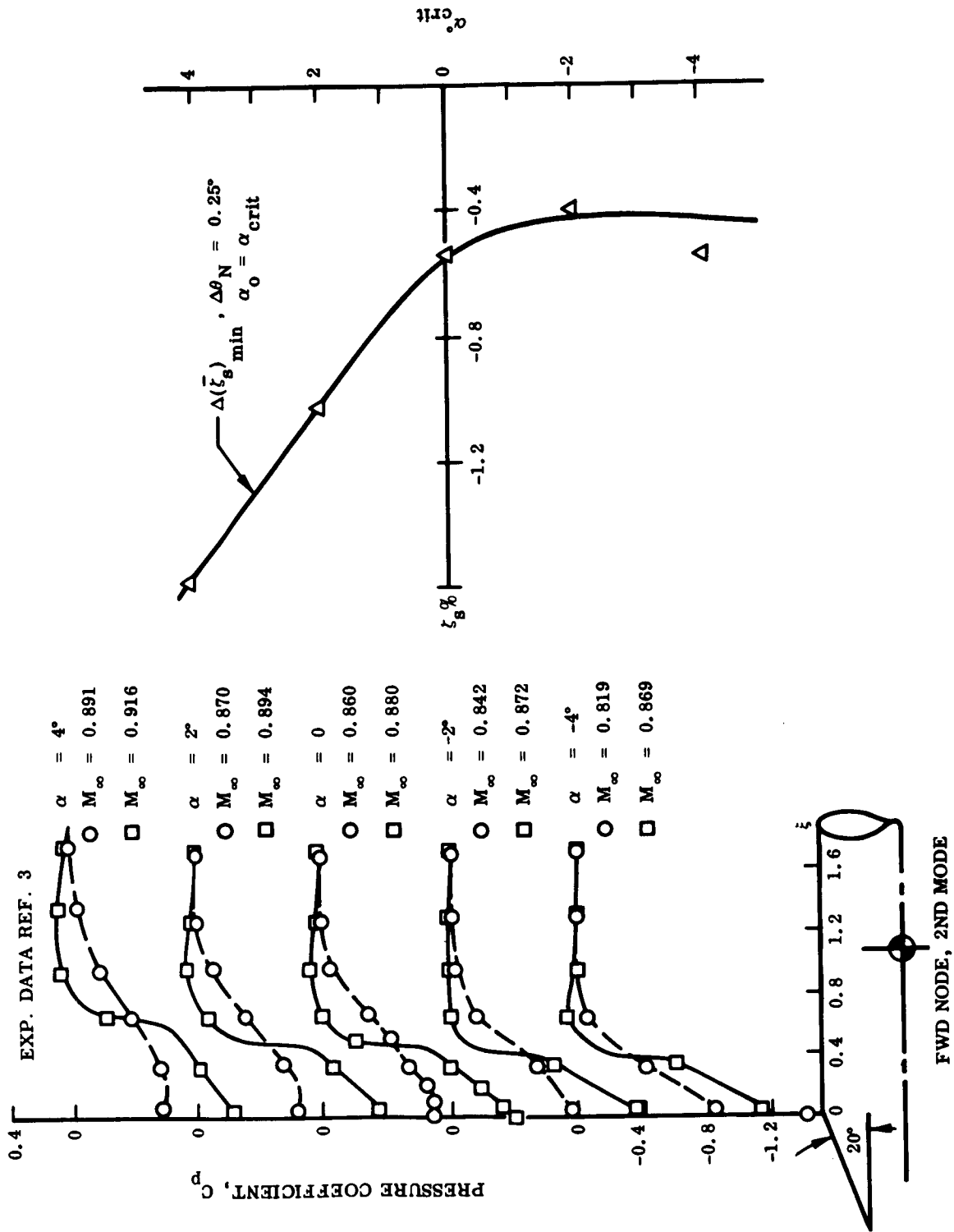


Fig. C-17 Comparison of Leeward- and Windward-Side Damping Combinations Induced by Complete Flow Separation an Elastic Vehicle Oscillating in its Second Bending Mode at 0.25 Deg Nose Amplitude

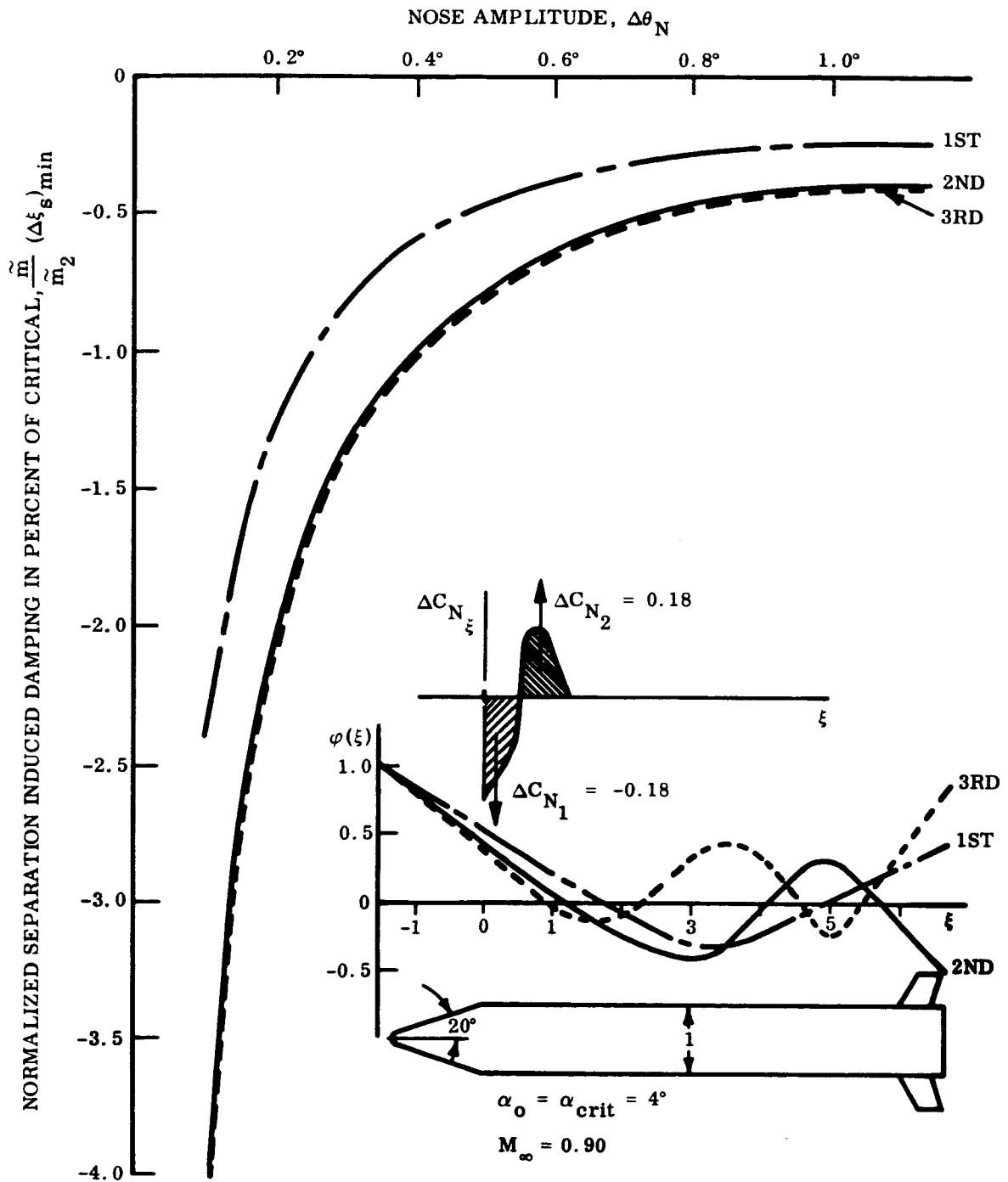


Fig. C-18 Effect of Mode Shape on the Separation-Induced Elastic Vehicle Damping

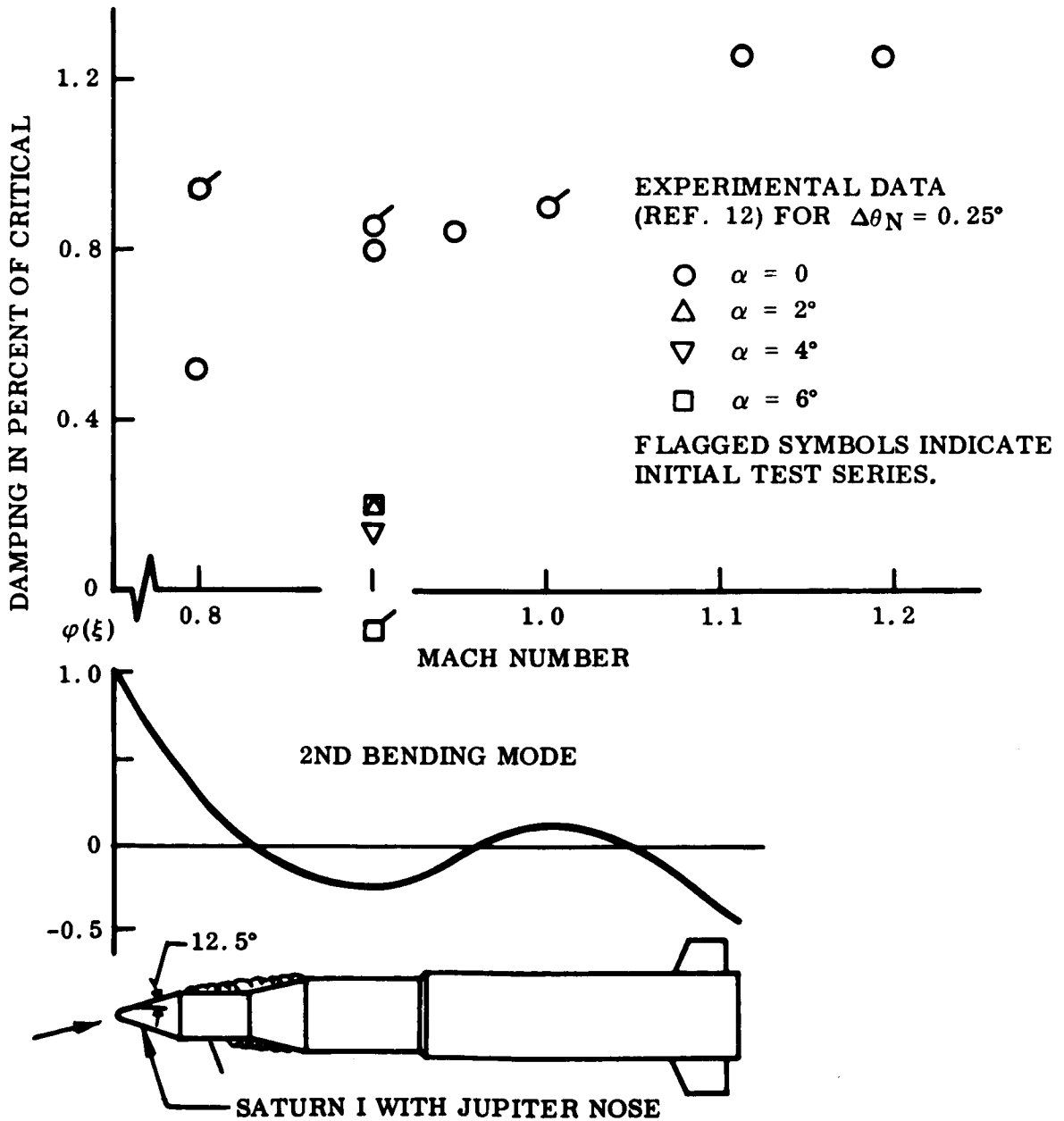


Fig. C-19 Aerodynamic Damping Measured on an 8-Percent Elastic Model of the Saturn I, Block II Vehicle with a Jupiter Nose

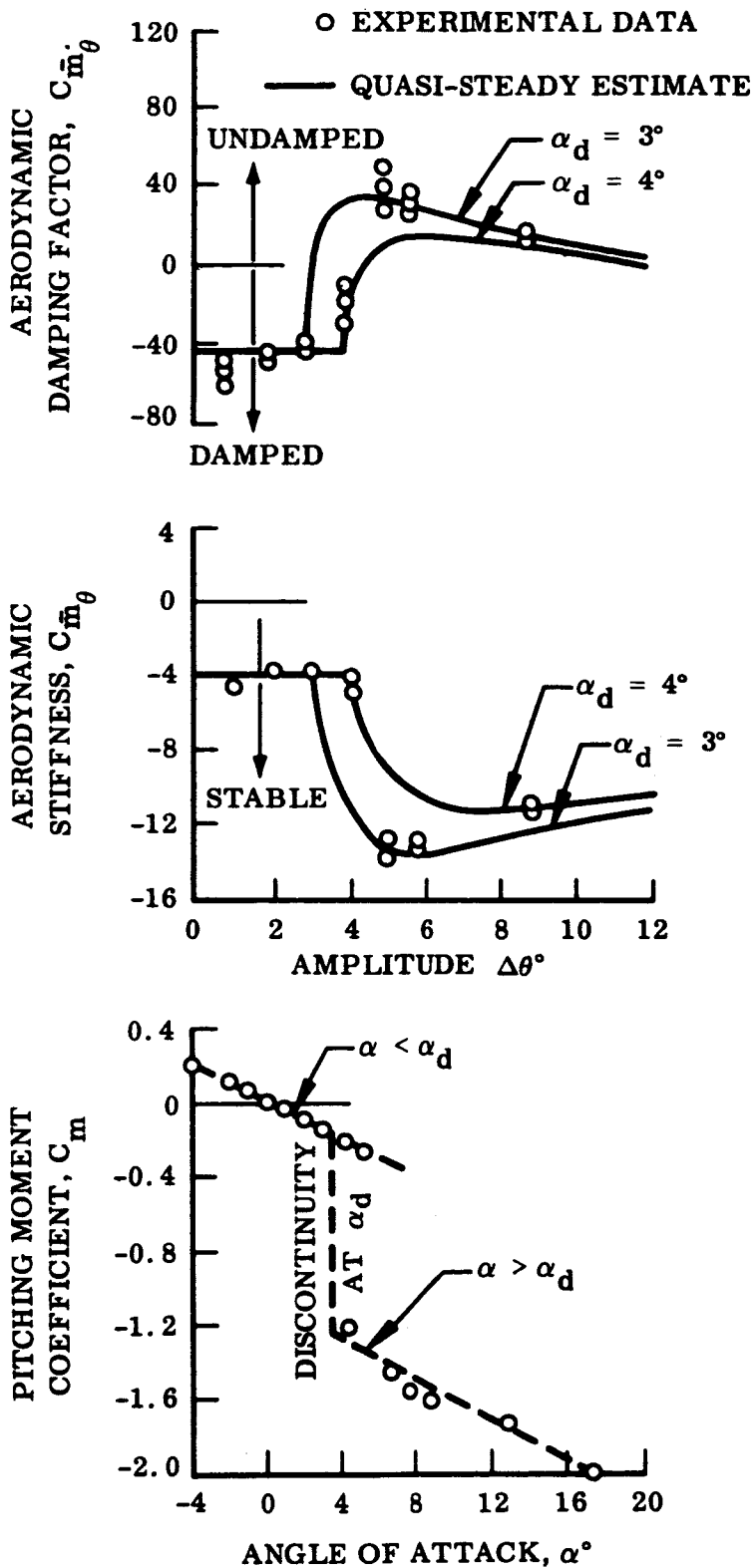


Fig. C-20 Dynamic Effects of Separation Induced Pitching-Movement Discontinuity on a Blunt-Nose, Cylinder-Flare Body at Transonic Speed

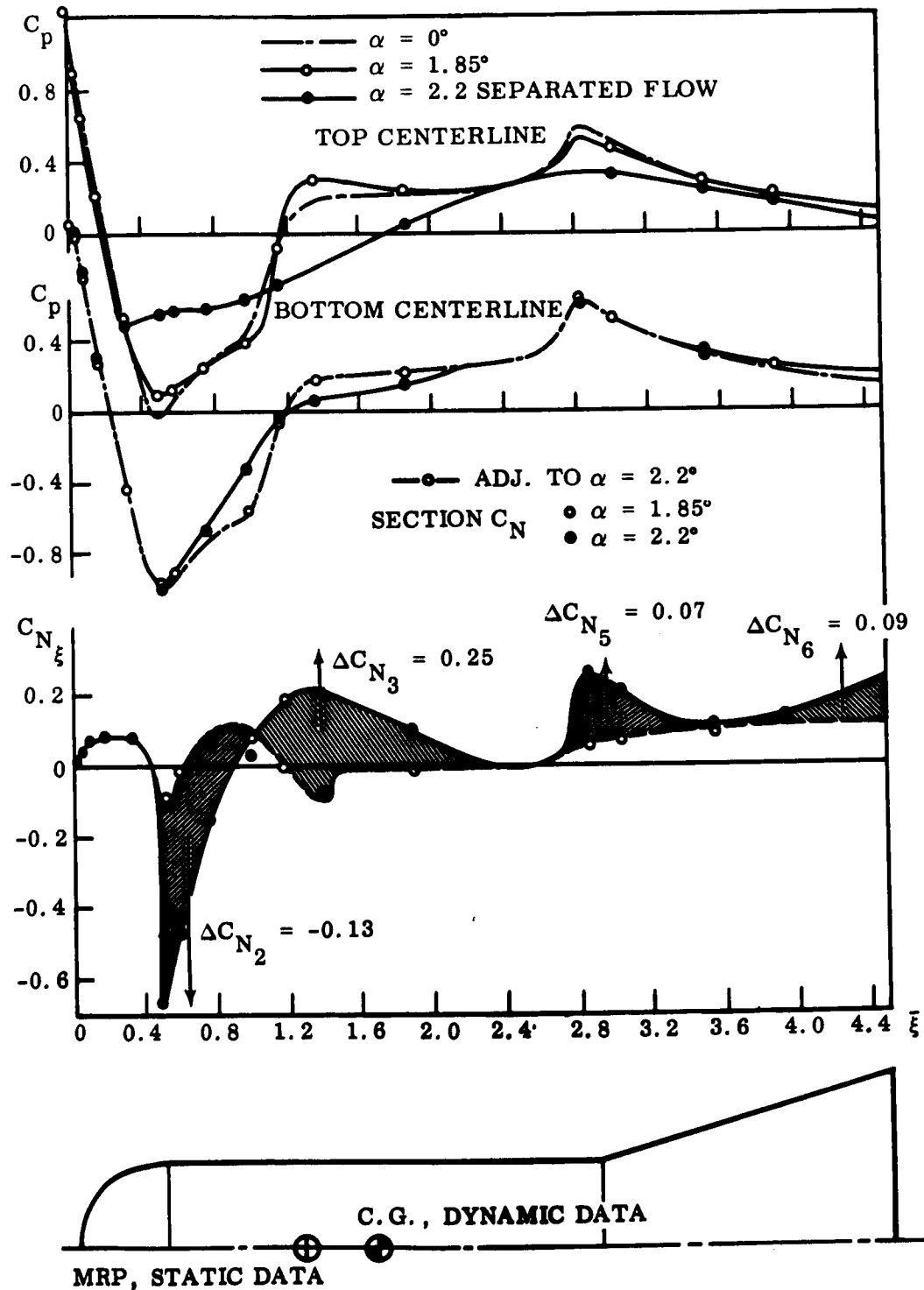


Fig. C-21 Effect of Complete Leeward-Side Separation on Pressure and Load Distribution Over a Hemispherical-Nose, Cylinder-Flare Body at $M_\infty = 0.95$

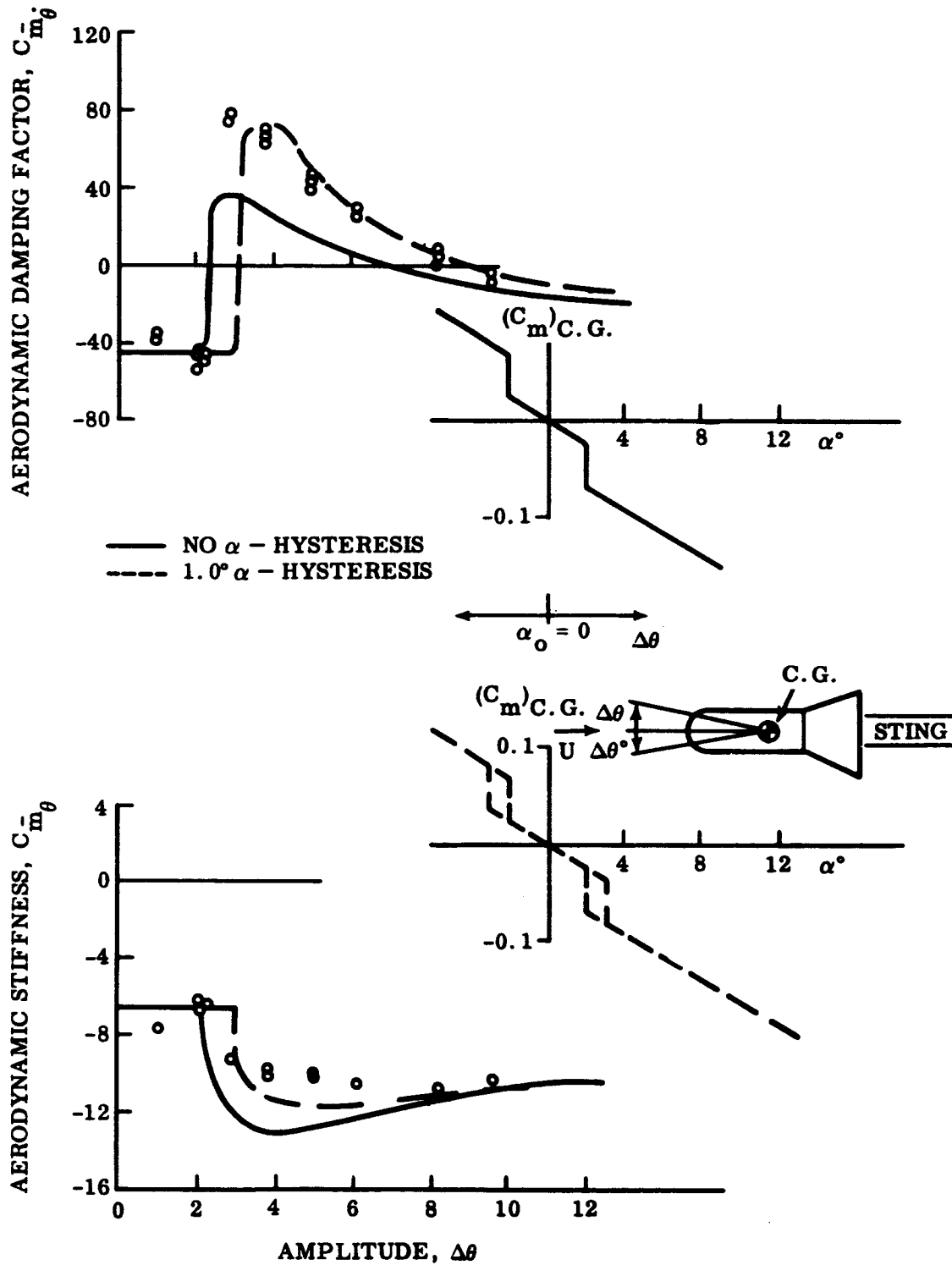
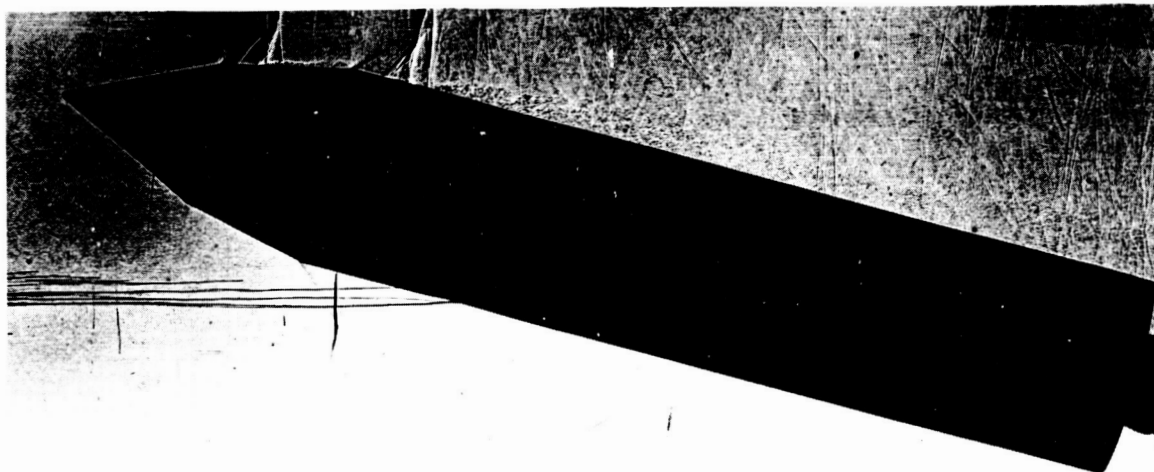
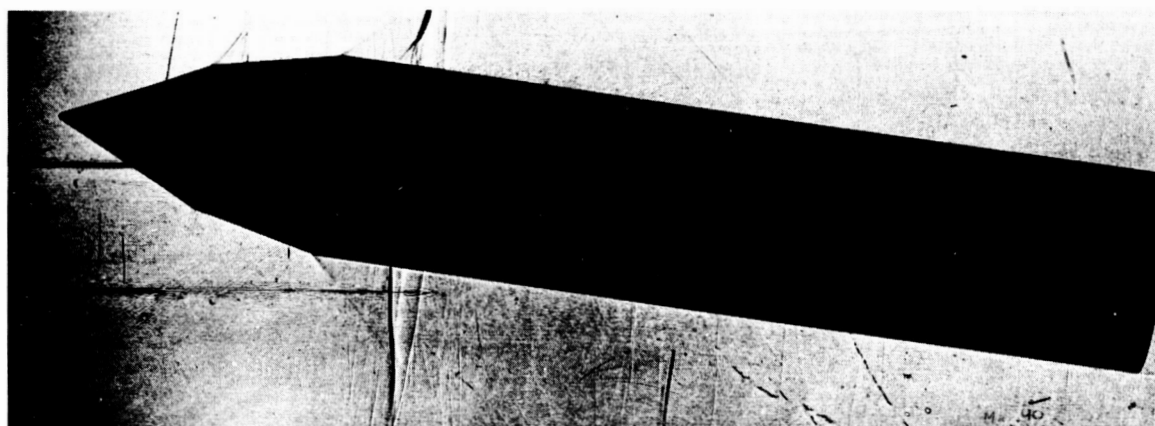


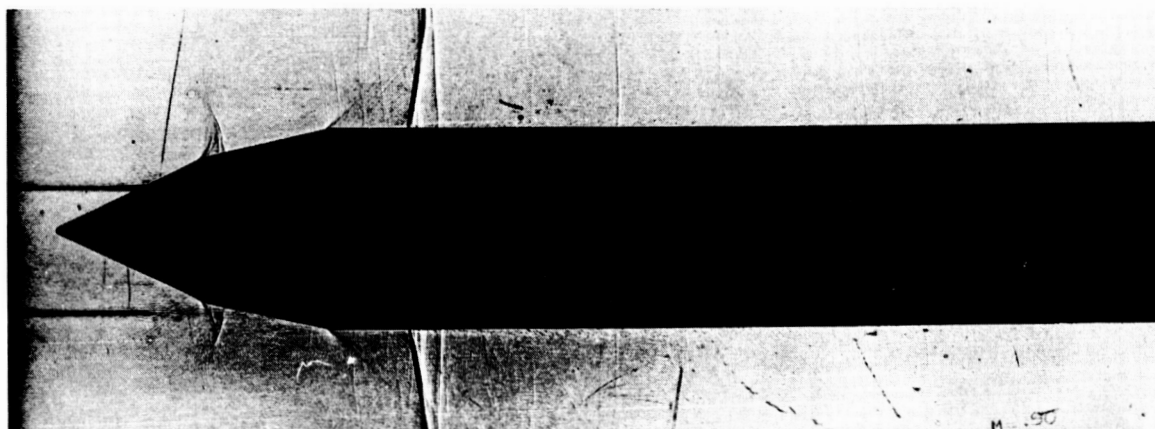
Fig. C-22 Dynamic Effects of Separation-Induced Pitching-Movement Discontinuity on a Hemispherical-Nose, Cylinder-Flare Body at $M_\infty = 0.95$



$\alpha = 16^\circ$



$\alpha = 8^\circ$



$\alpha = 0$

Fig. C-23 Shadowgraphs of the Flow Over the Saturn IB SA-203 Vehicle With a Generalized Payload at $M_\infty = 0.9$ and Various Angles of Attack

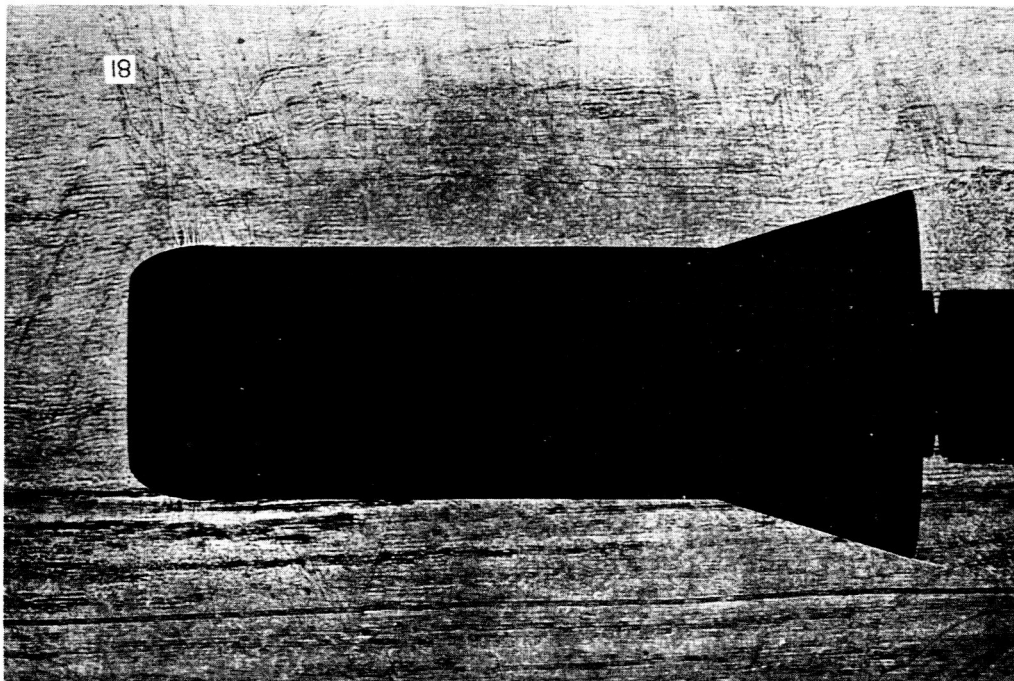
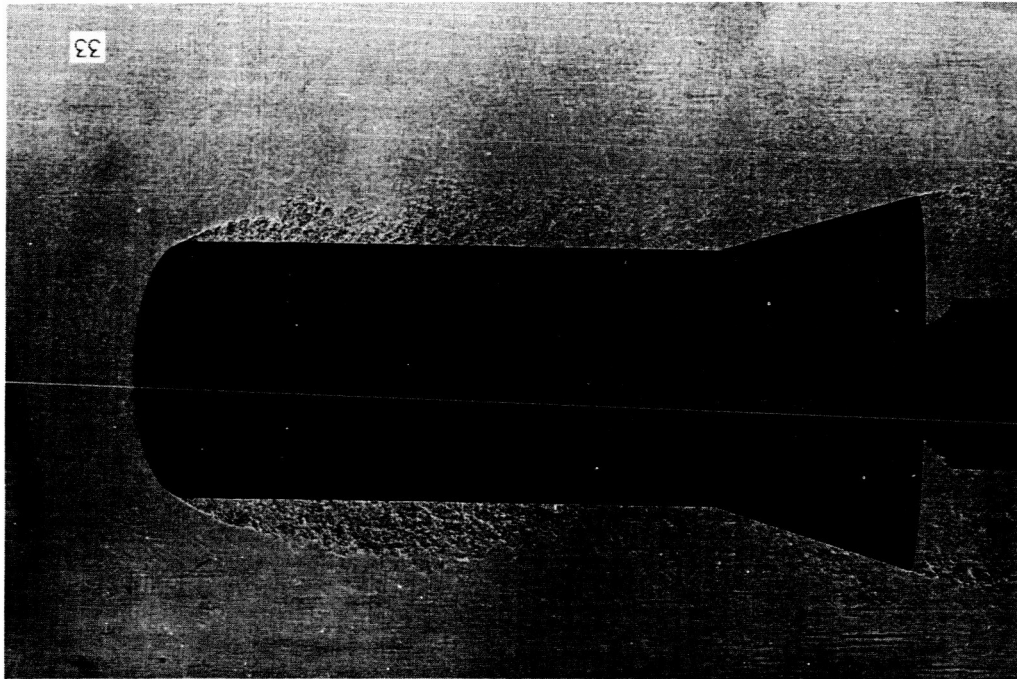


Fig. C-24 Shadowgraphs at $M_\infty = 0.65$ of the Flow Over Two Blunt-Nose, Cylinder-Flare Bodies With Identical Impact Nose Drag

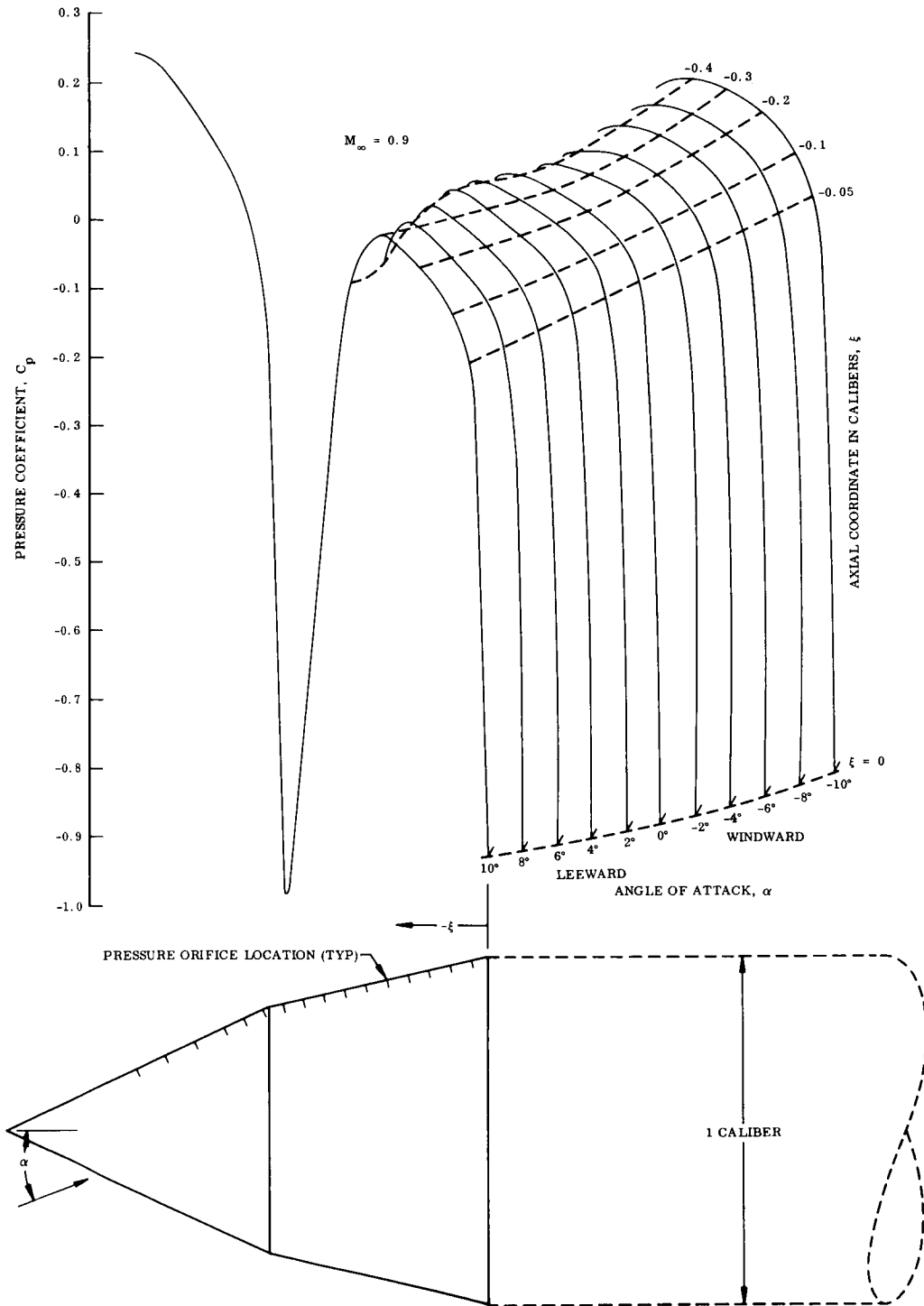


Fig. C-25 Pressure Distribution Over the Forebody of the SA-203 Vehicle at $M_\infty = 0.9$ and Various Angles of Attack

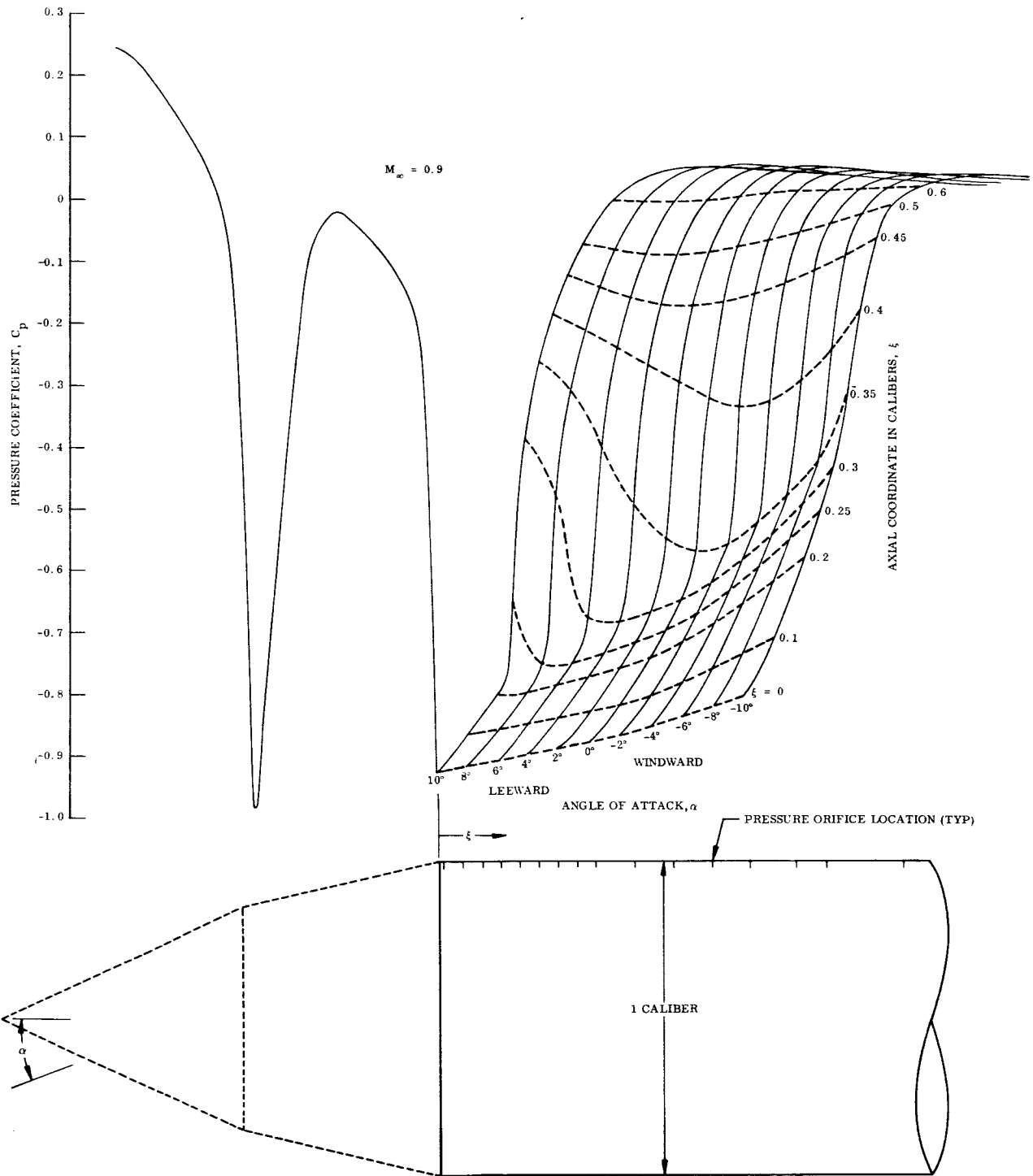
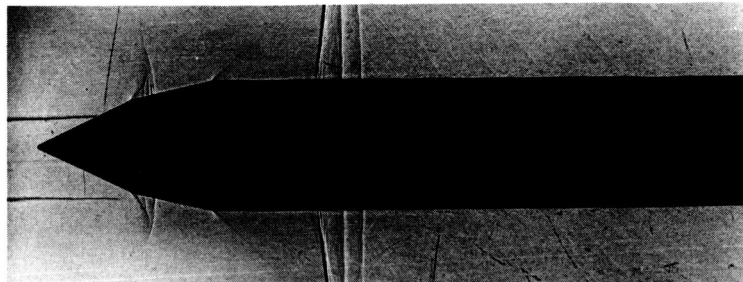
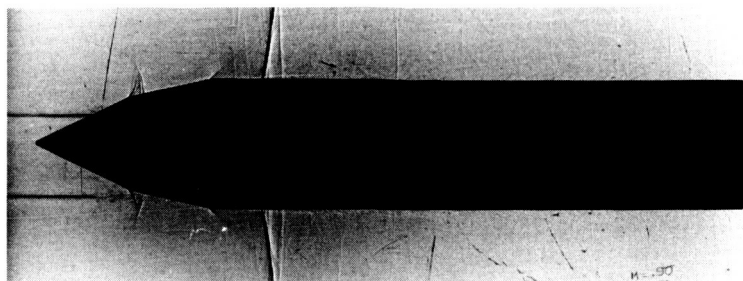


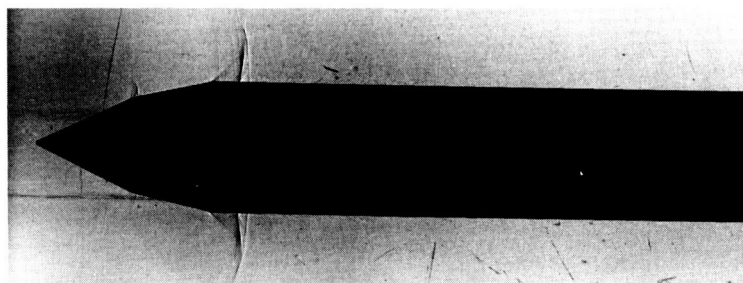
Fig. C-25 Pressure Distribution Over the Forebody of the SA-203 Vehicle at $M_\infty = 0.9$ and Various Angles of Attack (Cont.)



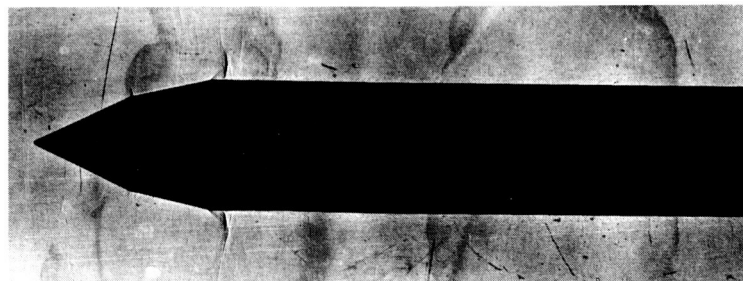
$M_{\infty} = 0.95$



$M_{\infty} = 0.90$



$M_{\infty} = 0.85$



$M_{\infty} = 0.80$

Fig. C-26 Shadowgraphs of the Flow Over the SA-203 Vehicle at $\alpha = 0$

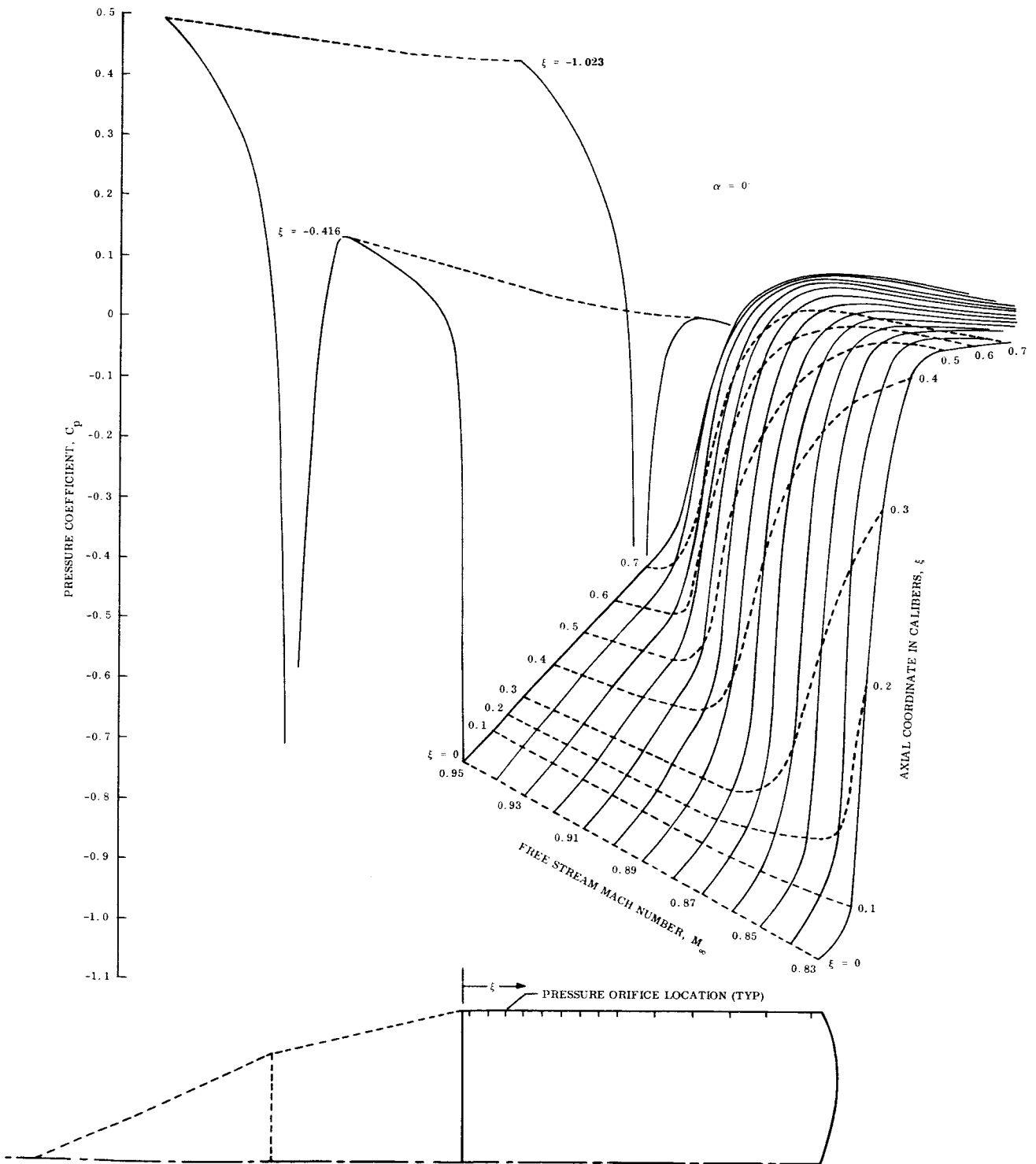


Fig. C-27 Pressure Distribution Over the Forebody of the SA-203 Vehicle at $\alpha = 0$ and Various Mach Numbers

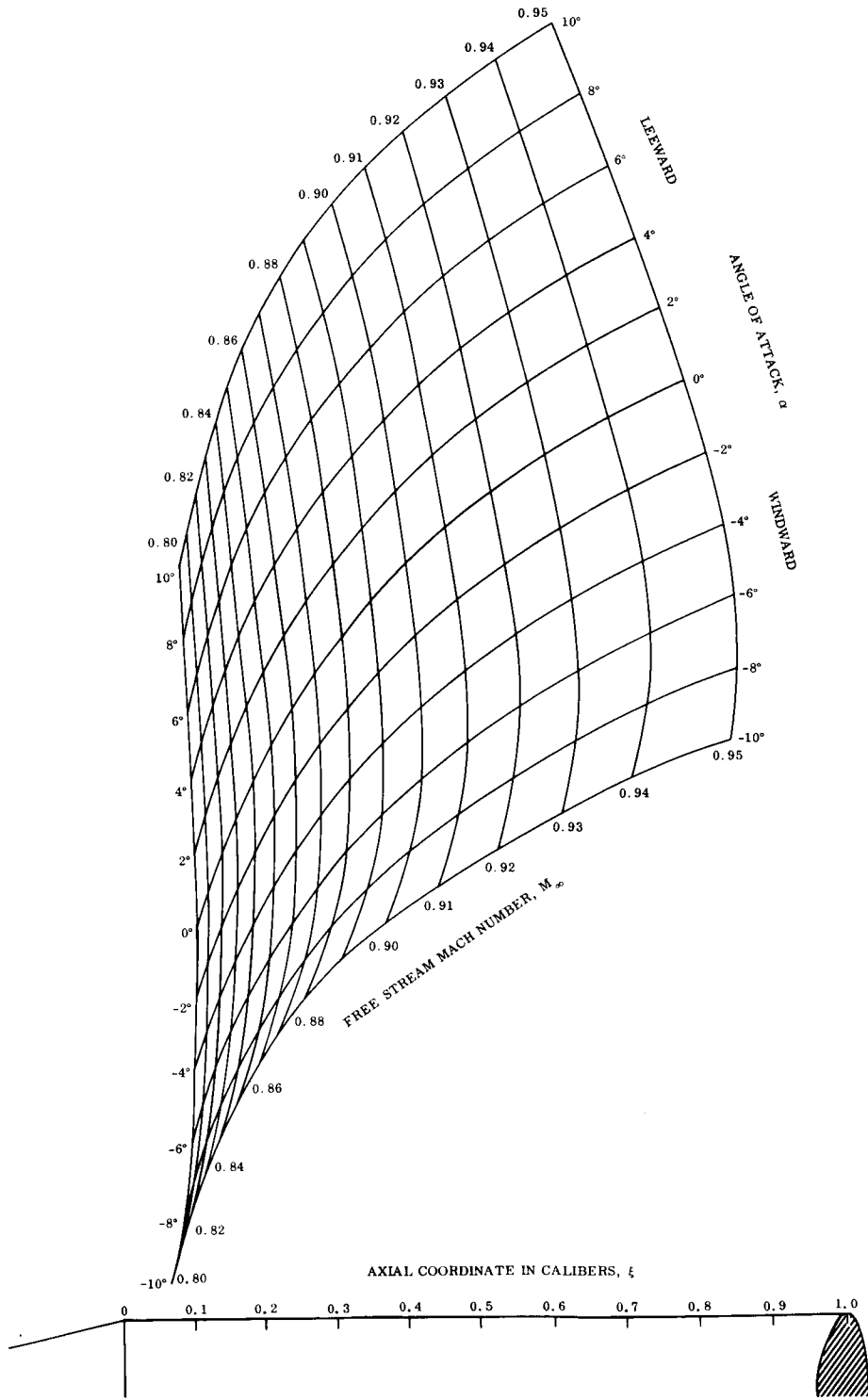


Fig. C-28 Terminal-Shock Position on the SA-203 Vehicle as a Function of Mach Number and Angle of Attack

C-62